UC Berkeley
UC Berkeley Electronic Theses and Dissertations

Title

Methods of Transverse Lifetime Extension in Nuclear Spins

Permalink

https://escholarship.org/uc/item/5gq739ww

ISBN

9798173785930

Author

Harkins, Kieren Anika

Publication Date

2026-08-10

Peer reviewed|Thesis/dissertation

eScholarship.org Powered by the California Digital Library
University of California

Methods of Transverse Lifetime Extension in Nuclear Spins

by

Kieren Anika Harkins

A dissertation submitted in partial satisfaction of the

requirements for the degree of

Doctor of Philosophy

in

Chemistry

in the

Graduate Division

of the

University of California, Berkeley

Committee in charge:

Professor Ashok Ajoy, Chair
Professor David Wemmer
Professor Jeffrey A. Reimer

Summer 2026

Methods of Transverse Lifetime Extension in Nuclear Spins

Copyright 2026
by
Kieren Anika Harkins

Abstract

Methods of Transverse Lifetime Extension in Nuclear Spins

by

Kieren Anika Harkins

Doctor of Philosophy in Chemistry

University of California, Berkeley

Professor Ashok Ajoy, Chair

Spin is a fundamental behavior common to almost all of the building blocks of matter, from subatomic particles, to electrons and atoms. Interaction with a magnetic field can manipulate this behavior to reveal insights about the world around us, such as studying chemical bonds through Nuclear Magnetic Resonance (NMR) or performing computations via quantum computing. However, interactions between spins limit their coherence, returning the system to a state governed by thermal equilibrium conditions. This thesis focuses on a model system of ^{13}C nuclear spins in nitrogen-vacancy (NV) center doped diamond to study methods by which the coherence of spins can be extended or manipulated. These methods include cooling the thermal equilibrium conditions by hyperpolarization, temperature, and laser illumination on electron spins of the NV centers in the sample. To this end, a novel instrument capable of integrating all three of these methods was developed and constructed. In addition, other methods of extending spin lifetimes including pulse sequence modification were employed, finding that the addition of fields from either the electron spins in the sample or an external radio-frequency (RF) transmitter could extend or shorten the lifetimes controllably.

To Mom and Dad

For all of the dinnertime conversations which encouraged me to remain curious.

Contents

Contents ii

List of Figures iv

Acknowledgments vi

I Introduction 1

1 Introduction 2
- 1.1 Introductory Concepts in Nuclear Magnetic Resonance . . . 2
- 1.2 Basics of Hyperpolarization . . . 3
- 1.3 DNP with Nitrogen Vacancy (NV) Diamonds . . . 4
- 1.4 NMR Spinlock Measurement Protocol . . . 6
- 1.5 Objectives of Dissertation . . . 8
- 1.6 Dissertation Overview . . . 9

II Novel Instrumentation 10

2 Development of Novel Cryogenic Field-Cycling Instrumentation 11
- 2.1 Instrumental Overview . . . 12
- 2.2 DNP-NMR Probe . . . 13
- 2.3 Optical Illumination . . . 16
- 2.4 Cryogen Delivery Compatible with Shuttling . . . 17
- 2.5 Device Synchronization and Control . . . 19
- 2.6 Avenues of Future Development . . . 21

III Spin Temperature Control 33

3 Cryogenic Cooling of Sample Temperature 34
- 3.1 Temperatures from RT - 77 K . . . 35

3.2 Preliminary Studies at ∼10 K 37
3.3 Instrumental Limitations 37

4 Hyperpolarization-based Cooling of Spin Temperature 42
4.1 Overview 42
4.2 DNP at low temperature 43
4.3 Variation of DNP length 44

5 Laser-Induced Manipulation of Spin Lifetimes 48
5.1 Experimental Modifications 49
5.2 Continuous Laser Application 49
5.3 Block Laser Application 51
5.4 Extensions to Decoherence Model 53

IV Pulse Sequence Control 57

6 Development of Hyperpolarized "Shells" 58
6.1 Method of Hyperpolarization Injection 59
6.2 Method of Hamiltonian Engineering 63
6.3 Interrupted Driving 66
6.4 Orientation Dependence 67
6.5 Temperature Dependence 68
6.6 Experimental Sequence Dependence 68
6.7 Theoretical Results 70
6.8 Discussion 72

7 Transmitter Offset Engineering of Protected Spinlock Axis 86
7.1 Adaptation of Experimental Protocol 87
7.2 Laplace Inversion 88
7.3 Magic Angle Decoupling 92
7.4 Small Tip Angle Lifetime Extensions 95
7.5 Application for AC Sensing 97

V Conclusion 115

8 Conclusion 116

Bibliography 117

List of Figures

2.1 **Overview of the instrument** . . . 27
2.2 **Field map indicating variation in magnetic field** . . . 28
2.3 **DNP/NMR Probe** . . . 29
2.4 **Control and synchronization of the instrument** . . . 30
2.5 **Closed-cycle liquid helium system** . . . 31
2.6 **CAD image of goniometer prototype** . . . 32

3.1 **Calculated spin polarization as a function of temperature** . . . 38
3.2 **Probing hyperpolarized ^{13}C nuclei at 100 K** . . . 39
3.3 **Comparison of spin-lock decay from RT to 85 K** . . . 39
3.4 **Comparison of spinlock decays at cryogenic temperatures** . . . 40
3.5 **Field-cycling relaxometry with hyperpolarized nuclei** . . . 41
3.6 **Spinlock measurements down to ~ 10 K** . . . 41

4.1 **Comparison of spinlock signals of hyperpolarized and thermally polarized states** . . . 45
4.2 **EPR mapping of NV electrons via DNP** . . . 46
4.3 **Signal S vs time with differing hyperpolarization build-up times** . . . 47

5.1 **Effect of laser application on spinlock dynamics** . . . 55
5.2 **Investigating rate of laser-induced decay** . . . 56

6.1 **Spin textures created via hyperpolarization injection** . . . 74
6.2 **Melting of initial state spin texture due to spin diffusion** . . . 75
6.3 **NV-mediated gradient potential to form stable "shell-like" textures** . . . 76
6.4 **Formation of zero-crossing behavior from Hamiltonian Engineered drives** 77
6.5 **Data for a wide range of spinlocking angles** . . . 78
6.6 **Comparison of State and Hamiltonian Engineering signal magnitude** . . . 79
6.7 **"Interrupted" periodic driving experiments** . . . 80
6.8 **Formation of "Hamiltonian Engineered" spin texture for two different sample orientations** . . . 81
6.9 **Effect of temperature on "Hamiltonian Engineered" spin-shell profile** 81

6.10 **Effect of hyperpolarization injection τ_+ on "Hamiltonian Engineered" spin-shell texture** . . . 82
6.11 **Variation of "Hamiltonian Engineered" spin shell with pulse duty cycle** 83
6.12 **Effect of frequency offset on "Hamiltonian Engineered" spin shell formation** . . . 84
6.13 **Simulations of spin texture formation** . . . 85

7.1 **Estimation of flip angle** . . . 102
7.2 **Decrease in signal with initial pulse** . . . 103
7.3 **Example S-Curve for α analysis** . . . 104
7.4 **Impact of regularization parameter α on Laplace Inversion** . . . 105
7.5 **Effect of noise on Laplace Inversion** . . . 106
7.6 **Effect of truncating data on Laplace Inversion maps** . . . 106
7.7 **T_2' lifetime extension due to frequency offset.** . . . 107
7.8 **Variation of T_2' as a function of interpulse spacing τ** . . . 108
7.9 **LI as a function of offset for high interpulse spacing** . . . 108
7.10 **LI maps as a function of pulse train pulse width and transmitter offset** 109
7.11 **Anomalously long T_2' lifetimes with small-angle pulses** . . . 110
7.12 **Full decay for longest T_2' spin lifetime** . . . 111
7.13 **Signal loss due to tilted prethermal axis** . . . 112
7.14 **Long-time quantum sensing at room temperature** . . . 113
7.15 **Magnitude of discrete Fourier transform for frequency swept AC field** 114

Acknowledgments

The pursuit of a Ph.D. is, in many ways, a solitary journey. Becoming an expert in an increasingly niche field of study means that many of my struggles become deeply personal experiences. Through it all, I am grateful to have a community who has encouraged, supported, cheered for, questioned, and inspired me to continue through all those moments. For all of you who were on this journey with me, thank you.

I would like to begin by thanking my advisor Professor Ashok Ajoy. You took a chance on me when I was just a first-year student who had only ever heard of NMR in organic chemistry courses and you committed to teaching me how to build my own NMR instrument and explore the field of magnetic resonance. I am grateful for the opportunities for scientific and personal growth that my time in this lab have provided as well as the opportunity to apply for the NSF GRFP which has funded much of this work.

I am deeply grateful to Professor Jeff Reimer. You created a space within your group and within our discussions where curiosity and belonging were the focus. You taught me that science should be just as much about community as it is discovery and your wisdom and input across the years have given me an invaluable perspective. Thank you.

I also want to thank my third committee member, Professor David Wemmer. I appreciated your advice and guidance, especially during my qualifying exam and the completion of this dissertation. Thank you as well to my many collaborators across the years. Your patience and guidance have taught me many lessons.

I am deeply grateful for my postdoctoral mentors who shaped my PhD and guided my growth both as a scientist and a better person. David, your mentorship when I arrived as a first-year graduate student taught me the most about problem-solving and the tenacity needed to succeed in science. Shira, your friendship taught me the importance of resilience and collaboration. Sophia, your joy around science was infectious; your curiosity and generosity reminded me why I fell in love with science to begin with. Together, the three of you have taught me to become a better scientist and friend.

I truly don't know what my Ph.D. journey would look like without Noella. You've been my coworker and bestie since Day 1, racing me to both the bottom and the top. You've been the best office mate, instrument buddy, and true friend. Will, Ozgur, and Zack, I have learned so much from all of you. You made this lab a wonderful place to work and your insight over the years taught me so much. To my colleagues, my coworkers, my 400 subgroup Cooper, Chaitali, and Leo: thank you for yapping with me in the office and sharing our very

temperamental instrument. I can't wait to see what you accomplish. Manny, you have been a 'lab dad' to so many of us, sharing engineering wisdom and life lessons alike. Thank you for always having a fun tidbit to share and inspire us with. My undergraduate researchers: Samantha, Angad, and Aris—you have taught me so much about teaching and mentorship. Thank you for muddling through my attempts to give you meaningful research tasks and listening to me get on my soapbox about distinctly non-scientific topics.

Our little Ajoy lab group has grown to too many graduate students, postdocs, postbacs, and visiting students for me to thank by name. All of you, past and present, have taught me and encouraged me along the way and I am so grateful to you. The Reimer group, as well, have welcomed me with open arms. Thank you for your community and support, both of which are truly unmatched.

A special shout-out goes to Joseph and Brooke. Your friendship, both at work and beyond, has supported me and encouraged me in all aspects of my life. I will miss our support group group chat and I'm so unbelievably proud to be able to call you my friends.

There are few people who I can call on for anything, but Wendy you are one of them. Our topics over the years have ranged from boys to climbing to quantum mechanics (I genuinely don't think I would have passed our first-year QM class without you) and our dedication to feeding each other weekly dinners has blossomed into a lifelong friendship. Thank you for being there for me, week after week, throughout our entire time at Berkeley.

There are countless more people here in Berkeley who I count among my truest friends. To all of you—thank you. Your friendship, be it at the gym, in the ceramics studio, at softball, during recruitment, from GSIing with me, or however else I've met you, has touched my heart. I will never forget all of your encouragement.

To my undergraduate advisors Prof. Hanson and Prof. Byers: Your excitement for science, your passion for teaching, and your care for your students are the reasons I am on the journey to begin with. I hadn't even thought about a Ph.D. until you showed me how cool something like that could be. I'm not sure I will ever be able to say thank you enough for teaching me how to do research, for encouraging my curiosity about different fields, and most of all for helping take the first steps on this Ph.D. journey.

To my partner Tyler, thank you for coming into my life and reminding me that though a Ph.D. is about doing research, life is about so much more. Your love has encouraged me to grow in confidence and find more joy. I can't wait for our next chapter together!

Max, thank you for being the best brother. From offering to read my dissertation to offering up your spare bedroom if I needed a place to write, I know I have your support. Becca, I am so grateful for our broad scientific conversations about anything we can think of. And to the rest of my family, I love you! Thank you!

Finally, and most importantly, thank you Mom and Dad for loving me unconditionally. For all the late night FaceTimes over dinner. For making me re-explain my research over and over to you, for being curious about what I'm up to, and for inspiring me. The two of you have been my biggest cheerleaders for my entire Ph.D. There are not enough words in the world to describe how much your love and support has inspired and motivated me from way back in elementary school, all the way to here. I love you both so much.

Citations to Previously Published Work

Much of the work in this thesis is adapted from previously published work. In order of appearance:

Chapter 2 is adapted from the following paper:
Noella D'Souza,* **Kieren A Harkins**,* Cooper Selco, Ushoshi Basumallick, Samantha Breuer, Zhuorui Zhang, Paul Reshetikhin, Marcus Ho, Aniruddha Nayak, Maxwell McAllister, Emanuel Druga, David Marchiori, Ashok Ajoy. "Cryogenic field-cycling instrument for optical NMR hyperpolarization studies". In: *Journal of Magnetic Resonance* **375** (28 Mar. 2025), p. 107847. DOI: 10.1016/j.jmr.2025.107874 URL: https://www.sciencedirect.com/science/article/pii/S1090780725000461?via%3Dihub

Chapter 6 is adapted from the following paper:
Kieren A Harkins,* Christoph Fleckenstein,* Noella D'Souza,* Paul M. Schindler,* David Marchiori,* Claudia Artiaco, Quentin Reynard-Feytis, Ushoshi Basumallick, William Beatrez, Arjun Pillai, Matthias Hagn, Aniruddha Nayak, Samantha Breuer, Xudong Lv, Maxwell McAllister, Paul Reshetikhin, Emanuel Druga, Marin Bukov, Ashok Ajoy. "Nanoscale Engineering and Dynamical Stabilization of Mesoscopic Spin Textures". In: *Science Advances* **11** (28 Mar. 2025). DOI: 10.1126/sciadv.adn9021. URL: https://www.science.org/doi/10.1126/sciadv.adn9021.

Chapter 7 is adapted from the following preprint:
Kieren A Harkins,* Cooper Selco,* Christian Bengs, David Marchiori, Leo Joon Il Moon, Zhuo-Rui Zhang, Aristotle Yang, Angad Singh, Emanuel Druga, Yi-Qiao Song, Ashok Ajoy. "Anomalously Extended Floquet Prethermal Lifetimes and Applications to Long-Time Quantum Sensing". In: *arXiv* (11 Oct. 2024) DOI: 10.48550/arXiv.2410.09028 URL: https://arxiv.org/abs/2410.09028

Part I

Introduction

Chapter 1

Introduction

1.1 Introductory Concepts in Nuclear Magnetic Resonance

Nuclear Magnetic Resonance (NMR) is a widely used analytical technique to study molecules. Taught in almost every undergraduate organic chemistry course, NMR is a workhorse technique for many organic chemists as it provides a fingerprint of the connectivity of molecules.

NMR, as its name suggests, utilizes magnetic fields to study nuclei via their spin. In a strong magnetic field, spin angular momentum causes a nucleus to precess around that field. In a bulk sample, the coherent precession of these nuclei results in a bulk magnetization that can be detected through an induced radio-frequency (RF) current in a pickup coil. This is the basis for NMR measurements.

Nuclei in different environments precess differently from each other. For example, a ^{1}H nucleus in proximity to an electronegative atom will suffer from "deshielding" where the nearby electrons are, on average, further away from the ^{1}H nucleus in question. This alters the precession frequency, rendering measurement of this precession a useful tool for describing the local environment and connectivity. With sufficient frequency differentiation between precessions, which can be created by a high magnetic field environment, NMR is a powerful way to identify molecules with great detail.

A drawback of NMR is the fact that the measurement is intrinsically related to the spin angular momentum. In conventional laboratory magnets, this yields a very small energy level difference, which gives rise to a well-known limitation in NMR — poor sensitivity of the technique due to low polarization at typical thermal equilibrium conditions.

As we describe a typical NMR experiment, this issue becomes readily apparent. In order to generate a bulk magnetization that is detectable as described above, the nuclear spins must become aligned with the field. We will do this by placing a simple sample of spin-1/2 nuclear spins in a magnetic field, where they preferentially align in the same direction as the magnetic field: the lowest energy state. However, the small energy level difference between the spin angular momentum states means that the other orientation (against the magnetic

field direction) is only slightly higher in energy. The populations of these states can be described by the Boltzmann factor:

$$\frac{p_\uparrow}{p_\downarrow} = e^{\frac{E_\downarrow - E_\uparrow}{(k_\mathrm{B}T)}} \tag{1.1}$$

where $k_\mathrm{B}T$ gives the thermal energy of the surroundings. In the magnetic field where the difference in energy levels of the states $\Delta E = \hbar\gamma B$, the polarization can thus be calculated. At high temperatures, this can be approximated for simplicity.

$$Pol = \tanh\left(\frac{\hbar\gamma B}{2k_\mathrm{B}T}\right) \approx \frac{\hbar\gamma B}{2k_\mathrm{B}T} \tag{1.2}$$

From the Boltzmann distribution, we can see that the small energy level difference of the two spin states creates a minuscule polarization — for a carbon nucleus described later in this dissertation at a typical high-field magnet strength of 9.4 T, this is only 8×10^{-6}. We can also see that the energy level splitting depends on the gyromagnetic ratio (γ) of the nucleus (an intrinsic property), the field strength B (hence the choice of a high-field magnet in which to put our samples), and the temperature. Indeed, working with higher γ nuclei and performing NMR at higher magnetic fields or lower temperatures results in higher polarization and thus higher sensitivity. However, not all samples are suitable for measurements at colder temperatures, very high magnetic fields remain difficult to achieve, and sometimes the nuclei of interest in the sample will simply have a low γ. Hyperpolarization, or the establishment of spin population differences much greater than normally achievable by thermal means, is an attractive solution.

1.2 Basics of Hyperpolarization

The practice of hyperpolarization has been around for decades [140, 40, 177, 72, 61], with many innovative methods to realize high spin population differences. Here, we define hyperpolarization as the generation of population ratios of up to several orders of magnitude [120, 61], resulting in a dramatically increased signal. There are many such methods which do this; some even considered conventional NMR, such as cross polarization (CP) [146]. Indeed, the methods of hyperpolarization vary wildly and frequently depend on the identity of the sample; cross polarization is an easily accessible technique for many organic molecules as it relies on hydrogen nuclei which are in contact with nearby ^{13}C nuclei.

In this dissertation, we will focus on the practice of dynamic nuclear polarization (DNP) which relies on proximal electrons to polarize nuclei of interest [4, 177]. With a gyromagnetic ratio of 28.0 GHz/T, electrons naturally have 660 times greater polarization than protons and 2600 times greater polarization than ^{13}C nuclei under the same thermal and magnetic field conditions. Indeed, electrons are ubiquitous throughout materials and many methods have been studied so that the electrons can be brought into contact with the nuclear spins to create a transfer of spin order. A brief flavor of these techniques includes: dissolution

DNP (dDNP) [17, 18, 93, 34], Overhauser DNP [140, 6, 151], solid-state MAS-DNP [26, 134, 161], optical/triplet DNP [59, 136, 69, 71, 58, 75], and optical NV-DNP [99, 66, 157, 92, 143, 13]. For the purpose of this dissertation, we will narrow our focus to optical DNP of NV diamonds, although we will gesture towards potential applications which involve triplet DNP.

1.3 DNP with Nitrogen Vacancy (NV) Diamonds

NV diamonds (more accurately labeled as NV^- diamonds) are an ideal model system in which to probe studies of spin lifetimes. As diamonds, they have a rigid, well-ordered lattice of carbon atoms with few impurities. Based on growth conditions, these diamonds can range in concentration of ^{13}C nuclear spins, from a natural abundance of 1.1% to fully enriched at $\sim 100\%$ abundance [128]. This allows for tunable properties of the nuclear spins, including dipolar coupling length scales.

As a solid, and at natural abundance, ^{13}C nuclear spins in NV diamond are known to have long T_1 lifetimes and short T_2 lifetimes [156, 155, 169]. This combination of lifetimes presents a challenge in typical NMR experiments; however, we will describe how these can be advantageous (or at least, rendered inapplicable) to this work. Typical NMR measurements rely on the build-up of thermal polarization in a high magnetic field, thus a long T_1 requires experiments to take a prohibitively long time. With optical hyperpolarization as the primary method of polarization build-up, this T_1 instead becomes an advantage as it enables high levels of polarization build-up and prolongs the non-thermal hyperpolarized state that has been achieved. The short T_2 lifetime of a solid, in conventional NMR, leads to broad linewidths due to strong dipolar couplings between neighboring nuclei [124]. These are dependent on position and angle from the magnetic field vector; in liquids, molecular tumbling leads to averaging of these angles and mitigation of this effect, but rigid solids with fixed angles and atomic locations suffer from the full effects of dipolar coupling [79, 124, 16]. In this dissertation, it is not necessary to distinguish fine structural features of the NV diamond; we are considering the bulk sample with one type of nuclear spin species. Furthermore, we can tune the strength of these dipolar couplings through the abundance of ^{13}C nuclei in the sample; experimental data shown in this work use only natural abundance (1.1%) ^{13}C nuclei in diamonds. Finally, the decreased measurement time resulting from the short T_2 lifetime will be addressed through the driving protocol detailed in the next section, Section 1.4.

More importantly for DNP, NV diamonds have a useful defect whose electrons can be optically targeted. Here, a nitrogen atom substitutes for a carbon within the diamond lattice, while a lattice vacancy is simultaneously introduced at one of the four proximal carbon sites, resulting in the NV^- defect [54]. Notably, the ground state of the NV^- center is a triplet state, with $m_s = 0$, $m_s = 1$, and $m_s = -1$ sublevels. Optical excitation of the NV^- center by 532 nm laser promotes the system to the triplet excited state; it can then radiatively decay thereby emitting fluorescence, or perform an intersystem crossing through

the singlet state as it relaxes. When performing the intersystem crossing, the pathway from the $m_s = \pm 1$ through the singlet state, ending in the $m_s = 0$ sublevel is strongly preferred over the pathway from the $m_s = 0$ to the $m_s = \pm 1$ sublevels. This results in a polarization increase in the $m_s = 0$ sublevel through simple optical illumination [54, 168, 121].

Polarization generated on the electrons must be transferred to nuclear spins so that it can be used in an NMR context. Here we summarize the method of hyperpolarization which was elucidated in Ref. [168]. This method is used throughout this dissertation as the primary method of hyperpolarization. Microwave (MW) radiation is swept across the electron linewidth, traversing a set of level anticrossings between the electron and nuclear spins. Consider that in the NV diamond system the NV electrons can be in states $m_s = 0$ and $m_s = \pm 1$ while the ^{13}C nucleus can be in states $\alpha = \uparrow$ or $\alpha = \downarrow$. Furthermore, a majority of the electrons will be in state $m_s = 0$ due to the optical polarization described above. Since the energy gap between the electron states is larger than that of the nuclear states, the energy gap in the level anticrossing diagram will follow suit. If traversed adiabatically with respect to the larger energy gap and diabatically with respect to the smaller energy gap, the system will hyperpolarize the nuclei to the state $\alpha = \uparrow$ [10]. Continued application of the laser re-initializes the electrons to the $m_s = 0$ state allowing sequential traversals of the level anticrossings until bulk polarization of the nuclear spins in the $\alpha = \uparrow$ state is achieved. A further description of the complexities arising from the broad electronic spectrum and multiple nuclei coupling to a single electron are described in Ref. [145].

The frequency of the MW sweeps is centered on the ESR frequency of the NV transition; both the transition type ($m_s = 0$ to $m_s = 1$ or $m_s = 0$ to $m_s = -1$) and field at which the MW sweeps are applied will alter the center frequency necessary to perform hyperpolarization. This choice of field and transition allows NV diamonds to be polarized with readily available commercial MW sources that are capable of producing sufficiently high power to maintain the adiabatic and diabatic conditions for hyperpolarization [11]. More discussion on the field requirements and associated experimental choices for the specific experiments described herein will be presented momentarily in Chapter 1.4 and in Chapter 2. The complex interplay of MW power, laser power, and chirping speed, which affect adiabaticity constraints has been previously published in Ref. [168] and we will assume that we are working within a near-optimal range in the following work.

NV diamonds are therefore an ideal system in which to work, as they are capable of generating high levels of nuclear polarization (approx. 0.6% in a bulk single crystal [23]). These levels are generated in <90 s per shot when well optimized [168]; a dramatic decrease in experimental time needed compared to the ∼5 hours necessary to generate thermal polarization. When considering the ∼100-fold boost in SNR achieved by hyperpolarization, approximately 100,000 thermal measurements would have to be averaged to yield the same SNR. Here is where the dramatic effect of hyperpolarization can be seen to its full extent: effectively, one hyperpolarized measurement is equivalent to over 57 years of continuous thermal measurements.

NV diamonds have another advantageous aspect: their relative simplicity, especially when used as a single crystal. Predominantly a diamond lattice composed of carbon, the

doping of spin-active ^{13}C nuclear spins can be controlled while NMR-silent ^{12}C nuclear spins make up the rest of the lattice. Other components in the NV diamonds include the NV^- defects used for hyperpolarization, as well as nitrogen substitutional defects left over from the formation of the NV centers [54]. These nitrogen substitutional defects will be referred to as P1 centers. As the hyperpolarization stems from the NV center, the NMR "visible" spins will be arranged in a centrosymmetric manner, with the NV center in the middle. Indeed, a good description of this can be found in Ref. [24]. The P1 centers, arranged randomly, are treated both in Ref. [24] and in this work as a cumulative background effect across the sample. This is a direct consequence of the bulk observation of centrosymmetric systems: individual centrosymmetric universes may have a few P1 centers affecting local relaxation dynamics, but they are averaged into a background effect when considering the ensemble of all the hyperpolarized NV centrosymmetric universes across the diamond sample. More consequences of the centrosymmetric NV center structure will be explored in Chapter 6 of this dissertation.

1.4 NMR Spinlock Measurement Protocol

The method for all experiments described herein is as follows: first, optical NV-based hyperpolarization is performed in the fringe field of the magnet. This reduces instrumentation requirements for the MW frequency, allowing application of high-power MW at the appropriate frequency chirp with commercially available and relatively inexpensive instruments. Next, the sample is shuttled from the fringe field to the high field center of the magnet. In the built instrument, described in Chapter 2, this process takes ∼90 s. Finally, an NMR "pulsed spinlock" experiment is performed.

The pulsed spinlock experiment consists of an initial $\hat{\mathbf{y}}$ pulse (typically $\sim\pi/2$) followed by a train of $\hat{\mathbf{x}}$ θ pulses with spacing τ [139, 159, 158]. Notably, this pulse sequence results in a dramatic increase in transverse nuclear spin lifetime, as is described in Ref. [25]. This pulse sequence is of primary use in this work for that reason, with modifications and tweaks as described in Chapter 6 and Chapter 7.

In the simplest vector picture, this sequence effectively tips the nuclear spins from the $\hat{\mathbf{z}}$ axis to the $\hat{\mathbf{x}}$ axis and then applies fast radio-frequency (RF) pulses, creating a weak RF field which maintains the spins along the $\hat{\mathbf{x}}$ axis. The use of pulses for this spinlock opens up short windows of measurement in which the spins can be observed.

A more mathematical description of the action of the spinlock sequence can be found in Refs. [25, 8]. Briefly put, the spinlock sequence creates an average Hamiltonian [79] that commutes with the initial state of the system along $\hat{\mathbf{x}}$, to a first order approximation.

The first pulse along $\hat{\mathbf{y}}$ tips the spins to result in the initial condition:

$$\rho(0) = \sum_j c_j I_{jx} \tag{1.3}$$

Let us then consider the spinlock sequence. The spins will experience a large effect from the high magnetic field they are in, but this Zeeman Hamiltonian can be treated by entering the rotating frame, thus simplifying the following treatment. At the core of the spinlock sequence, the nuclear spins will experience a Hamiltonian from the RF pulses, as well as an interaction between the nuclear spins, governed by the dipolar Hamiltonian:

$$\mathcal{H}_{\text{dd}} = \sum_{j<k} d_{jk}^{CC} \left(3I_{jz}I_{kz} - \mathbf{I}_j \cdot \mathbf{I}_k\right) \tag{1.4}$$

where $d_{jk}^{CC} = \frac{\mu_0}{4\pi}\frac{\hbar\gamma_C^2}{r_{jk}^3}(3\cos^2(\beta_{jk}) - 1)$ is the constant dipolar coupling strength between any two nuclei j and k. Here, r_{jk} is the distance between the two nuclei and β_{jk} is the angle between the internuclear vector and the magnetic field. For N pulses, these Hamiltonians can be arranged sequentially to give a total Hamiltonian:

$$\mathcal{H}_{\text{tot}} = \left(\mathcal{H}_{\text{rfx}}\mathcal{H}_{\text{dd}}\right)^N \tag{1.5}$$

For mathematical simplicity, we consider all RF pulses to be equally spaced delta pulses of tip angle ϑ with time τ between two pulses under which free evolution under the dipolar Hamiltonian is occurring.

We establish a time development operator $U(t, 0)$ such that

$$|t\rangle = U(t, 0)\,|0\rangle \tag{1.6}$$

and for short time steps,

$$U = e^{-i\mathcal{H}t} \tag{1.7}$$

Thus, we can write

$$\left(U_{rfx}U_{dd}\right)^N = \left(e^{i\vartheta I_x}e^{i\mathcal{H}\tau}\right)^N \tag{1.8}$$

A clever expansion reveals the following:

$$\begin{aligned}\left(U_{rfx}U_{dd}\right)^N &= e^{-i\vartheta I_x}e^{-i\mathcal{H}\tau}e^{i\vartheta I_x}e^{-2i\vartheta I_x}e^{-i\mathcal{H}\tau}e^{2i\vartheta I_x}e^{-3i\vartheta I_x}\ldots \\ &= \prod_n^N \exp(-i\tau\left(e^{-in\vartheta_x I_x}\mathcal{H}_{\text{dd}}e^{in\vartheta_x I_x}\right))\end{aligned} \tag{1.9}$$

which eventually resolves via a Magnus expansion to

$$\left(U_{rfx}U_{dd}\right)^N = \exp(-i\tau\sum_{j<k} d_{jk}^{CC}\left(\frac{3}{2}(I_{jy}I_{ky} + I_{jz}I_{kz}) - \mathbf{I}_j \cdot \mathbf{I}_k\right)) \tag{1.10}$$

This resolution can be neatly demonstrated by hand in the case where $N = 4$ and $\vartheta = \pi/2$; however, it is generally applicable.

We note that extracting the average Hamiltonian from this evolution yields:

$$\overline{\mathcal{H}}_{\text{ave}} = \sum_{j<k} d_{jk}^{CC} \left(\frac{3}{2} \mathcal{H}_{\text{ff}} - \mathbf{I}_j \cdot \mathbf{I}_k \right) \tag{1.11}$$

which contains the flip-flop Hamiltonian $\mathcal{H}_{\text{ff}} = I_{jy} I_{ky} + I_{jz} I_{kz}$.

This average Hamiltonian can be demonstrated to commute with the initial state of the system (Eq. 1.3) indicating that, by the Liouville-Von Neumann equation, the time derivative is zero. Thus the initial state, to the leading order approximation, does not change in time. This, fundamentally, is the protection under which the pulsed spinlock sequence works.

On its face, this sequence works for any ϑ_x pulse length. However, the shorter ϑ_x is, the more pulses must be applied for a given N, and thus the longer the period of the Floquet cycle must be. The accumulation of higher order terms and pulse imperfections weaken the drive, shortening the T_2' relaxation time. For this reason, typical ϑ_x pulses are $\sim\pi/2$ [139]; effects that arise due to the choice of $\vartheta_x \neq \pi/2$ are part of the modifications to the pulse sequence which are discussed in Chapter 6 and Chapter 7.

Between the pulses, we rapidly interrogate the ^{13}C Larmor precession. This quasi-continuous sampling is a key benefit to the pulsed spinlocking technique, as it offers a way to investigate the spin dynamics as the spinlock progresses over time. We record the nuclear polarization amplitude S and phase φ_R in the $\hat{\mathbf{x}}$-$\hat{\mathbf{y}}$ plane in the rotating frame; the majority of figures shown in this thesis demonstrate a plot of S vs experimental time. Further details of sampling and experimental data collection are included in Chapter 2.

1.5 Objectives of Dissertation

The primary goals of this dissertation are to investigate the causes and methods to control transverse relaxation times in hyperpolarized diamond ^{13}C nuclear spins. The length of relaxation time is both a benefit and a detriment to researchers across myriad fields studying spin. Thus, the control of this relaxation time and ability to uniquely modify and preserve the spin states is of paramount importance. This dissertation seeks to advance and deepen our understanding of nuclear spin relaxation.

Achievement of these goals is predicated on a secondary goal: advancement of instrumentation in the field of field-cycling hyperpolarization. The construction of a novel, cryogenically-capable instrument detailed in Chapter 2 is indeed the fundamental advancement upon which the rest of this dissertation is built.

Several of the chapters included here, including Chapter 5 are incomplete works, having been built on and investigated by subsequent colleagues. The work as it is presented here explores questions arising from original datasets we have collected but leaves more comprehensive treatments and complete results to the authorship of these colleagues. Where appropriate, a discussion of these colleagues' results is included with citation.

1.6 Dissertation Overview

This dissertation is organized into three sections that address different aspects of the methodology of the control of nuclear spin relaxation times. The first section, Part II describes the custom instrument that was built over several years in order to facilitate the studies done in the rest of this dissertation. Attention is paid in Chapter 2 to the addition of cryogenic operation and the experimental concerns that were overcome. The final section of Chapter 2 notes additional improvements to the instrument that could be made (or, indeed, are in the process of being made) to contribute to future work.

The following two sections, Parts III and IV describe data taken pursuant to the development of the control of nuclear spin lifetimes. These are split largely by the method of the control. Part III focuses on various methods in which spin temperature can be altered. The most straightforward approach of simply cooling the sample is covered in Chapter 3. A review of another readily apparent method of changing the spin temperature through hyperpolarization is presented in Chapter 4. Finally, Chapter 5 details an interesting application of laser to affect the spin temperature as well as musings of certain questions it raises, to be addressed in work by other colleagues.

Part IV instead focuses on controlling spin lifetimes through pulse sequence development. Here, Chapter 6 describes novel behaviors that arise in the sample as a consequence of the ϑ pulse-train pulse lengths approximating π. The ultimate formation of stable spin polarization "shell" structures provides a counter-intuitive picture of polarization and spin lifetime extension. Finally, Chapter 7 details the longest spin lifetimes reported in these systems of NV diamonds, achieved through protecting a small-angle spinlock axis.

Part II

Novel Instrumentation

Chapter 2

Development of Novel Cryogenic Field-Cycling Instrumentation

In addition to NV diamond systems [65, 14, 13], optical DNP is being actively explored across a wide array of systems, including: *(i)* semiconductors such as SiC [64, 91], *(ii)* organic molecules hosting triplet-polarizable electrons (e.g. pentacene [187, 86, 175, 126], porphyrins [82], and derivatives [167]) and sensitizer-acceptor pairs via optical CIDNP [50], and *(iii)* molecular complexes with rare earth inorganic (REI) centers [22, 109]. The latter two classes are particularly interesting due to their synthetic tunability. Chemical modification can enable precise control over properties such as polarization agent spacing and topology, potentially enabling the development of custom-designed, bottom-up engineered molecular frameworks optimized to host polarization sources [199].

With these various materials comes a diversity in electron polarizability and in nuclear T_1 relaxation times. Even within one material, there exists a large variation in these relaxation times as a function of both magnetic field (B) and temperature (T) [70, 104]. This motivates the need for tools to be able to probe nuclear hyperpolarization across a range of B and T conditions.

This chapter details the development of a novel instrument that enables optical DNP studies across a broad range of temperatures (from room temperature to ∼77 K) and magnetic fields (10 mT to 9.4 T). While all data shown in this thesis are demonstrated on a model system of ^{13}C nuclear spins in diamond, this device would be easily adaptable to a wide range of materials and DNP applications.

The core methodology is that of "cryogenic field cycling", which involves shuttling a sample within a cryostat between a low-field polarization region and a high-field NMR detection region. Field-cycling in NMR has a storied history, beginning with important contributions by Pound, Ramsey, Purcell and many more in the 1950s [147, 150, 149, 5]. Notable applications in the late 1950s and early 1960s included the measurement of nuclear relaxation in superconductors, building the basis for NMR field-cycling relaxometry [87, 152, 15]. However, in their original form, these experiments were limited by the magnetic field values they could attain with only an electromagnet. Field-shuttling experiments using superconducting

magnets quickly followed [77, 198]. This technique has further been refined and advanced in the last several decades for both field-cycling NMR [102, 201, 101, 153, 42, 46, 81, 43, 44, 76, 11] and field-cycling relaxometry [98, 181].

Our approach builds on these efforts by integrating two key advancements: the ability to maintain samples at sustained cryogenic temperatures down to ∼77 K and possibly even ∼10 K, while performing field cycling and simultaneous optical excitation, and the ability to perform nuclear spin manipulations involving millions of pulses, even under these cryogenic conditions. A tradeoff for the broad temperature range and enhanced spin control capabilities our system provides is slower shuttling speeds than achievable in some of these setups [42, 43]; however, our shuttling speeds are sufficient for the sample types that we are studying in this thesis. This limitation, due to eddy currents from moving a cryostat into a magnet, will be detailed further in Section 2.1.

In this chapter, we will describe the design, construction, and operation of this instrument. This chapter is largely based on Ref. [49] and must acknowledge significant contributions from N. D'Souza and Dr. D. Marchiori as equal co-authors.

2.1 Instrumental Overview

The instrumental operation centers around the mechanical shuttling of a cryostat from low-field to high-field conditions under continuous flow cryogenic cooling (see Figure 2.1A). This allows the sample of interest to be hyperpolarized via MW-driven optical DNP at low magnetic fields before being shuttled into a high-field (9.4 T) magnet for NMR readout. This field-cycling instrument builds on the system previously built in Ref. [11], with the primary addition of operation down to cryogenic temperatures ∼77 K. This is enabled by several innovations, described in this chapter, which account for the extra weight of shuttling the cryostat and probe, the presence of eddy current forces, and the continuous replenishment of cryogen to maintain constant sample temperature regardless of cryostat position.

An aluminum extrusion frame, built around the NMR magnet, hosts a belt-driven actuator (Parker HMRB08) with excellent longitudinal precision of (50 μm) (Figure 2.1B). The actuator carries a movable stage ("truck") on which the cryostat is mounted by two custom-designed clamps. While the top clamp is machined and carries the weight of the cryostat, the bottom clamp is tightened or loosened to optimize alignment of the cryostat in the magnet bore (Figure 2.1E). This alignment must be maintained to within 0.5° over the entire ∼600 mm path of travel due to the tight clearance of <2 mm between the cryostat outer walls and the bore of the magnet. The consequence of misalignment results in grinding between the cryostat and magnet bore, which is discussed further in Sections 2.3 and 2.4.

In physically attempting to shuttle the entire cryostat assembly, eddy current forces pose a significant challenge [45]. They oppose the shuttling motion and vary in magnitude proportionally to the gradient of the magnetic field encountered. Figure 2.2 illustrates the magnetic field strength and field gradient profile, relative to the sample's position. Notably,

the maximum force arises 186 mm before the sample achieves the NMR magnet's maximum field, or "sweet spot."

We address the effects of the eddy currents in two ways. First, we design the probe and cryostat for lightness and to eliminate the excess use of metals. The stainless steel cryostat body is used as an RF shield for the probe, eliminating the need for a typical, copper shield that has higher induced eddy current forces due to its higher conductivity. We also minimize the use of copper within the probe. For a more detailed description of the probe design, see Section 2.2. Second, we provide additional support to the actuator belt that performs the motion. We incorporate a high-torque gearbox to the shuttling motor (ACS) located at the top of the actuator belt, which adds an extra 10 lb of torque to enhance load-carrying capacity (Figure 2.1C). We also utilize a spring load balancer pulley system, which is directly attached to the shuttling truck, as a dynamically variable counterweight. This pulley system will act to counterbalance any additional forces beyond the set point of 33 lb, compensating for any eddy current forces which arise due to motion.

In our experimental setup, the magnetic field experienced by the sample is controlled by adjusting the vertical position of the cryostat within the magnet's fringe field. The field profile during the sample's journey is also shown in Figure 2.2.

The shuttling time between the hyperpolarization field (27 mT) and the readout field (9.4 T), with the cryostat moving at a fixed rate of 7 mm/s, is ∼91 s. This is significantly longer than comparable room-temperature devices (e.g., 0.6 s in Ref. [11]). However, at cryogenic temperatures, the nuclear spin relaxation times (T_1) are expected to be inherently longer. It is also known that T_1 is strongly field-dependent and typically short only at low fields [9], where a two-electron spin-flip process stemming from electrons in the sample dominates. This region is marked for the case of our sample of ^{13}C nuclei in diamond, up to 100 mT, in Figure 2.2. The most critical time scale, therefore, is the duration required to traverse the low-field regime (<0.1 T), where shorter T_1 values are expected. This traversal is completed in ∼22 s.

2.2 DNP-NMR Probe

Creating an instrument that shuttled a cryostat necessitated the development of a custom probe with the following constraints: (1) it must fit within the cryostat, (2) it must contain all the parts necessary to integrate the probe with the existing DNP methodology developed previously in the lab [145, 10, 13], and (3) it must be able to be tuned and impedance matched to 50 Ohms externally, while at cryogenic temperatures. In this design, the NMR probe supports microwave (MW) excitation at low fields in order to perform hyperpolarization as well as radio-frequency (RF) excitation and detection for performing NMR at high fields. The final design of the probe is laid out in Figure 2.3.

The two coils for MW and RF excitation were mounted perpendicularly to each other in order to minimize interference, as both must be in contact with the sample at different times during the experiment. The RF coil is designed in a saddle geometry and laser-cut

from a 0.7 mm copper sheet using a high-power (60 W) CO_2 laser (Figure 2.3E-G). This thickness of 0.7 mm was chosen as it was determined that thinner sheets (0.5 mm) were not robust enough to withstand the movement of the sample as it was mounted and removed, while thicker coils presented challenges in folding the geometry. Indeed, it is self-supporting in design, requiring no external support or structure to maintain its shape. The RF coil has a 12 mm internal diameter, which accommodates the sample mounted inside a 10 mm internal diameter flat-bottomed quartz test tube. Also located inside the saddle RF coil is the MW loop coil, approximately 8 mm in diameter on which the flat-bottomed test tube rested. Subsequent probe designs included a plastic O-ring that fit snugly around the test tube but had an outer diameter larger than the central opening of the puck, alleviating the weight of the sample tube on the MW coil. This MW loop coil is constructed from 18-gauge bare copper wire shorted to itself. Other successful MW loop coil designs use higher gauge shielded wire, which is shorted to the braided shield. A key to the success of both designs is the rigid mounting of the coil to avoid any movement. Introduction of vibrations in the MW coil would directly affect the NMR signal by introducing artifacts and high levels of noise. To ensure this rigid mounting, all probe designs used for these experiments relied on threading the MW coax to the base of the probe and restraining the coil against the inner hole of the bottom puck, either by tension, glue, floss, or a combination of the three.

It would seemingly be obvious that one would wish to separate the RF and MW coils in space in order to minimize the potential for interference and introduction of noise during experiments. An early design idea, which was explored and quickly discarded, was to place the RF and MW coils at different locations within the cryostat. However, this would create a situation in which either (A) two separate shuttling mechanisms would have to be introduced — one to shuttle the entire cryostat in and out of a magnet, and a separate smaller mechanism to shuttle the sample between the RF and MW coils — or, if the cryostat was not shuttled, (B) the hyperpolarization position would not be far enough out of the magnet to be at a mT fringe field, necessary for hyperpolarization with cost-effective, high power amplifiers. Indeed, moving the sample between two separate positions for the RF and MW coils at all would raise challenges surrounding the addition of noise while shuttling, and the changing temperature of the sample — cryostats are not able to maintain a constant temperature throughout the entire body, instead a small "sample well" is at the optimal temperature before the cryogen is returned. For all these reasons, it was determined that the RF and MW coils must be co-located leading to the "pill-box" design seen in Figure 2.3G.

In addition to integrating the MW coil into the probe design, accommodations had to be made to account for the laser necessary for optical DNP. These accommodations included: (A) the opening of a central aperture in all pucks making up the probe body (Figure 2.3A-C) and (B) the sample being mounted in a quartz test tube, with a notched quartz rod placed on top to ensure the sample's orientation and position were maintained (Figure 2.3F). Not only did this allow the laser to shine on the sample with minimal reflected power, but it also created an optical pathway to allow for fluorescence-based laser alignment from the top cap of the cryostat.

Tuning the probe to the Larmor frequency is achieved by using a 10 pF fixed capacitor on

the RF coil leads and two tunable 0.8–10 pF tunable capacitors mounted on a nearby puck (Figure 2.3D-E,G). In some probe designs constructed with thicker RF coil material (up to 1.1 mm in copper thickness), a second fixed capacitor was added in parallel to the original fixed capacitor. Since matching and tuning of the probe are dependent on temperature, it was necessary to have the capability of matching and tuning externally regardless of the internal temperature and vacuum of the cryostat. Ports on the cryostat cap were fitted with O-rings so that long (3.5 ft) matching and tuning rods could be turned from outside of the cryostat while maintaining vacuum. The rods were initially constructed from brass and turned by hand, as they protruded from the cryostat by >6 in. Later tuning rods were constructed from the cast resin FR8 and terminated in a female Allen key head for more precise rotation. At the tunable capacitors, the rods initially terminated on thin brass edges. This design failed due to the brass chipping when one tried to turn the tuning rod if the system was not correctly locked in place, if the tunable capacitor had reached an outer limit, or if water in the system had frozen one of the capacitors. Later designs for the tuning rods used ceramic screwdriver tips (Figure 2.3D); these are wider and do not fit in the groove of the tunable capacitor as easily but have yet to break off. A self-locking system to ensure engagement with the tunable capacitors was designed by having a spring push the tip of the rod into the center groove of the capacitor. This design was largely successful as it prevented the tip of the tuning rod from becoming displaced; however, if overly tightened, it could lead to premature degradation of the capacitor if excessive force was applied. Another strategy for engaging the tip of the tuning rods with the capacitors was to simply press down as the rod was turned.

The cryostat cap was machined in-house in order to accommodate custom Swagelok fittings with O-rings for the matching and tuning rods, MW and RF coax, and a central optical aperture (Figure 2.3C). This optical aperture was frequently closed with a brass optical block. When necessary for laser alignment, an endoscope camera with a wavelength filter from a broken pair of laser safety glasses covering the camera lens could be inserted into this optical aperture, the O-ring sealed, and the fluorescence of the diamond optimized.

The rest of the probe body was constructed of brass, featuring machined ribs or "pucks" which accommodated the tuning rods, structural rods, RF and MW coaxial cables, and the central aperture for laser beam passage (Figure 2.3A-B). The first probe model (which was indeed used for many experiments in this thesis) had two lightweight PDC pucks around the coil region. These were originally intended to lighten the probe, given that it would have to be mounted from the top of the magnet, approximately 6 ft in the air; however, future designs changed these pucks to be brass as well, for simplicity in machining and out of concern that they would not withstand temperatures down to 4 K. This original model probe was never tested below 77 K.

The RF and MW coaxial cables serve a dual purpose, both as coaxial lines and as structural support spanning the 39 in probe length. These rigid coaxial lines could be the only two support posts on the probe (if necessary due to the small inner diameter of the ColdEdge He cryostat) or could be a part of a support system of 2–4 additional supports. When functioning as the sole structural support, care had to be taken to not apply undue

torque on the bottom of the puck as the probe could quickly become misaligned, resulting in difficulty reaching the tunable capacitors with the tuning rods. The initial probe model used hollow grounded brass tubes, with the ability to run several shielded coaxial lines inside. Indeed, this was used at one point to run up to 4 simultaneous lines through the MW strut. It was quickly realized that if one of these coaxial lines was broken or picking up noise, it would be strongly detected during RF readout due to the MW coil being in such close proximity to the RF coil. Later probe designs favored using a single shielded coax with a brass exterior cut to the appropriate length of the strut for each of the MW and RF lines.

Finally, electrical shielding was maintained in one of several possible ways. The stainless steel body of the cryostat served as an RF shield; however, maintaining contact with the cryostat body was challenging. Laser-cut copper "fingers" (see Figure 2.3B), attached to the brass pucks by tension, glued by epoxy, or tied down by floss made good contact with the cryostat body; however, they scuffed against the inside of the cryostat when the probe was removed or inserted, frequently breaking off and falling to the bottom of the cryostat. If they obscured the optical window, no hyperpolarization could be performed until the cryostat was removed from the magnet and cleaned. A third method was to wrap a rigid copper mesh near the top of the body of the probe. As this effectively increased the width of the probe, it would make contact with the cryostat body for effective grounding. Still, this mesh would get stuck when the probe was removed from the cryostat and was inconvenient for rapid probe removals, especially when trying to maintain cryogenic temperatures. The most common strategy was simply to ensure that all coaxial cables leaving the probe were securely grounded and to assume that the cryostat cap was able to complete the connection to the cryostat body, even though it was intended to secure vacuum via an O-ring.

Outside of the probe, flexible, shielded RF and MW coaxial cables are connected to the NMR pre-amplifier and MW amplifiers throughout shuttling. They are supported by cable guides, mounted to the top frame of the instrument, ensuring stable operation through multiple shuttling cycles. These cable guides also provide support for the SMA connectors between the MW and RF coax lines of the probe and the flexible ones outside the probe, ensuring that the torque caused by the weight of the cables would not snap the SMA connections and break the MW lines. Thus, the cryostat, with all coaxial cables attached, can be shuttled without compromising integrity or picking up noise at the crucial steps of hyperpolarization or NMR readout.

2.3 Optical Illumination

The optical DNP strategy, outlined previously, is performed by shining a high-power 532 nm laser beam through an optical window in the base of the cryostat onto the sample located in the center of the MW and RF coils. In this design, the continuous-wave laser (Coherent 1169898) is located ∼6 ft away from the shielded 9.4 T magnet, and mounted at ankle-level (∼4 in from the floor). This ensures that the potentially magnetic components of the laser generator box are kept well away from the high magnetic field present under the magnet

body. The laser beam path is guided under the magnet by a set of piezo-driven mirrors, then directed up through the bore of the magnet and into the cryostat optical window via a 45-degree mirror mounted under the cryostat. This is the only optical component under the magnet bore, intended to minimize the need for magnetic components in this location.

Two lasers were used over the course of these experiments, with the second replacing the first after a gradual decrease in maximum lasing power due to age. The first laser had a maximum output power of 5 W but slowly decreased to a typical lasing power of 2 W for many experiments herein. The effect of this change in lasing power resulted in a loss of hyperpolarization and thus SNR. This laser was replaced with a tunable laser capable of delivering up to 8 W of output power; typical laser powers used in this experiment were $\sim$6 W.

Notable losses in laser power occurred due to the passage through the cryostat optical windows. While difficult to measure directly, it was estimated that up to 2 W of power could be lost due to passage through both the exterior and interior optical windows. This also includes beam divergence from passing through both fused-silica windows. In addition, care had to be taken when mounting the sample to prevent it from being partially or completely eclipsed by the MW coil on which it rested, as this would further decrease the laser power applied to the sample and limit hyperpolarization.

Since the laser is directed through the bore of the magnet and aligned via the top port (as described in Section 2.2), it is, in theory, possible to apply the laser to the sample at any given position in the bore. This removes the limitations of previous instruments (Ref. [11]) in which optical DNP was restricted to a single illumination field; instead, one could perform optical DNP at any given field accessible to this magnet, provided that MW irradiation at that frequency was able to be generated. It also allows the application of laser during NMR sequences for novel experiments that are detailed in a later chapter of this work.

The robustness of this instrumental design and the ability to perform hundreds of sequential experiments over the course of weeks proved challenging for the laser. While only used for 90 s of hyperpolarization at a time when performing most typical experiments, it lased continuously for many hours as experiments were run overnight. Effective laser cooling was an absolute requirement; thus, we stabilized the laser at 19 °C using a Lytron RC006G03BB2M007 chiller. With the addition of a new laser that could be remotely controlled, the instrumental control script was updated to turn the laser to standby mode when not needed for hyperpolarization.

2.4 Cryogen Delivery Compatible with Shuttling

The main design improvement over previous instrumentation developed in this lab, and indeed the main constraint necessitating the changes described above to the probe design and laser integration, is the addition of a cryostat to maintain cryogenic temperatures at the sample region. Since the cryostat must be shuttled with the probe in order to maintain the sample's constant temperature (justified in Section 2.2), the ability to deliver cryogens must

also be compatible with shuttling. Several adaptations and procedures were established to do so.

For the vast majority of experiments presented herein, temperatures only ranged to 77 K, courtesy of liquid nitrogen-based cooling. For this cryogen, a flow-through system could be used in which the nitrogen was released to the environment as a gas after use. The cryostat used was an Oxford SpectrostatNMR, a flow-through cryostat that consisted of an external vacuum chamber and an internal chamber in which the cryogen was delivered and the sample was held. Cryogen is transferred through a horizontal plunging spigot (Figure 2.1D), delivered into the sample well as a mist near the base of the cryostat, and then pulled through the return line by use of a vacuum pump after which it is dispersed into the lab environment. When cryogen is flowing, the sample well is thus at a slight vacuum, the extent of which was not measured, as it had minimal effect on the performed experiments. The outer vacuum chamber is maintained under vacuum by a dual pump system, comprising a Pfeiffer ONF 016 Vacuum Duo Line roughing pump in series with a Pfeiffer D35614 HiCUBE 80 Eco Vacuum TurboPump. This setup achieves an ultralow pressure of approximately 10^{-7}–10^{-8} mbar when optimized but would function sufficiently at pressures of only 10^{-5} mbar. It is important to note that the cryostat used in this work had been previously used in another laboratory and was repurposed for the present instrument. As a result, it exhibited a persistent, small leak. This leak was noticed because the pressure reading on the outside vacuum decreased as the vacuum was pulled to initiate cryogen flow. Over the course of several cooling and warming cycles, this leak would gradually worsen, resulting in difficulty maintaining optimal temperature. The cryostat vacuum chamber could be opened to facilitate the replacement of the inner optical window. Once sealed with indium wire and epoxy, this leak would be mitigated but would reappear after numerous cooling and heating cycles.

Concerns about another potential cryostat leak from the vacuum jacket to the outside lab arose when the cryostat's shuttling path and the bore of the magnet became misaligned. This caused a "cheese-grater" type effect, where the aluminum of the cryostat walls was shaved off against the inner walls of the magnet. These non-magnetic shavings fell out of the bore of the magnet, landing on the ground (and laser mirror) below, which obscured the laser path and decreased hyperpolarization. The cryostat was realigned, and a narrow stream of house nitrogen was directed over the mirror to clear any aluminum shavings. No exterior leak was discovered, although scrapes on the cryostat remain a testament to the difficulties of alignment over such a long shuttling path.

As the cryostat is shuttling, cryogen is flowing continuously from a ∼100 L liquid nitrogen dewar, placed outside the fringe field of the magnet (∼8 ft). Refilling this dewar could be performed on location using a secondary dewar. A custom (2.8 m) long transfer line is used, so that adequate slack can be maintained in the line throughout shuttling to not deviate the plunging spigot from horizontal. Pulling the spigot down from horizontal would likely result in the formation of a leak at the spigot as the O-ring in the plunging spigot is not seated correctly, or the tilting of the entire cryostat body would create misalignment and scrapes along the bore of the magnet. Indeed, even the weight of the transfer line manifested these issues over time, leading to the development of a cable to support the sidearm and transfer

line in addition to the pulley. This system was durable and robust, sustaining continuous shuttling approximately every two minutes for over two months of operation with minimal manual intervention.

Clogs in the transfer line were not unusual, as is the case with many cryogenic operations. These arose from the contamination of the line with water from the air, which would freeze and create ice blockages. These would disrupt cryogen flow, decreasing the cooling capacity to the cryostat and resulting in an increase of temperature measurable at the sample well. Frequently, these clogs could be cleared by simply agitating the transfer line—pulling it almost out of the dewar before dropping it forcefully back in, creating a change in pressure that would break apart the clog. If the clog was unable to be disrupted, or was in the return side (limiting the ability of the vacuum to pull warm cryogen from the sample well), the optimal course of action would be to shut down the experiments, warm up the system by blowing room-temperature nitrogen gas through the cryostat, and dry the transfer line overnight.

The temperature inside the cryostat was controlled by an Oxford Instruments ITC503 temperature controller paired with a variable output heater. In this scheme, a constant flow of cryogen vapor was delivered to the sample well to cool it, while the variable output heater delivered current to resistors near the sample well, heating them. The current was set by a PID feedback loop, native to the controller, and care was taken not to send so much current such that the resistive wires would be destroyed. These wires were located inside the vacuum jacket of the cryostat yet inside the radiation shield, making them difficult to access for repairs. A manual cap on the voltage that could be sent to these wires was programmed into the controller; if the cryogen was delivered at too high a flow rate, then the heater might rapidly compensate and overheat if this limit was not set. Indeed, a careful balance of the amount of cryogen delivered by the transfer line must be manually accounted for before setting the temperature controller; with the cryogen delivery increased or decreased in rough steps by changing the return vacuum pump settings and in finer steps by opening or closing the check valve on the transfer line. The controller could be operated in manual or automated mode, with the automated mode setting the desired temperature at which the sample well was to run, whereas the manual mode sets the voltage applied to the heating element, regardless of temperature. It was preferable to operate in automated mode when running experiments at or near the desired temperature and in manual mode when changing temperature by more than 5 °C.

2.5 Device Synchronization and Control

The control and synchronization of the instrumental components are of paramount importance to the automated operation of the instrument over extended, multi-day (and indeed, multi-month) experiments. For user convenience, the control of all elements is centralized to a “control computer”. Even the data processing, although it occurs on a separate computer, hosts a handshake connection with the control computer. Note that due to the large size

of the data that was processed, it was deemed necessary to separate the control computer from the data processing tasks. Without separation, the control computer (and hence instrument) would freeze and/or crash frequently due to the high demand on RAM during the data processing step.

In order to visualize the interconnected nature of the instrument, Figure 2.4 is color-coded according to the part of the system in which it is integrated. The primary synchronization (in yellow) is provided by a Swabian pulse streamer with 1 ns timing resolution. A previous iteration used a SpinCore PulseBlaster USB 100 MHz synchronization device; it was replaced due to the limited number of channels for control and insufficient timing capability to generate and operate a sequence lasting $\sim$10 min.

Temperature control is outlined in red. As described previously in Section 2.4, temperature is monitored by a Mercury ITC, which interfaces with the central control computer.

Control of the cryostat motion is labeled in orange. Here, the Swabian pulse streamer sends a trigger to initiate motion of the actuator. As the Swabian trigger voltage is not sufficiently high to create a recognizable input at the ACS controller, a MOSFET which gates a 24 V power supply receives the signal from the Swabian and sends the trigger to the ACS controller managing the actuator.

The laser system (in green) is equipped with a high-speed 1 ms Thorlabs SC10 shutter which synchronizes laser application with MW pulses for hyperpolarization and generally gates optical access to the sample. Motorized adjustable Zaber mirrors are used for optical alignment. They are connected to the control computer via USB and can be adjusted to alter the laser path, either during shuttling or before the experiment starts. This capability eliminates the need for the laser to maintain alignment at both low and high-field locations simultaneously.

Next, the MW pulse generation and delivery scheme is shown in blue. Chirped MW waveforms for hyperpolarization are generated by the Tabor Proteus AWT device. In order to synchronize timing with the rest of the experiment, the MW waveform is routed through a switch, which is triggered by the Swabian. Two amplification stages are used to achieve a final MW power of > 20 W, as measured by the power meter connected inline for monitoring. An isolator is also used inline to protect the amplifiers. As the MW signal is critical for hyperpolarization, this constant monitoring is necessary to anticipate any burgeoning problems, which could manifest as changes in power.

NMR pulse generation (the path shown in purple) was originally performed by the native VNMRS software using the Varian console (as shown in Figure 2.4). However, this system includes limits on the number of pulses that can be applied and the complexity of the repeated sequence. To perform longer spinlocks, constituting millions of pulses, or to interrogate more interesting sequences, a new method of generating pulses was developed by colleagues and adapted to this instrument [129]. This method uses the Tabor Proteus AWT to generate not only the MW chirps but also the pulses for the NMR pulse sequence. Here, the Herley amplifier from the Varian console is used for both schemes of creating the pulse sequence, as it introduces little noise, while amplifying the correct range of frequencies. The Proteus is also used in both schemes to sample and digitize the NMR signals at 1 GS/s, equivalent

to sampling every 1 ns. As it is equipped with a large (16 GB) onboard memory, it is capable of recording the precession signal over millions of pulses. In experiments involving the spinlock sequence, digitization is performed during windows between pulses. After the experimental conclusion, the data is streamed to the Data Processing Computer, so that it may undergo Fourier transform (FT) analysis to extract the amplitude and phase of the Larmor component in the window between each pulse. This transformation is necessary to reduce the data size for storage.

2.6 Avenues of Future Development

This instrument was designed with the ability for future iteration and improvements to be made, as necessary. Indeed, progress was made on several fronts in order to improve the capabilities of the instrument. Here, these are described from most to least progress on implementing any given improvement.

4K Compatibility

While ideal for use with liquid nitrogen cryogens, a flow-through cryostat system is incompatible with more expensive cryogens such as liquid helium. The flow-through cryostat releases used cryogen to the environment, using and releasing ∼100 L of cryogen per week. With the higher comparative cost of liquid helium, this would quickly become prohibitively expensive to operate; thus, a different method of cryogen delivery became imperative.

To operate colder than 77 K—reliably down to 10 K and in principle down to ∼4 K—a different approach is necessary. A closed-cycle liquid helium system (ColdEdge Stinger) recovers and recycles the cryogen, eliminating the need to periodically refill cryogen. The ColdEdge Stinger employs a Gifford-McMahon (GM) refrigeration cycle to cool a cryocooler down to 4 K. Room-temperature helium gas is then circulated over the cryocooler and through the closed-cycle cryostat, progressively cooling the gas and the sample to temperatures near 4 K (Figure 2.5A-B).

To ensure compatibility, as well as to achieve the higher vacuum integrity demanded by colder temperatures, we use a custom cryostat also designed and constructed by ColdEdge (shown in Figure 2.5C). It features three distinct chambers: the outermost vacuum-insulating chamber, a middle chamber for cold helium gas circulation, and the innermost chamber housing the sample. A valve to the innermost chamber is continuously purged with helium gas during cool down, enhancing heat exchange between the sample and cryogen while maintaining constant pressure. Each chamber is sealed with quartz windows to enable laser access for hyperpolarization experiments, the same as the original cryostat. The Stinger system utilizes a bayonet-style spigot which replaces the bayonet-style transfer line utilized previously. Due to the short length of the spigot, the Stinger system is mounted to an aluminum extrusion (80/20) frame ∼7 ft above the ground so that the transfer line can reach the cryostat throughout shuttling.

The GM refrigeration cycle is powered by pre-cooled, high-pressure helium gas supplied by the helium compressor (Sumitomo, F-70) located within a noise-dampening cart. This pre-cooled gas operates the cryocooler, which cools an auxiliary helium circuit from room temperature to the set cryogenic temperature in the cryostat. This auxiliary circuit uses the top compressor (Sumitomo, CKW-21) to push helium through the cryocooler and into the cryostat (Figure 2.5A). Vacuum must be pulled on the vacuum jacket of the cryocooler in addition to the vacuum jacket of the cryostat; this uses the dual vacuum pump system described previously.

The cryocooler can cool to ∼5 K in 75 min. Cooling the sample well to below 10 K requires approximately 3 hr, with further stabilization to 4.3 K taking around 18 hr when the sample well is empty. While sample well temperatures of ∼8 K have been achieved with the probe incorporated into the sample well, typically temperatures of ∼10 K are achieved for experiments that include shuttling.

The use of a second cryostat, with an additional chamber for closed-cycle helium gas circulation, realizes the need for development of additional, custom probes designed to accommodate an even narrower bore. The probe design remained largely the same as described in Section 2.2 with a smaller diameter puck. However, an unfortunate operational challenge is that the high-power RF pulses used at temperatures ∼10 K may lead to probe arcing at the tunable capacitors. While data collected at 10 K (see Figure 3.6 in Chapter 3) using PTFE capacitors (Voltronics AT10-4) demonstrate low arcing, these capacitors are not explicitly rated for cryogenic conditions. Alternate capacitor designs, such as those described by the Han group [185], have previously shown promising performance in cryogenic environments and could further enhance system reliability. Arcing is largely mitigated by using a helium gas environment in the sample chamber instead of pure vacuum, consistent with Paschen's Law [21].

Fiber Optic Laser Application

Laser alignment over the long path length of ∼10 ft is a challenging task, especially considering the final trajectory of the laser into the bore of the magnet must traverse ∼6 ft with no correction while striking a sample only 4 mm in diameter. Adding to the challenge is that the laser is placed near the floor level due to instrumental constraints, yet this poses a safety concern due to the ease at which an instrument user can alter a mirror's position.

A solution of using a fiber optic laser, where the laser head was introduced through the cryostat cap and placed directly on the sample was considered. This method would reduce the uncertainty of laser power loss through the optical windows in the cryostat and potentially eliminate the need for optical windows altogether in future cryostats, eliminating a known cryogen failure point. In addition, the infrastructure needed to shuttle the fiber optic cable was already available, as the same supports for the RF and MW cables protruding from the top of the cryostat could be used.

In practice, the fiber optic laser was successfully able to perform hyperpolarization without need for alignment. However, the power from this laser head was limited to only 1.5 W,

resulting in laser-limited hyperpolarization [168]. The fiber-optic cable, already in place, could also be terminated in a photodiode and used to discern alignment of the high-power laser applied through the optical windows. Two concerns arose regarding the use of the fiber optic cable. Firstly, under repeated temperature cycling, the cable appeared to contract, decreasing its length such that it was no longer in contact with the diamond sample. This created misalignment with the sample and reduced hyperpolarization. Secondly, the fiber optic cable is terminated in a metal head. When mounted to optimize hyperpolarization, it is suspected that this metal head resulted in a B_1 field inhomogeneity, decreasing coherence times in the sample. While there may be future applications in which the fiber optic laser and cable are most useful, the current instrument relies on optical illumination from the more conventional high-power laser underneath the magnet.

AC Field Application

Magnetometry, or the ability to detect small time-varying magnetic fields, is of great interest to a wide variety of areas including monitoring metabolic activities, optical and MRI imaging, high-temperature audio transceiving, and nanoliter NMR [135, 116, 174, 20] The methods for sensing in these publications include the use of SQUIDs, NV centers, and scanning Hall probe microscopy. A newly developed probe by Sahin et al. [165] is that of ^{13}C nuclei in diamonds, developed with a similar methodology on the companion instrument to the one described in this chapter [11]. While that instrument lacked a cryostat and thus was limited to room temperature samples, the unconstrained space in the magnet bore allowed for the placement of a loop coil through which a test AC field could be sent.

With the extension of lifetimes seen at low temperatures (the subject of Chapter 3), there is room for improvement in this sensing technique. Indeed, AC sensing improvements are described as an application in Chapter 7.

However, applying an AC field within the already tight geometry of the cryogen probe is challenging. There are several options to attempt this, with varying amounts of disruption. First, as there is already a loop coil integrated near the sample for hyperpolarization, it would be possible to switch that coil to apply MW chirps during hyperpolarization and an AC field during NMR readout. This was an effective proof of concept but unsuitable for automation as it required a user to manually switch the coaxial cable from the output of the MW circuitry to the output of the AC amplifiers during the $\sim$90 s of shuttling. The second option of applying an AC field was to add an additional, dedicated AC coil to the probe. In the original design, however, there was no opening in the cryostat top through which to pass a coaxial line. Initially, we attempted to run a second coaxial line through the hollow rod that housed the MW coax. This coaxial line was fashioned into a simple loop coil around the exterior of the RF saddle coil, but suffered from a poor termination and direct contact with the MW coax where the top of the hollow rod was cryogenically sealed. This led to shorting of the signal and a lack of hyperpolarization. We deemed this method unsuitable.

The final attempt to apply an AC field within the confines of the cryostat is to design a specific probe in which a dedicated AC coaxial opening is integrated into both the cryostat

cap and the entire body of the probe. Due to planned future operations with the "Stinger" 4 K system, this probe was designed for the narrow bore cryostat and has not yet been tested.

Goniometer for Sample Alignment

Throughout the course of these experiments, it became increasingly obvious that sample alignment is important for both hyperpolarization efficiency and the observation of certain effects caused by the NV center electrons in the sample. While the diamond sample used here was designed such that, when placed flat, its [100] face was oriented approximately parallel to B_0, this should result in overlapping frequencies of the four NV^- orientations, yielding a narrow MW region over which to hyperpolarize.

In practice, it is difficult to place the sample such that this orientation is maintained. Even slight deviations will separate out the NV^- families, splitting the single EPR peak into up to four peaks [107]. The strategy used for sample mounting in this instrument, described in Section 2.2, details how the sample is mounted in a flat-bottomed test tube with a notched quartz rod placed on top to keep the diamond centered. If this quartz rod was not pressed firmly enough, the sample would slide around the flat bottomed test tube, de-centering itself from the optical path. However, if the quartz rod was pressed too firmly, it would introduce a slightly uneven pressure on the diamond, tilting it slightly. This was, unavoidably with this sample mounting scheme, a frequent occurrence. It was difficult to fix this issue, as it was unnoticeable until a complete mapping of the EPR line was performed in an EPR-via-NMR experiment, similar to those performed by Pillai et al. [145]. Not only could this experiment take several hours to perform, it was also typically only run when at cryogenic temperatures. It was impractical to remove the probe while operating at cryogenic temperatures (as it could introduce water or other contaminants that could clog the cryogenic system), but in the current method of sample mounting, only the sample tilt can be adjusted manually. Warming the instrument up to room temperature to remove the probe took several hours and was also impractical for minor adjustments. Thus, a goniometer was needed to adjust sample tilt while maintaining cryogenic temperatures.

A prototype goniometer, capable of fitting around a similar coil design and geometry, was designed and 3D printed, as illustrated in Figure 2.6. With this system, inspired by the goniometer detailed in Ref. [47], two rods with attached worm screws each drive a gear. One gear rotates the center of the stage perpendicularly to the axis of the B_0 field. The second gear rotates a pendulum on which the stage sits, allowing access to a second dimension in which angular adjustment can be performed. The rods must extend out of the cryostat cap and be able to be turned similar to the matching and tuning rods. The worm screws must be coupled to large gears so that fine adjustments of only a few degrees are possible by hand.

This goniometer is limited to only fine adjustments since larger adjustments may cause the pendulum to obscure the laser for hyperpolarization or tilt the sample to no longer be centered in the RF coil. However, for the NV diamond sample which only requires fine adjustments of $< 5°$, this limitation is sufficient to demonstrate proof of concept.

Variable Field Hyperpolarization

While in theory this advance is immediately available, and indeed a featured advancement of this instrumental design, in practice, variable field hyperpolarization has never been implemented. The microwave frequency that is applied to drive polarization transfer to the nuclei is dependent on the electronic state of the NV diamond, which varies with magnetic field [94]. While any field between our current hyperpolarization field of 27 mT and the high field of the 9.4 T magnet is available for hyperpolarization, it is likely that one would need different microwave generators and amplifiers to perform hyperpolarization at higher fields. Shuttling is necessitated by the prohibitively high cost and low availability of the ∼266 GHz field necessary to hyperpolarize within the center of the 9.4 T magnet.

Faster Cryogenic Shuttling

Shuttling speed is limited predominantly by eddy current effects, as described in Section‘2.1. It is likely that the cryostat can be shuttled slightly quicker than currently described, as faster speeds have not been tested. For the samples examined in this body of work, the slow shuttling time described above was sufficient and there was no need to test faster speeds, as these may risk harm to the instrument. It is likely that dynamic variation of the shuttling speed (i.e. moving the cryostat faster through the low-field region, where eddy currents are low and fastest relaxation rates prevail before slowing the shuttling rate when the magnetic field increases) would safely result in a moderate improvement to shuttling speed.

While eliminating the need to shuttle the cryostat entirely is implausible (as described when discussing the co-location of the MW and RF coils, Section 2.2), the choice of cryostat material could reduce eddy current effects. Constructing the cryostat from non-metallic materials like glass or high-density plastics such as PEEK could allow for faster shuttling, realizing the possibility of studying new materials with shorter nuclear T_1 times.

ODMR Readout

NV centers in diamonds are well known for their optically addressable electronic states, which produce fluorescence. They are well-studied using optically detected magnetic resonance (ODMR) and highly characterized. Crucially, the instrument described herein has nearly every component necessary to perform in situ ODMR readout of the electronic state. The laser used for hyperpolarization in this system can perform the same function in ODMR, while the MW loop coil can drive the spin-sublevel transitions. Indeed, the only missing component is a detector for optical readout that could be placed either along the opening of the center of the probe or split from the laser beamline under the magnet. Integration of ODMR readout could assist in determining the microwave frequencies necessary for hyperpolarization excitation.

Cryogenic Preamplification

Signal-to-noise ratios in NMR readout could be significantly improved by integrating the first stage of the preamplifier directly within the cryostat. Similar strategies have been recently explored in the context of EPR [95] and adapting this approach could yield valuable benefits in future iterations of this system.

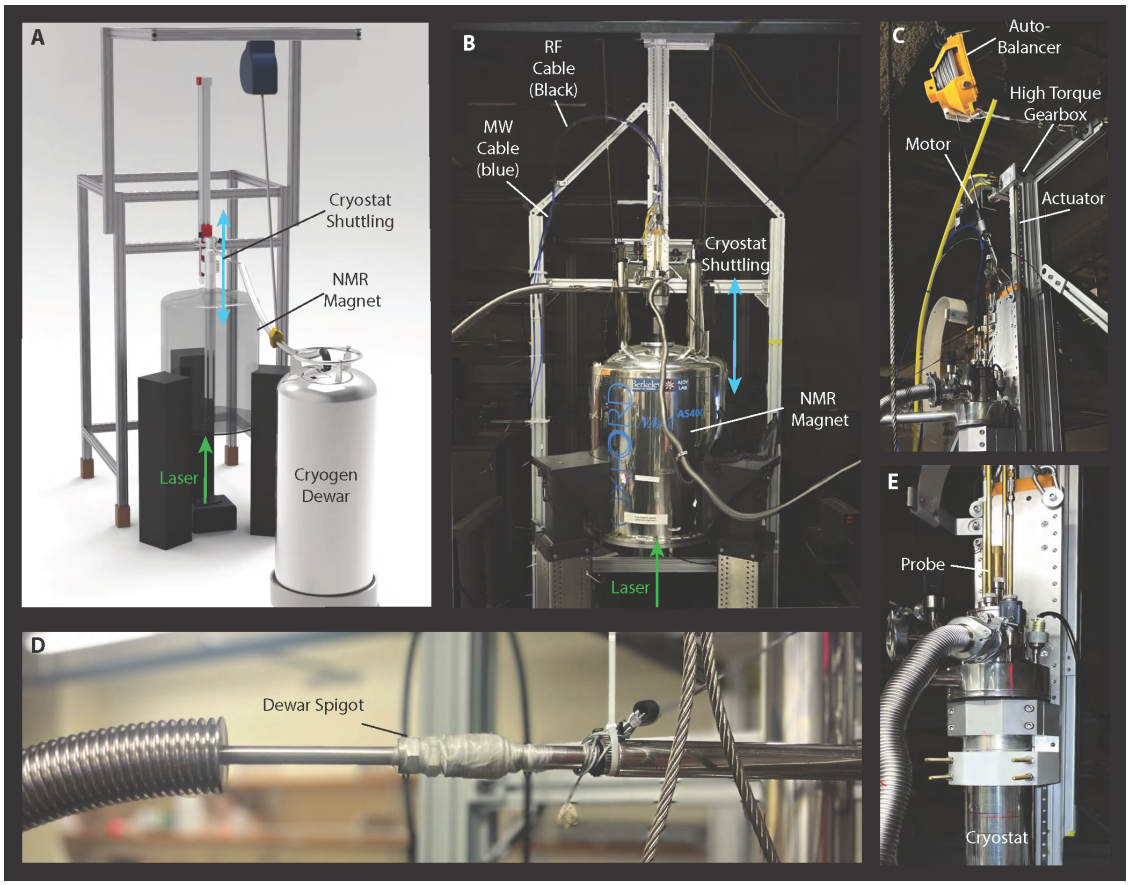


Figure 2.1 **Overview of the instrument.** (A) A CAD rendering illustrates the conceptualized core attributes of the instrument, comprising a 9.4 T high-field NMR magnet, a 4 K-compatible cryostat for sample and NMR probe housing, a replenishable cryogen delivery system, and optical access of a 532 nm laser for hyperpolarization. (B) Photograph of the instrument, mounted on an Oxford NMR magnet. (C) A close-up image shows the motor connected to a high-torque gearbox and the belt-driven actuator. A spring-loaded load balancer on the shuttler truck provides extra support to the cryostat against eddy currents during shuttling. (D) Cryogens are supplied from a non-magnetic dewar via a transfer line that moves with the cryostat, enabling continuous shuttling. Additional sealing with Parafilm is applied around a known connection that can leak. Temperature is regulated by a Mercury ITC (not pictured), and a dual-pump system evacuates the cryostat outer jacket for insulation. (E) The cryostat is mechanically mounted on the shuttling truck using custom clamps for vertical alignment with the magnet bore. A custom cryostat cap provides access to probe tuning rods.

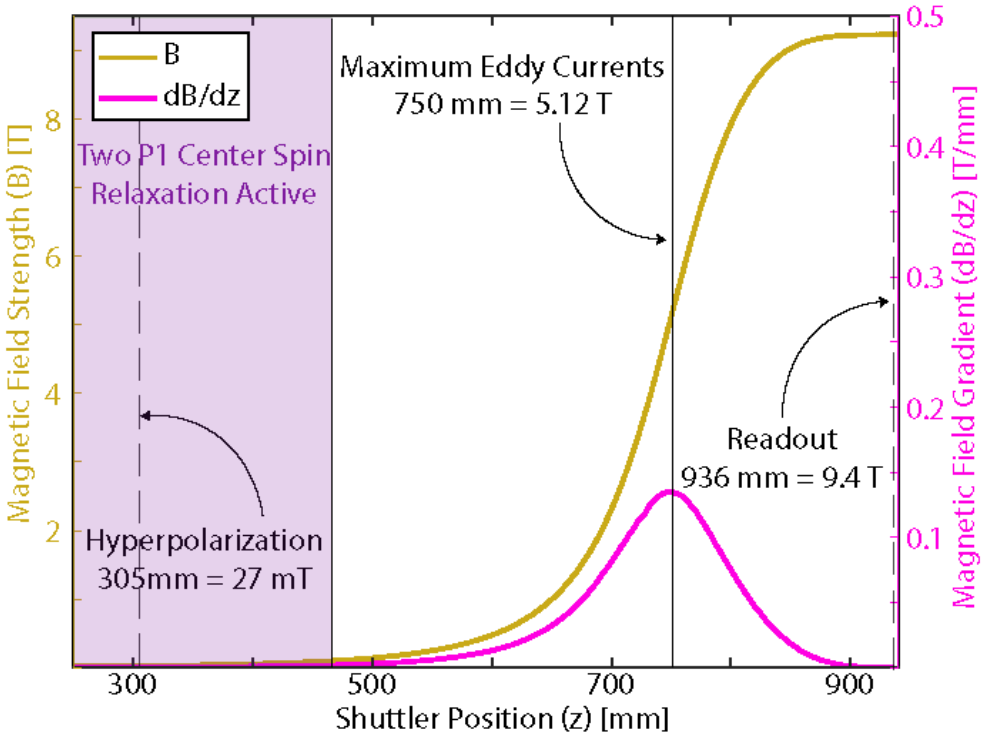


Figure 2.2 **Field map indicating variation in magnetic field.** with vertical position along the central axis of the magnet. The sweet spot of the magnet is evident at the high-field plateau (9.4 T). For the experiments on hyperpolarizing ^{13}C nuclei in diamond, the DNP (27 mT) and readout (9.4 T) fields are marked by dashed lines. The region where the P1-center-mediated two-electron spin-flip relaxation process is active is shaded in purple for clarity. Eddy currents are strongest at the maximum field gradient, located here at 750 mm (5.1 T).

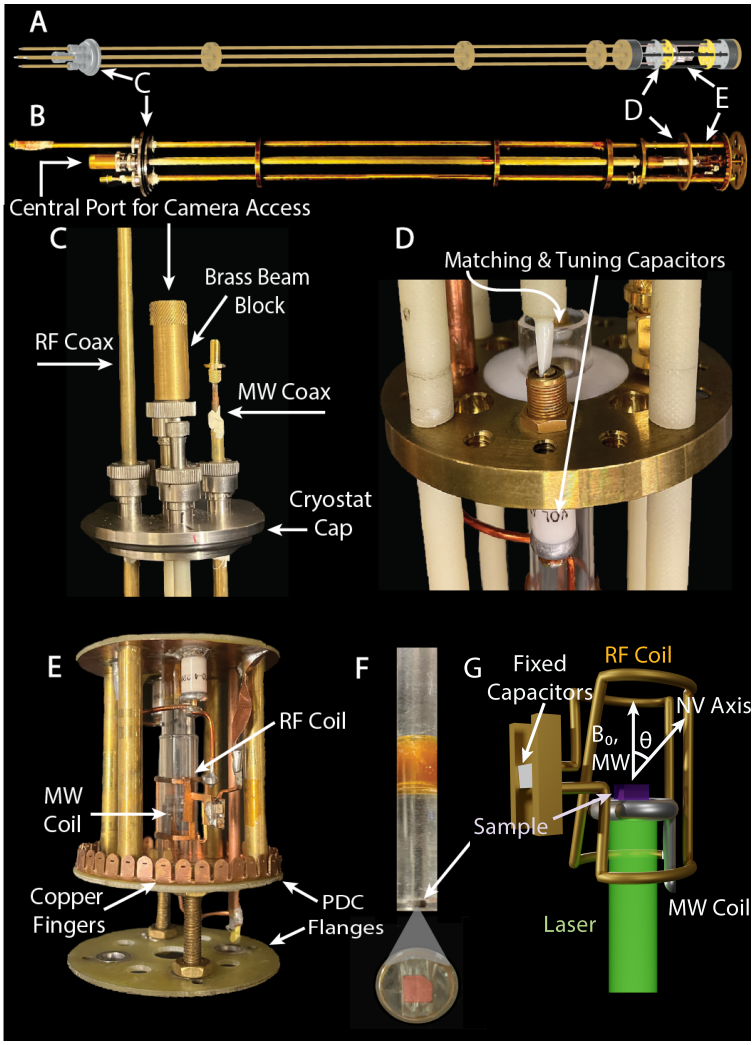


Figure 2.3 **DNP/NMR Probe.** (A) CAD rendering illustrates probe design and corresponding figure insets. (B) Photograph of the probe with length 39 in from the top of the cap to the bottom of the last support. Copper "fingers" maintain contact with the cryostat at each brass puck. (C) Probe top cap seals the cryostat. Custom Swagelok fittings enable NMR frequency tuning and impedance matching while maintaining vacuum and cryogenic conditions. The same fittings are used for MW and RF coaxial lines. A central port, closed with a brass insert when not in use, enables camera access for laser alignment. (D) Tuning setup consists of two tunable capacitors adjusted by ceramic screwdriver rod ends. (E) MW and RF coils. The MW loop is compactly centered within and perpendicularly oriented to the RF coil shown. (F) Sample mounting is achieved using a quartz rod insert notched for the sample size. (G) Schematic of sample orientation with respect to magnetic field and coil geometry.

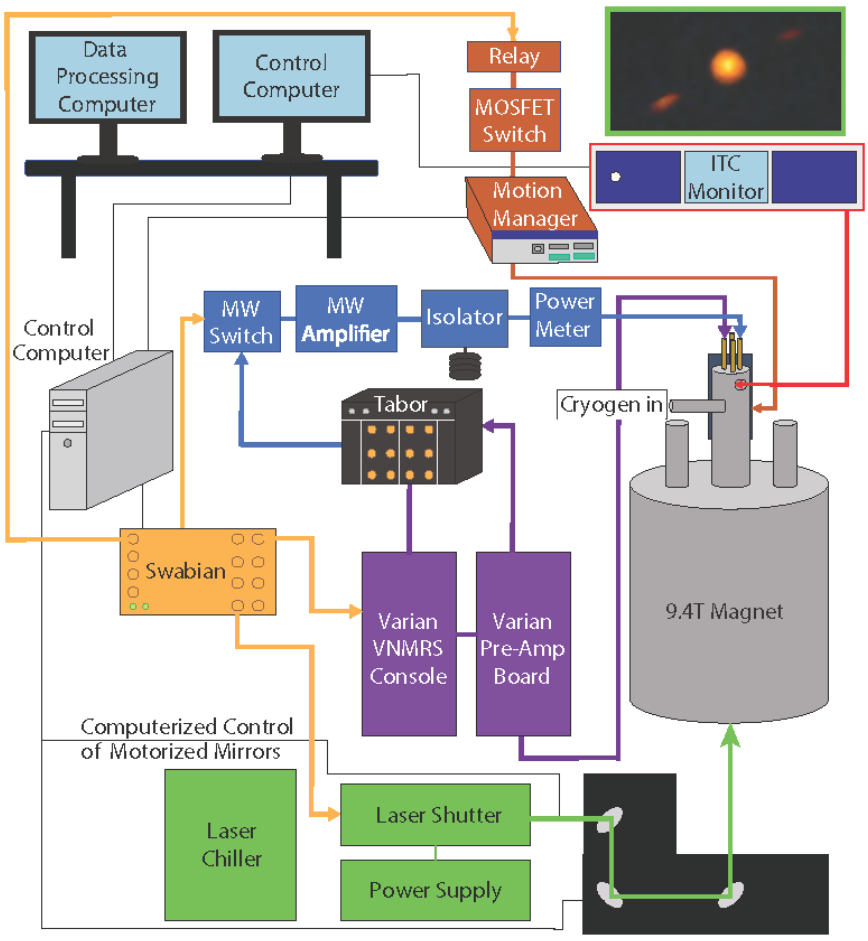


Figure 2.4 **Control and synchronization of the instrument.** (Yellow) Synchronization: TTL triggers generated by the Swabian pattern generator synchronize the timing of the four main components of the setup: laser, MW, shuttling, and RF. (Green) Optics: The laser beam is directed through the bore of the magnet onto the sample. The sample is aligned by observing the sample fluorescence on a camera (top right inset) and remotely adjusting the beam path through motorized Zaber mirrors to produce optimal sample fluorescence. (Blue) Microwave: MW generated by the Tabor Proteus AWT is applied to the sample when the Swabian triggers the MW switch on. An isolator protects the amplifier from reflected power. MW power is tracked with a power meter. (Orange) Shuttling: After optical hyperpolarization, the Swabian trigger is stepped up to 5 V via the relay. The 5 V trigger allows the MOSFET switch to connect the 24 V circuit and initiate the ACS for cryostat shuttling. (Purple) Radio-Frequency: RF pulses, synthesized and amplified in a Varian VNMRS console, are applied to the sample through the RF coil. The RF signal is preamplified using the Varian receiver but digitized on the Tabor AWT. (Red) Temperature control is maintained using a variable-output heater monitored with the Mercury ITC. Temperature information is accessed from the control computer.

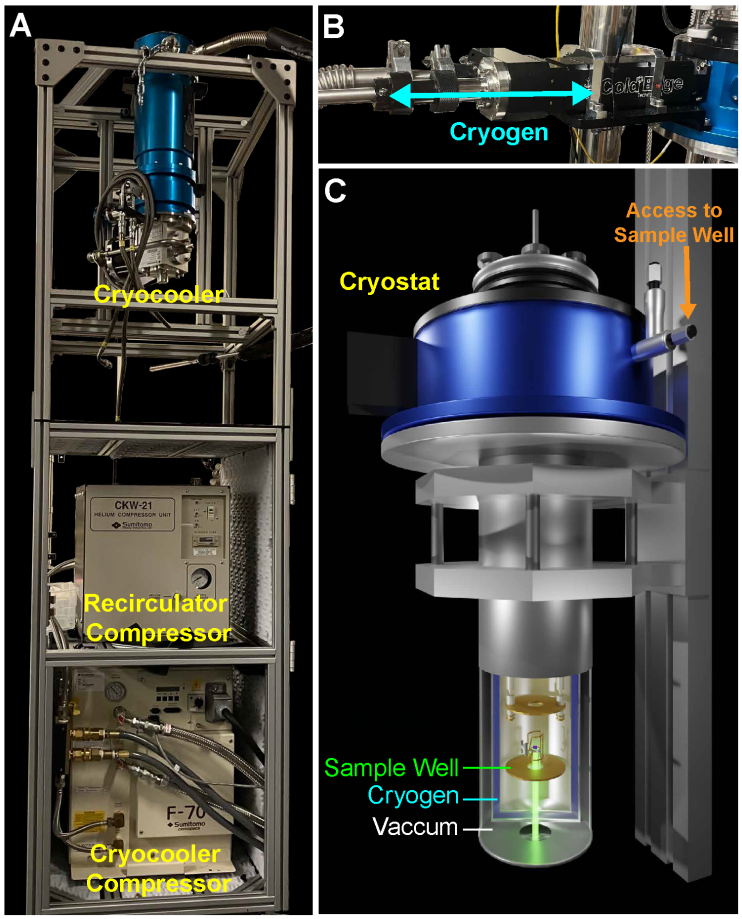


Figure 2.5 **Closed-cycle liquid helium system.** allowing operation to ∼10 K. (A) Mounted system displaying the compressors and cryocooler. The ColdEdge Stinger cryocooler (blue, top) is cooled using the Sumitomo helium cryocooler compressor (bottom). The recirculator helium compressor (middle) moves helium gas through the cryocooler and into the cryostat. (B) The transfer line with bayonet insertion delivers helium gas to the cryostat and returns warm cryogen to the cryocooler for recycling. (C) CAD rendering of the cryostat with mounted probe. The length of the cryostat is not to scale. The closed-cycle cryostat has three separate chambers: the outermost chamber is a vacuum jacket, the central chamber is where the cryogen flows, and the innermost chamber is where the probe and sample are located. This interior chamber can be directly accessed and purged with helium gas to facilitate cooling. Each chamber is sealed with a quartz window, permitting laser access for hyperpolarization.

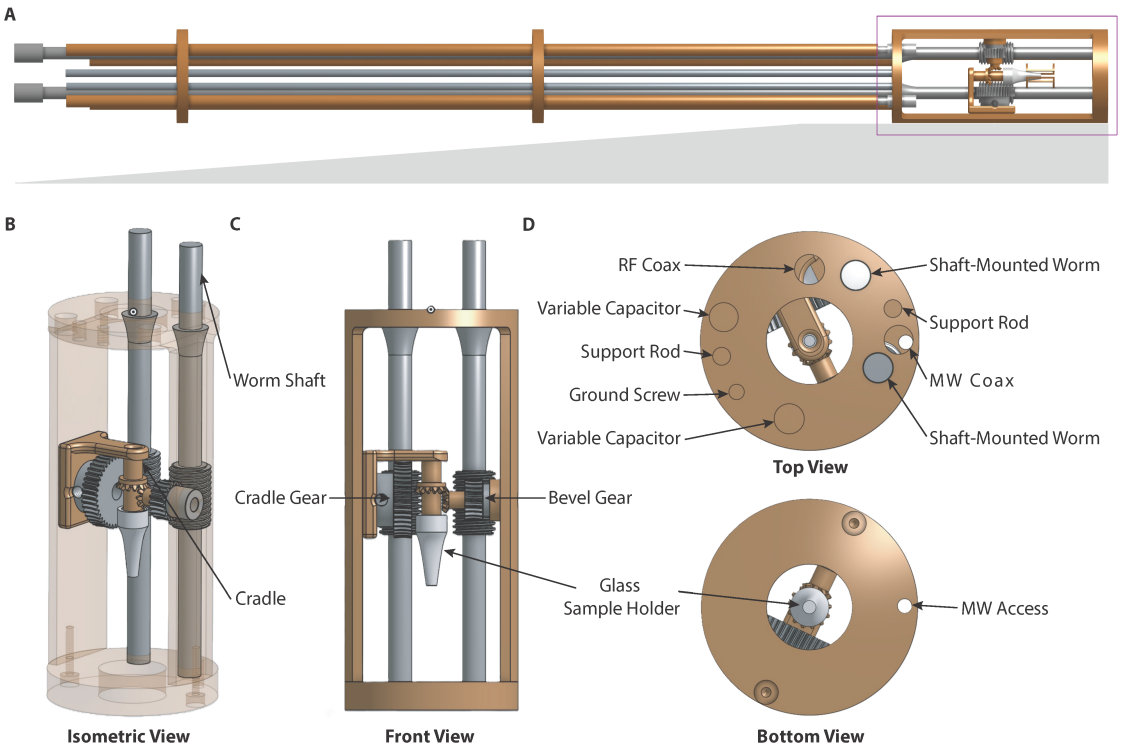


Figure 2.6 **CAD image of goniometer prototype.** (A) The focus of this updated probe is on the changes made at the base, where the goniometer structure is located. (B) An isometric view shows the interplay of the worm shafts and cog wheels. (C) The two worm gears are located on either side of the probe, retaining space for necessary RF and MW electronics. The large gear ratio (∼40:1) of the cradle gear allows fine control of the tilt angle. (D) The top and bottom views of the goniometer region reveal the complex geometric puck design required by the addition of the worm drives for the goniometer. All necessary components of the probe are retained, including the MW and RF coaxial cables and ground, as well as a narrow optical channel through the cradle for laser alignment.

Part III

Spin Temperature Control

Chapter 3

Cryogenic Cooling of Sample Temperature

The first method to control nuclear spin lifetimes, and indeed, the method primarily enabled by the construction of the cryogenic field-cycling instrument detailed in the previous chapter (Chapter 2) is to decrease the sample temperature as far as is cryogenically possible. Decreased temperature is well established to increase the polarization (see Eq.1.2) of our spin system [189]. Aside from the obvious boon of increased signal-to-noise ratio, a highly polarized state has significantly decreased flip-flop interactions that act to diffuse polarization. Considering our system of ^{13}C nuclei, however, the temperatures must be ultra-low to reach this level of polarization: sub-1 K to reach polarizations of $\sim 1\%$ (see Figure 3.1).

Our electron system, however, is a different story. When using NV diamonds, we have several known electron species that are highly important. First are the NV centers, which are ubiquitous at the center of our ^{13}C systems as the generators of hyperpolarization. We also have P1 centers, which are electrons stemming from nitrogen substitutional defects [54]. Previous work has suggested that the most active spin-relaxation channel (with respect to T_1 at least) is the multiple spin-flips in the P1 bath that couple to the ^{13}C spins [9]. As the P1 centers are randomly located within the lattice and we measure the system as an average over all NV center environments, we treat the P1 centers as a background effect acting uniformly across the measured ^{13}C spins [24].

Cooling of the entire sample should thus have an effect on nuclear spin lifetimes as a byproduct of its effect on electron spin polarization. When considering Figure 3.1, the polarization of the electron at 100 K (marked by the rightmost dashed line) is $\sim 6\%$, while the polarization of the electron at 10 K (leftmost dashed line) is almost $\sim 60\%$. These high levels of polarization effectively suppress the flip-flop interactions within the P1 center bath, thus suppressing the relaxation in the ^{13}C nuclear spins that stem from it.

3.1 Temperatures from RT - 77 K

The instrument described in Chapter 2 is initially configured to operate with liquid nitrogen as the cryogen. This limits the sample cooling to a minimum of 77 K, with long-term operation at slightly higher temperatures of $\sim$ 100 K. We note that this increase in operational temperature to $\sim$ 100 K is due to balancing the load on the heating element in the cryostat with the continuous flow of nitrogen vapor: flowing too much nitrogen vapor may lead to an accumulation of liquid nitrogen in the cryostat, obscuring the optical window for hyperpolarization. The most stable operation of the cooling system occurs when a small amount of vapor is flowed through the cryostat while the heating element operates at a constant low voltage; these conditions are achievable when the temperature is set between 85–100 K.

Let us first examine the type of data that is now achievable at cryogenic temperatures with the field-cycling instrument. Figure 3.2A displays the FID of hyperpolarized ^{13}C spins at 100 K. It is characterized by rapid decay primarily governed by internuclear dipolar interactions, with a $T_2^* = 1.1$ ms. The typical FID pulse sequence is incorporated into the hyperpolarization scheme in the inset. In comparison, Figure 3.2B employs the pulsed spinlock sequence as we describe in Chapter 1, with the experimental sequence shown in the inset (i). Here the pulses are 25 μs in length with 75 μs pulse-to-pulse spacing. Inductive acquisition of nuclear precession is carried out between pulses, during which the Herley amplifier is blanked. The data points represent the Fourier intensity at the heterodyned Larmor frequency after every pulse (see inset (ii)); the rapid collection for long-lived experiments means curves such as these comprise over 10 M points. There is also a significant increase in lifetime, with $T_2' = 93.5$ s. We note that this lifetime is comparable to that presented in Ref. [25], without the optimization of the pulse sequence that was necessary to achieve such a long lifetime at room temperature.

Indeed, when comparing room temperature data with data taken at $\sim$ 85 K on the same field-cycling instrument, we see this predicted lifetime extension. Figure 3.3 shows two spinlock decay profiles at RT and $\sim$ 85 K, where Figure 3.3A demonstrates that the $\sim$ 85 K data is higher in total signal while Figure 3.3B shows the normalized and smoothed data to compare lifetimes. We note in Figure 3.3B that a 1000-point moving average filter was used to smooth the data, resulting in an artificially high baseline. Based on analysis of the raw dataset in Figure 3.3A, it is evident that the signal at RT has decayed below the SNR threshold by $\sim$ 150 s, resulting in the flatness observed in Figure 3.3B. In comparison, however, the signal taken at 85 K continues to decay and has not reached the noise floor even past 300 s.

Due to instrumental constraints during cooling (see Section 3.3), only a range < 150 K can be accurately studied. Figure 3.4 shows the normalized signal profile during cooling from 130 K to 80 K in steps of 5 K. We note that taking the data even in this small range of 50 K is a logistical challenge: the matching and tuning of the RF circuit drifts with temperature. Even small changes can result in off-resonant pulses and decreased RF power [27]. As we will examine later in Chapter 7, off-resonance effects can change the appearance and behavior of spinlock decay profiles immensely.

For this reason, data in Figure 3.4 was taken carefully so as not to induce these off-resonant effects. The matching and tuning were checked after every temperature decrease to ensure that they remained in the optimal range. We still consider this data to be preliminary, however, as further optimizations (both of transmitter offset and Rabi frequency calibration) were not considered at the time of measurement.

Data taken at higher temperatures ($\sim 110 < T < 130$ K) demonstrates very little change in lifetime or decay profile as a function of temperature. As temperature continues to decrease, the decay profiles extend slightly in lifetime from $T_2' \approx 130$ s to $T_2' > 160$ s. The coldest decay profile at $T = 80$ K notably has much poorer SNR and exhibits a wavy, unsteady profile. Both of these are believed to be a result of nitrogen vapor condensation at the base of the probe. Condensation of liquid nitrogen on the optical window diffracts the laser and decreases the amount of power for hyperpolarization; this results in a dramatic loss of SNR. The waviness in the spinlock decay profiles is attributed to the nitrogen condensation on and around the RF circuit changing the tuning as a function of droplet formation; this is a more acute effect than the temperature drift described previously.

Comparison to T_1 and T_2 measurements

An advantage of performing spinlock measurements to characterize the decay of these spins via T_2' is the ability to sample the T_2' profiles at an exceptionally high density of points, capturing one data point per pulse. This granularity, capturing > 4 M data points per curve, allows for a deeper understanding of the decay profile, extending beyond just the $1/e$ intercepts (dashed lines in Figure 3.2, Figure 3.4). The results clearly show an increase in T_2' values as the temperature decreases.

The cryogenic field-cycling instrument does allow measurement of T_1 relaxation times of hyperpolarized nuclei as a comparison to the investigations into the T_2'. We note that the instrument is capable of performing these experiments across the wide range of magnetic fields accessible to this instrument (from 27 mT to 9.4 T). Hyperpolarized spins are allowed to relax at a target field, B_{int}, for a set period before spinlock readout at high field (Figure 3.5(i)). Figure 3.5 shows the variation of nuclear T_1 at low (27 mT) and high magnetic fields (9.4 T) at 100 K. Corresponding lifetimes are recorded as T_1=386 s at low field and T_1=3094 s at high field. At room temperature (using a similar field-cycling instrument), the lifetimes at low (36 mT) and high (7 T) were recorded at T_1 =283 s and T_1 =1520 s, respectively [24]. While undoubtedly there is a contribution from the different fields at which the lifetime is measured, we note that at 100 K the low-field lifetime is ~ 100 s longer than that of the slightly longer low-field lifetime at RT. This demonstrates the strongly temperature-dependent effects of T_1 in our nuclear spin system.

Each data point in Figure 3.5 is a single-shot measurement, resulting in a total experimental time to measure these curves of ~ 5 days. When investigating temperature-dependent behavior, it is much more efficient to study T_2', which can be collected in single shot with high density of data points as opposed to T_1 decay curves, which require a hyperpolarization experiment lasting up to 3 hours per data point on the decay curve. Indeed, the high number

of data points in the T_2' decay curves facilitates in-depth analytical approaches to study their shape, such as the use of Laplace inversion to examine the constituent decay components and their temperature dependence (Chapter 7) [178].

We note that the spinlock sequence shares a marked similarity to the CPMG sequence [125]. If, say, the spinlock sequence used π pulses in the spinlocking train, the spinlock sequence would approximate a CPMG with poorly calibrated τ and echo collection. While it is important to compare this system using conventionally established T_2 values, the NV center structure thwarts these efforts and leads to the interesting zero-crossing behavior described in Chapter 6 in lieu of an in-depth comparison between T_2' and T_2.

3.2 Preliminary Studies at ∼10 K

The most promising extension of lifetime will be at very low temperatures achieved through the use of liquid helium cryogen, as per the hypothesized method of quenching electron-mediated (NV and P1) noise experienced by nuclear spins. This quenching likely results from an increase in the T_{1e} relaxation times of the electron spins at lower temperatures [94], and greater electronic polarization at high fields and low temperatures [186]. Data from both these references support that the most dramatic extension of T_{1e} occurs between 20–100 K, depending on NV diamond sample conditions.

Preliminary data, collected after alterations to the instrument in Chapter 2 to include the "Stinger" system, demonstrates this predicted increased lifetime. Figure 3.6 compares spinlock curves across three temperatures similar to those of Figure 3.3. The lifetime extension between similar conditions at RT ($\sim$ 300 K) and 10 K is almost a full order of magnitude; from $\sim$ 20 s to $\sim$ 200 s. However, the dataset at 10 K has notably lower SNR than that of other datasets, even that of RT, with comparable smoothing (also via a moving average filter). The low total signal of this dataset gestures to an inability to build up hyperpolarization effectively; when collecting this dataset, total signal appeared to decrease when cooling past temperatures of $\sim$ 60K. The difficulty collecting this dataset reflects some instrumental limitations which were not discovered when the instrument was first conceptualized.

3.3 Instrumental Limitations

We note several instrumental constraints that largely limit our studies to the temperatures described above. Firstly, it is difficult to achieve and stabilize temperatures between RT and $\sim$ 150 K. While these temperatures are not unachievable, it is impractical to stabilize high temperatures for a long period of time as the liquid nitrogen flow must be minimized and the heater must be operating at high voltage: these conditions can introduce rapid temperature fluctuations if the nitrogen vapor flow is unstable. Indeed, induced current in the heater circuit from motion through the magnetic field could alter the temperature at the sample by tens of degrees with every experiment when operating in this metastable high-temperature

regime. This constraint leads to the first caveat: we compare RT and cryogenic datasets (Figure 3.3) and we compare datasets at different temperatures near 100 K (Figure 3.4), but no comprehensive study of the decay profiles as a function of temperature starting from RT has yet been achieved. That being said, should the effect of temperature be largely dependent on the electron bath, as hypothesized, the most significant effects on relaxation as a function of temperature should be achieved within the range of instrumentally-accessible temperatures (sub $\sim$ 100 K) [94, 186]. However, measuring at temperatures that are too low likewise introduces complications should liquid nitrogen condense in the probe, as in Figure 3.4.

Experiments using helium cryogen are likewise delicate. The use of a vacuum inside the sample well results in poor cooling of the sample and an inability to dissipate heat generated from the optical hyperpolarization. The use of helium gas inside the sample well, however, is known to exacerbate arcing, which is already a known issue for these spinlock experiments where millions of pulses are applied. In addition, the probe capacitors that are not rated for such cold temperatures further worsen the arcing. Finally, the aforementioned loss of signal at temperatures colder than $\sim$ 60K has thus far limited the usable data that can be collected using helium cryogen.

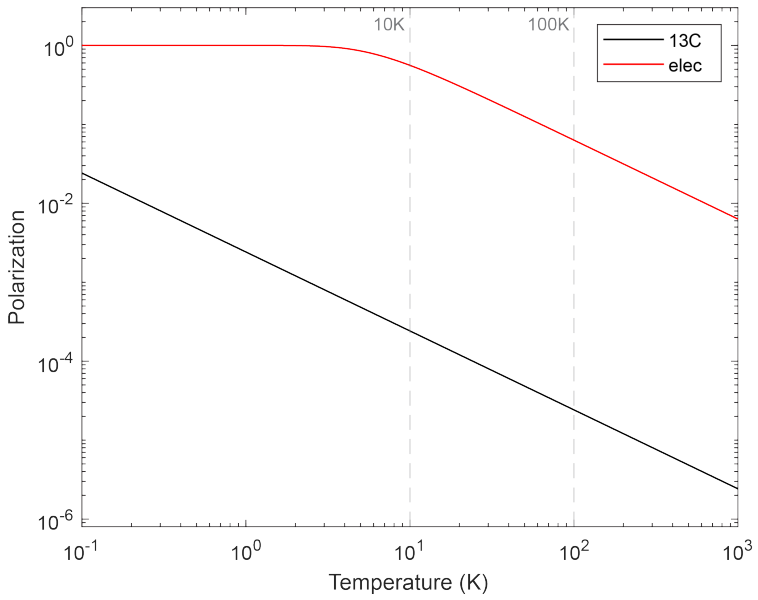


Figure 3.1 **Calculated spin polarization as a function of temperature.** Boltzmann thermal spin polarization, calculated from Eq. 1.2 for ^{13}C nuclei and electrons. Vertical dashed lines at 10 K and 100 K indicate reference temperatures for which the cryogenic field-cycling instrument operates under helium or nitrogen cryogen conditions, respectively.

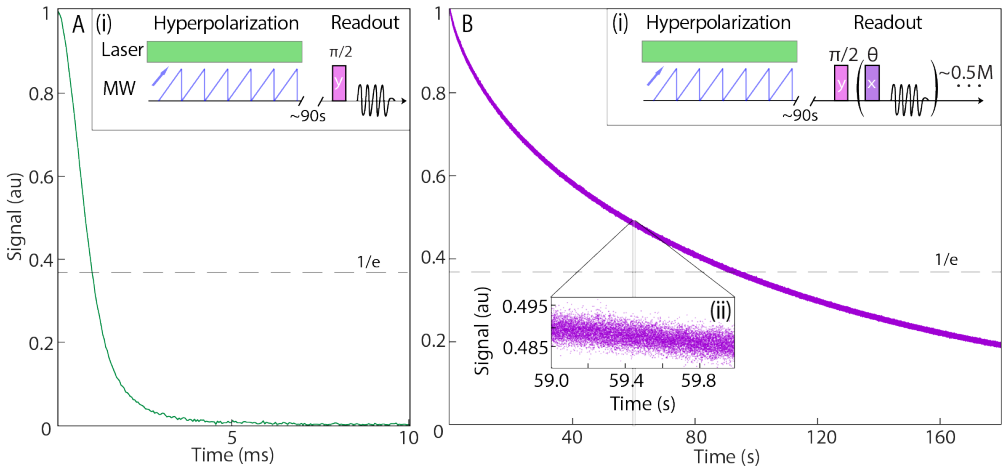


Figure 3.2 **Probing hyperpolarized ^{13}C nuclei at 100 K.** (A) FID and (B) pulsed spinlock traces for ^{13}C nuclei hyperpolarized via optical DNP at 100 K. (A(i)) Experimental scheme for DNP followed by an FID readout. (B(i)) Pulsed spinlock readout involves a pulse train of $\theta = \pi/2$ pulses with a 50 μs interpulse separation. (B) Pulsed spinlock data shows a >10,000-fold extension in lifetime, with >3 M points in the trace. Inset shows a 1 s window at $t = 59$ s and highlights the rapid data sampling rate.

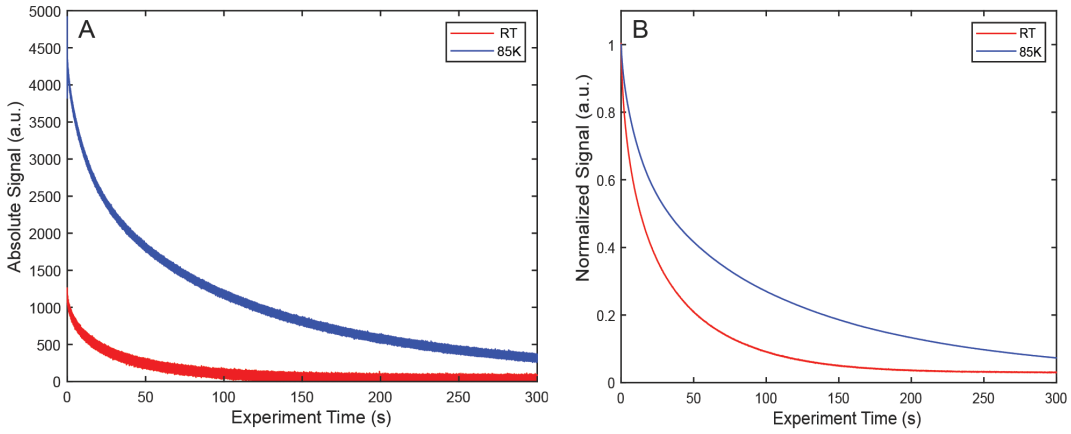


Figure 3.3 **Comparison of spin-lock decay from RT to 85 K.** Signal S vs time decays of spinlock data taken at RT (red) and 85 K (blue). (A) Unsmoothed data clearly demonstrates the increased signal present at 85 K compared to RT. Here the RT signal decreases to the noise floor within $\sim$ 150 s. (B) Normalized and smoothed data (via a moving average filter) shows the difference in decay profile between RT and 85 K datasets, with demonstrated lengthening in the relaxation time at 85 K.

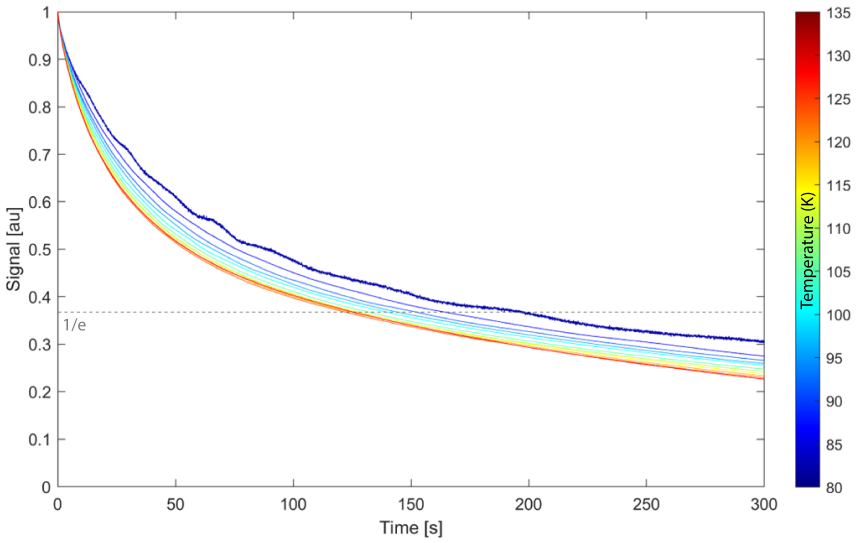


Figure 3.4 **Comparison of spinlock decays at cryogenic temperatures.** Normalized and smoothed signal S vs time decays for cryogenic temperatures from 130 K to 80 K in steps of 5 K (see color bar). While only a moderate shift in decay profile is observed, the shift is greater at colder temperatures. High noise and artifacts in the 80 K data (dark blue) are a result of condensing nitrogen vapor.

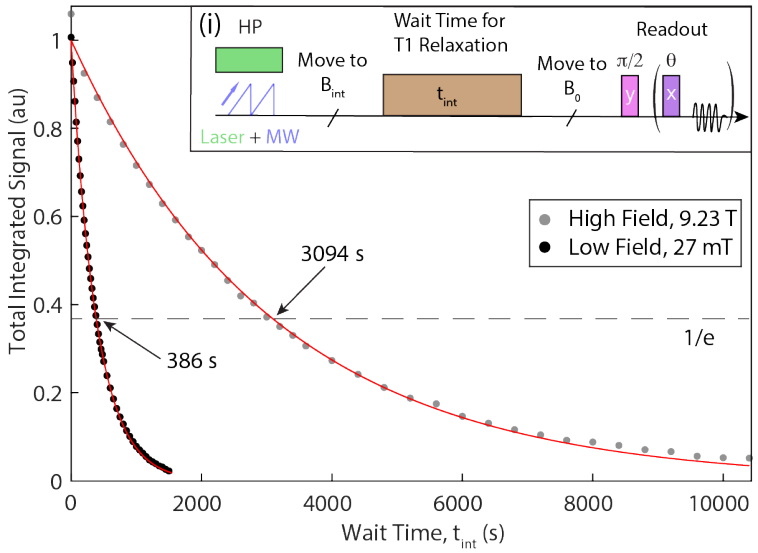


Figure 3.5 **Field-cycling relaxometry with hyperpolarized nuclei.** (i) Experiment schematic where spins are allowed to relax at an intermediate field B_{int} for a period t_{int}, followed by high-field (9.4 T) readout via spinlock. (Main Figure) T_1 relaxation traces at 100 K measured at low-field (27 mT) and high-field (9.4 T). Each point represents an integrated single-shot measurement, taken with 60 s spinlock readout.

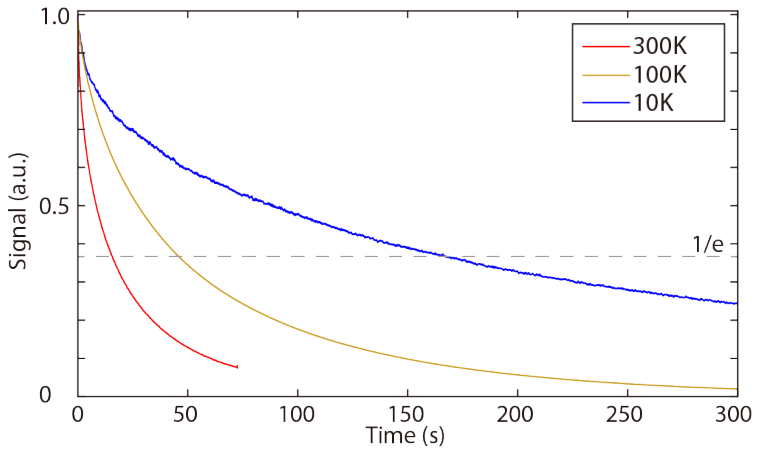


Figure 3.6 **Spinlock measurements down to $\sim$ 10 K.** Three spinlock measurements taken at RT, 100 K, and 10 K. Data at 100 K and 10 K is taken over a 5-minute period involving > 4 M pulses. Data at RT is taken over 70 s, sufficient to determine a $1/e$ intercept (dashed line). All data is smoothed using a moving boxcar average. Data reveals a significant lengthening of T_2' times with decreasing temperature.

Chapter 4

Hyperpolarization-based Cooling of Spin Temperature

4.1 Overview

While varying the sample temperature is the most direct means of altering the effective spin temperature of a system, hyperpolarization provides another avenue for manipulating spin polarization and, consequently, nuclear spin lifetimes. Hyperpolarization, in a sense, is an effective nuclear spin temperature [61] that differs from the lattice temperature. Using Eq. 1.2, we can calculate the temperature of the nuclear spins from the polarization level that we have generated, often resulting in effectively sub-Kelvin nuclear spin temperatures with a simple 100-fold increase in polarization.

The hyperpolarization we generate is not uniform across the sample; this is an important aspect of the discussion in Chapter 6. Indeed, this lack of uniformity, with high levels of polarization generated near the fast-relaxing electron of the NV center, has been recently studied [24] to aid in applications such as quantum control [83].

Work performed in Ref. [24] found that additional hyperpolarization increased T_2' lifetimes of nuclear spins largely due to the increased diffusion of hyperpolarization away from the NV center relaxation source. This work was performed at room temperature, using the aforementioned room-temperature field-cycling instrument [11]; this chapter provides a follow-up to this work using the cryogenic field-cycling instrument in an attempt to (a) confirm the previous observations and (b) note any differences that arise due to cryogenic temperatures.

The spinlock sequence offers an effective method for evaluating the impact of hyperpolarization. For instance, Figure 4.1A-B compare spinlock signal traces with (purple) and without (orange) hyperpolarization at 100 K. For thermal measurements, spins thermalize in the magnet for > 10 hr prior to the experiment. The SNR increase due to hyperpolarization is apparent, both from the total signal traces in Figure 4.1A and the noise in the normalized traces in Figure 4.1B (of which the thermal signal is subject to a moving average smoothing

function of 1000 points per bin, for visualization purposes). We quantify the SNR increase by performing an FT on each trace, analyzing the effective line-narrowed NMR spectrum. The results, shown in Figure 4.1C on a logarithmic scale, highlight a $>$ 100-fold gain in SNR from hyperpolarization.

We turn our attention next to the lineshape and T_2' in Figure 4.1B. Here, the thermal signal dies rapidly with a T_2' of $\sim$ 10 s before exhibiting a markedly slower decay. The region of slow decay notably occurs as the signal approaches the noise floor. Indeed, such poor signal complicates comparative analysis between hyperpolarized and thermal signals as the thermal signal, requiring a long time for build-up of polarization, is not optimized with respect to pulse parameters.

Instead, we compare the relatively narrow linewidths of these signals shown in Figure 4.1C. The thermal signal here exhibits a slightly narrower linewidth than that of the hyperpolarized signal; this is explained by considering the fact that hyperpolarization stems from the NV center, which also acts as part of that electron reservoir to relax the spins. Thus, the nuclei that are observed in the hyperpolarized signal are biased to be nuclei that relax faster due to NV-mediated dissipation causing shortened lifetimes as compared to the nuclei in the thermal case.

4.2 DNP at low temperature

A major difference in the effect of hyperpolarization between previous room-temperature studies [24] and this dissertation is the fact that hyperpolarization of ^{13}C in this system at 100 K is more effective. The hyperpolarization methodology was described in Chapter 1 and the specific instrument capabilities that enable it were described in Chapter 2. It has previously been well described in Refs. [10, 13, 145], where MW pulses are chirped across the NV EPR line to drive polarization transfer. A useful way to calibrate the in situ underlying EPR spectrum of the sample, which is highly dependent on sample orientation with respect to the magnetic field as well as temperature [7, 38, 12], is to map the EPR spectrum via DNP (Figure 4.2). Here, chirped MWs are applied in small windows, each spanning $\Delta f = 25$ MHz, with their center frequencies sequentially swept across a broader range.

Figure 4.2 shows the experimental data comparing the DNP-EPR spectra obtained at RT and 100 K under 60 s of optical pumping. We observe the expected temperature-dependent shift of the NV zero-field splitting [7, 38] towards slightly higher frequencies. More obviously, there is an order of magnitude increase in the DNP signal at 100 K. We attribute this increase to the longer electron T_{1e} relaxation times at lower temperatures [94].

As explored in Ref. [168], the extent of hyperpolarization depends on several parameters, including the rate of electron polarization from laser pumping, the rate of polarization transfer to nearby nuclei from the aforementioned MW chirps, and finally the rate of bulk polarization from spin diffusion. The increase in electron T_1 relaxation times at low temperatures, then, primarily increases the efficiency of polarization transfer to nearby nuclei because the longer electron T_1 means that less of the polarized electronic reservoir will be

lost before the polarization transfer is complete. This has a large effect on the ability to build polarization within the ^{13}C nuclei.

The temperature change likely does not affect the other rates of hyperpolarization generation, since a strong temperature dependence in the intersystem crossing (ISC) necessary to polarize the electrons is not observed above $T \approx 22$ K [73]. Spin diffusion, which mediates the last rate step, is generally considered to be independent of temperature. The nuclear spin flip-flops that act to diffuse spin polarization are mediated through dipole couplings and occur when energy is conserved; thus there is no effect that stems directly from temperature in the range presented throughout this dissertation. Dissipation from the NV electron (which is decreased as T_{1e} increases) does not actively relax proximal nuclear spins until readout occurs (see Chapter 6.1) and thus has no temperature-dependent effect on the ability of spin polarization to diffuse.

Overall, decreasing temperature within the range presented here creates a larger body of polarization from a more efficient polarization transfer step, but does not alter the general shape of the polarization distribution.

4.3 Variation of DNP length

The primary data explored by Beatrez et al. [24] shows the effect of an increase in polarization build-up. Comparable data measured on the cryogenic field-cycling experiment is presented in Figure 4.3. Here, the general experimental sequence described previously is unchanged, except for the hyperpolarization time τ which varies from 1 s to 90 s. The shuttling time of ~ 91 s is used for all experiments as this is limited by the shuttling of the cryostat into a high magnetic field (see Chapter 2). Figure 4.3A shows the S vs time decay profiles of these signals, smoothed with a moving average filter spanning 1000 data points, allowing us to distinguish the signal magnitude increase of individual datasets. Figure 4.3C plots the initial signal amplitude as a function of time and fits this build-up curve to an approximate monoexponential. We note that the fitting of this monoexponential build-up is consistent with the fact that the build-up is rate-limited by either the polarization build-up in the electron stemming from the laser or by the MW transfer to the nearby nuclei instead of spin diffusion [197]. Indeed, the laser and MW powers used for the collection of this dataset are low compared to those which Sarkar et al. [168] identified as the regime where spin diffusion would limit the rate of polarization spread.

The most interesting result that shows how spin lifetimes change as a function of hyperpolarization is the comparison of normalized spinlock decays shown in Figure 4.3B. Here, the decay profile extends slightly as a function of hyperpolarization, with the yellow-colored traces exhibiting a rightward shift as compared to the magenta traces. We note that the two traces corresponding to $\tau = \{1, 2\}$ s exhibit a high amount of noise even with the moving average filter. This result is similar to that published by Beatrez et al. [24]. They attributed this longer lifetime to the increased polarization being able to spread farther from the NV electron, which acts as a dissipator during RF readout. In Figure 4.3B, we note a more mod-

est change in lifetime than was observed by Beatrez et al.; this is likely due to the increased shuttling time of the instrument as opposed to the decreased temperature, creating a longer time under which spin diffusion can spread polarization away from the NV center electron.

We acknowledge several limitations in our effort to quantify this. It is not possible to vary the shuttling speed of the cryogenic field-cycling instrument to be shorter so as to more closely match the conditions of the room-temperature instrument used by Beatrez et al. and thus confirm the effect of diffusion. Nor is it effective to vary the time between polarization and readout on the room-temperature instrument (as was done later in Chapter 6) due to the fact that the shorter-lived lifetimes at room temperature would decrease the SNR of low hyperpolarization time τ experiments (which show the effect most dramatically) beyond what is experimentally readable. Either type of experiment would provide more conclusive results on the role of spin diffusion in this system. Ultimately, the results presented here act to corroborate the observations previously reported by Beatrez et al. [24] on a separate instrument and sample. We also demonstrate that the intuition regarding the build-up of polarization on transverse spin lifetime is largely independent of temperature.

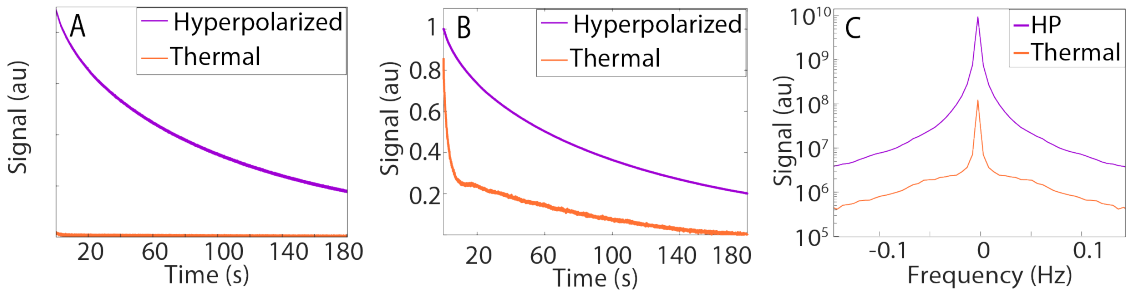


Figure 4.1 **Comparison of spinlock signals of hyperpolarized and thermally polarized states.** (A) Comparison of thermal (orange) and hyperpolarized (purple) spinlock signals at 100 K clearly demonstrates the SNR improvement from hyperpolarization. For the former, the diamond sample thermalizes in the high field of the magnet for 10 hr before measurement. The latter performs the hyperpolarization procedure for a hyperpolarization time of $\tau = 60$ s. (B) Comparison of normalized decay curves of thermal and hyperpolarized spinlock signals. An additional moving average filter with a bin of 1000 points is used for comparable visualization of the thermal spinlock signal. (C) Effective NMR spectra of spinlock time traces, obtained via FT and displayed on a logarithmic scale. Results indicate a >100-fold increase in SNR with DNP.

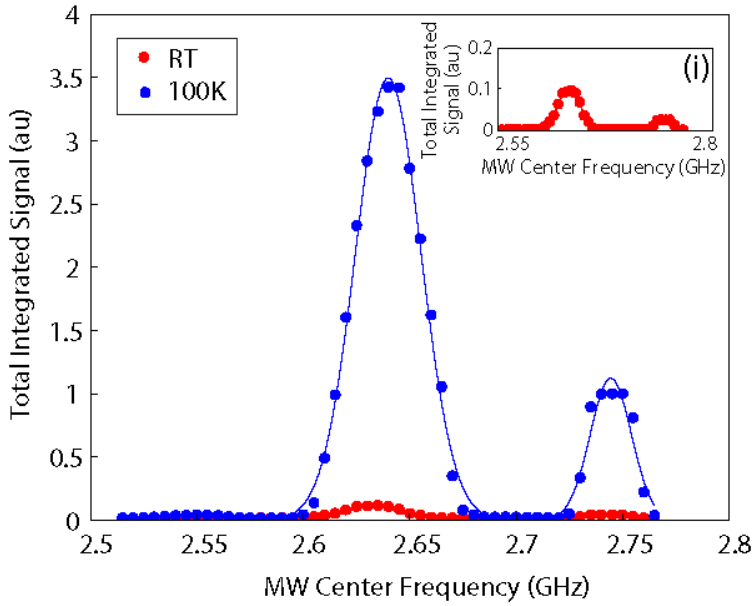


Figure 4.2 **EPR mapping of NV electrons via DNP.** DNP-mediated EPR spectra of NV centers at two temperatures (100 K and RT, also see inset (i)). Each point represents a 90 s-long optical DNP experiment performed with a 25 MHz MW bandwidth centered around the frequency of the point. A 60 s-long pulsed spinlock readout was used to determine the total integrated signal. Solid lines indicate a Gaussian fit. Peak broadening and the presence of a second peak at 2.72 GHz indicate poor overlap of the four NV center families at the chosen orientation, which is less effective for hyperpolarization but consistent across both measured temperatures (see inset (i)).

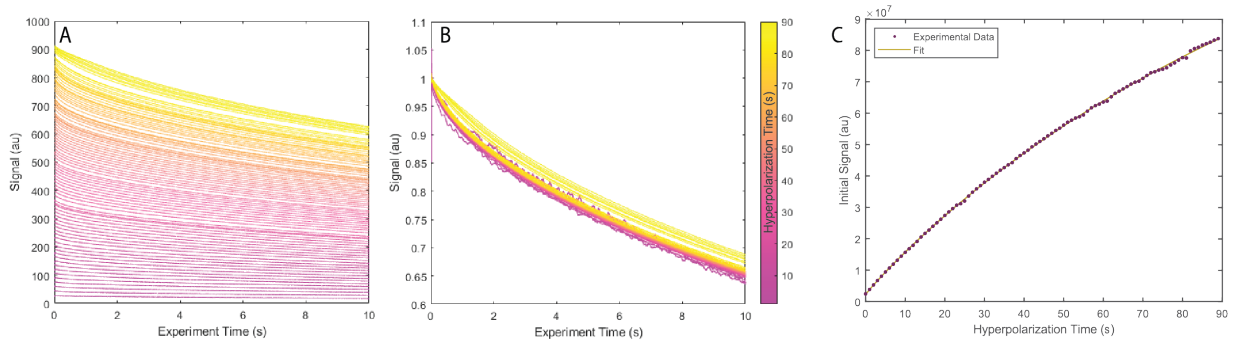


Figure 4.3 **Signal S vs time with differing hyperpolarization build-up times.** (A) Ninety spinlock signal curves show hyperpolarization build-up with variation of the applied hyperpolarization from $\tau = 1$ s (magenta) to $\tau = 90$ s (yellow). The signal increase as a function of increased hyperpolarization is readily apparent. (B) Normalized spinlock signal curves demonstrate the change in signal decay profile as a function of hyperpolarization. A slight increase in decay time from 1 s (magenta) to 90 s (yellow) of hyperpolarization is attributed to a greater spreading of hyperpolarization far from the fast-relaxing NV center. (C) Total initial signal of the decay profiles as a function of hyperpolarization time. The increase in signal is fit to an exponential build-up of the form $S(\tau) = A(1 - e^{-(\tau/T)^c})$, with $c \approx 1$.

Chapter 5

Laser-Induced Manipulation of Spin Lifetimes

The previous two chapters (Chapters 3, 4) have thus far demonstrated that the largest effect on ^{13}C nuclear spin lifetimes in our sample stems from the action of the electrons. Longer lived electron lifetimes, higher electron polarization, and the transfer of spin polarization away from the NV center have all demonstrated a contribution in extending the nuclear spin lifetimes. In this chapter, we directly target the electron via laser application to determine what effect it will have on nearby nuclear spin lifetimes.

Previous work optically addressing the NV center at cryogenic temperatures and high fields yielded exciting results [99, 171]. First, King et al. [99] discovered that under pure optical illumination (without the application of microwave frequencies to enforce a resonance condition), nuclear spins could become negatively polarized. They attributed this to fluctuations between electrons of the NV center and those of the electron spin bath, which could provide the necessary energy to stimulate a nuclear spin-flip transition. Scott et al. [171] later expanded the scope of these experiments to multiple samples of different NV^- and P1 concentrations from different manufacturers measured as a function of sample orientation in the magnet (the importance of which is discussed in Chapter 2.6 and later in Chapter 6.4). One of the samples used by Scott et al. (Sample #1) more closely matches with the sample used in this dissertation, having an NV defect concentration of ≈ 1 ppm, a P1 concentration of ≈ 20 ppm, and manufactured by Element6. Indeed, this sample was capable of being optically hyperpolarized at room temperature using a 532 nm linearly polarized green laser with a characteristic build-up time of ≈ 13 min, reaching levels of $\approx 0.07\%$ ^{13}C nuclear polarization [171]. The magnitude and sign of polarization were also greatly affected by the sample orientation, which the authors note marks a discrepancy in the theoretical mechanism elucidated earlier by King et al. [99], but no new mechanism was proposed.

It is with this background that our research optically targeting the NV center electron with a 532 nm laser during spinlock readout was undertaken. The amount of time reported by Scott et al. [171] necessary to build up polarization in the most comparable sample (~ 13 min) is slightly longer than the transverse nuclear spin lifetimes reported throughout

this dissertation ($\sim$ 2 min) but still within an order of magnitude. Thus, it is possible that nuclear spin polarization could be re-generated near the NV center or protected from NV-mediated dissipation through action on the NV center from laser application. However, should the orientation of the diamond sample result in positive polarization (compared to the negative polarization which is engendered through the DNP strategy discussed previously, see Chapters 1, 2.3, 4), or should the mechanism of electron fluctuations posited by King et al. [99] prove correct, this may accelerate signal decay instead.

5.1 Experimental Modifications

While the instrument, in principle, was designed to enable experiments in which the laser could be applied at a wide range of fields, several instrumental modifications were needed in order to actually perform these experiments. The software was modified in several respects, primarily to realign the laser when the sample is in the bore of the magnet at high magnetic fields. As noted in Chapter 2, the cryostat is not well aligned within the bore of the magnet and may move up to 2 mm with respect to the center of the bore across the shuttling trajectory. In addition, the laser applied during hyperpolarization must pass $\sim$ 6 ft uncorrected until it hits the sample, traversing the entire bore of the magnet; only a 45° mirror is used under the bore of the magnet due to the high magnetic field in its location. Mirrors used to perform alignment were located away from the bore of the magnet, adding an additional $\sim$ 3 ft through which the beam would pass after any minor correction. This instrumental description portends the challenge experienced when performing these experiments: the fact that the laser must be re-aligned at full power during shuttling between the hyperpolarization field and the high-field center before being returned to its original alignment to perform the next experiment.

Automated mirrors from Zaber had previously been installed to allow for fine adjustment; the mirrors were located at ankle-height and could be easily altered as a user re-sealed the laser safety enclosure. These automated mirrors were controlled exclusively by the computer and removed the need to open the laser safety enclosure entirely, making them an ideal choice for fine adjustments to the beam path while the laser is at full power. The necessary software modifications enabled the control computer to interact with the Zaber software, altering the positions of the mirrors in real time during the experiment. In addition, new experimental sequences were developed to turn the laser on at different times with respect to the start of the pulse sequence.

5.2 Continuous Laser Application

The effect of the laser is immediately obvious, as shown in Figure 5.1A. Here, the laser causes an immediate and notable reduction in spin lifetime, with T_2' decreasing from 53 s to 34 s when applied continuously during the 5-minute experiment. We note in Figure 5.1B that

this effect persists regardless of transmitter offset (data taken here at a 2.25 kHz offset, the importance of which will be discussed in Chapter 7).

The characteristic shape of the decay is not obvious. Relaxation theory in NMR typically treats relaxation as an exponential decay of the form

$$M(t) = M_0 e^{-t/T} \tag{5.1}$$

where $M(t)$ is the magnetization over time and T is the relaxation time constant [111, 97], which corresponds to a relaxation rate R. Here, the magnetization vector is assumed to come from one source of spins [30]; to treat multiple families of spins which relax differently, one can extend this equation to

$$M_i(t) = \sum_i M_{i,0} e^{-t/T_i} \ . \tag{5.2}$$

Ultimately, a large number of families which relax differently can lead to a broad distribution of rates R_i, which motivates the use of Inverse Laplace Transform in Chapter 7.

We note the use of T and T_i as the relaxation time constant instead of a more specific value, such as T_2, which is typically considered in relaxation theory [111, 30]. This is due to the use of a spinlock pulse sequence for which the relaxation time constant can be thought of as $T_{1\rho}$ or T_2'. While thus far in the dissertation, we have frequently described the relaxation as T_2', it would be appropriate to consider this a $T_{1\rho}$ as well. The spinlock sequence acts in such a way that the spins thermalize to the protected axis (as will be later described in Chapter 6), making their relaxation behavior similar to T_1 relaxation albeit in the rotating frame of that protected axis. This behavior is maintained, even when the protected axis is tilted away from $\hat{\mathbf{x}}$ (as will be described in Chapter 7).

Thus far, relaxation has been presented and discussed as though it behaves monoexponentially. However, one can easily see how this description is not sufficient with differing families of spins, such as those at different distances from paramagnetic defects. Indeed, previous literature has reported non-exponential relaxation behavior in glasses when spins coupled to different paramagnetic relaxation sources and experiencing slow spin diffusion contribute inhomogeneously to the overall relaxation, resulting in a stretched exponential behavior [184]. Previous work had also noted this stretched exponential behavior when spin diffusion was slow, although only at short experimental times [188].

Fitting the exponential decays from Figure 5.1A-B, therefore, is non-trivial. While we expect spin diffusion to play an active role in our spin system (see Chapter 6), previous work on this hyperpolarized NV diamond system has demonstrated a stretched exponential character [25, 24]. After fitting to both a stretched exponential ($\beta = 0.5$) model (Figure 5.1C) and a single exponential model (Figure 5.1D), it was determined that the stretched exponential model fit better based on comparison of residuals in Figure 5.1C-D(ii). Notably, a systematic error persists through both datasets, with a concave curvature of residuals in Figure 5.1C(ii) in contrast to a convex curvature of the residuals in Figure 5.1D(ii). This indicates that neither a stretched nor a single exponential approximates the dataset well; this data instead appears to be in an intermediate regime.

A new manuscript by Selco et al. [173] (which will be discussed in Section 5.4) has identified this intermediate regime as being a linear combination of a stretched exponential ($\beta = 0.5$) and monoexponential. Interestingly, the data shown in Figure 5.1B where a transmitter offset of 2.25 kHz is applied to protect the transverse axis along the magic angle, identified by Selco et al. as a region where a stretched exponential ($\beta = 0.5$) ought to fit well, still shows concavity in Figure 5.1C(ii).

Regardless, further analysis in this chapter will be performed assuming that the relaxation behavior of the spins under both conventional spinlock and the application of laser during conventional spinlock follows a stretched exponential ($\beta = 0.5$) model, as per the analysis by Beatrez et al. [25].

5.3 Block Laser Application

Here, we turn our attention away from the total effect of the laser on the sample. Instead, we focus on the question of whether the mechanism of action of the laser on the NV center has a distance-dependent effect on the ^{13}C nuclear spin ensemble. Should the electron be relaxing proximal nuclear spins through fast fluctuations, this effect ought to act more strongly at the beginning of the experiment. After an initial depolarization period of the nearby spins, the effect of the fluctuations would then be limited by the ability of bulk ^{13}C spins to undergo spin diffusion back into the domain of the fast-fluctuating NV center, decreasing the rate of decay caused by the laser.

Data shown in Figure 5.2 depicts the results of the application of a 532 nm laser in "blocks" of 1 s. (Throughout this chapter, the term laser "block" is used to describe the finite interval of laser illumination. This terminology is adopted to avoid confusion with a pulsed laser, as all experiments presented herein employ a continuous-wave (CW) laser.) Figure 5.2A depicts a full set of spinlock datasets in which a laser block is applied for 1 s at times incremented by 0.5 s. The laser start time is sequentially varied from the start of the experiment (yellow) to 69 s (the last second of the experiment, green). Notably, the modest decay in signal of only 1 s of laser application is obscured by the vast number of experiments; for clarity, a small subset of ten experiments is presented in inset Figure 5.2A(i) from the laser start time $t_L = 17$ s to $t_L = 21.5$ s. Here, the abrupt change of decay rate upon application of the laser is obvious, followed by the return to the original decay rate once the laser is turned off.

Unfortunately, the biggest flaw with this data is also readily observable from the inset: the decay due to the laser is not evenly spaced every $t_L = 0.5$ s as the experiment was intended. Instead, through a flaw in the laser block timing, experiments from $17.5 \leq t_L \leq 19, t_L = 21.5$ s were timed correctly, while $t_L = 17$ s actually started the laser at 17.5 s and $19.5 \leq t_L \leq 21$ s all applied the laser at 21.5 s. While the block timing was subsequently corrected for later experiments, this was the only dataset of its type collected.

In Figure 5.2B, we present the rate of relaxation that occurs when the laser is turned on. This is calculated from the data in Figure 5.2A, as well as from a dataset taken immediately

prior, in which no laser block was applied. The dataset which does not have a laser delay is fitted to a stretched exponential:

$$M(t) = M_0 e^{(-t/T)^\beta} \tag{5.3}$$

If we consider the rate $R_{st}(t)$ to be the background relaxation that would have continued regardless of the effect of the laser, and R_L to be the independent rate of relaxation stemming from the laser, then the decay in magnetization during a laser block is:

$$\frac{dM(t)}{dt} = -\left(R_{st}(t) + R_L\right) M \tag{5.4}$$

Integrating over the laser block to solve this differential equation yields

$$\ln\left(\frac{M\left(t_L + \Delta t\right)}{M\left(t_L\right)}\right) = -\frac{\left(t_L + \Delta t\right)^\beta - t_L^\beta}{T^\beta} - R_L \Delta t. \tag{5.5}$$

where Δt is the 1 s length of the laser block. R_L is calculated directly from the rearrangement of this equation, where $M\left(t_L\right)$ and $M\left(t_L + \Delta t\right)$ are calculated by averaging the spinlock signal S of $\sim$ 50 ms before and after the laser block, respectively. Figure 5.2B then plots these relaxation rates as a function of the time at which the laser block is started, t_L.

We note that the most obvious feature of this plot is the oscillations. These are purely an artifact of the mistimed laser blocks: when the laser is not applied, the rate difference between the background decay from the stretched exponential and the decay in the data is negligible (it follows the stretched exponential well). One would expect that the calculated R_L in this case would be null, and indeed we find that in these data points $R_L \approx 0$. Several laser blocks are such that, though the start time is incorrect, the actual application of the laser overlaps with the expected laser block, resulting in some decay and thus a non-zero R_L. To separate these, all datasets were inspected by eye to determine which laser blocks were applied at the correct time; all rates in Figure 5.2B calculated from mistimed laser blocks are shown in mint green.

We also note there are two data points shown in gray; these correspond to datasets for which $t_L = 53, 68$ s. In Figure 5.2A, these are the two datasets that exhibit extreme arcing resulting in complete loss of signal around 10 s. The resulting calculated "decay" in S is minimal; yet the stretched exponential also anticipates a very small comparable decay, resulting in R_L values that, while meaningless, are comparable to real R_L values. This also speaks to the need to confirm this data with properly calibrated laser blocks.

Finally, we consider the data in dark green, which represents the R_L calculated during the application of the laser. While generally steady across the experimental time, a sharp increase in rate is followed by a slight decrease occurring steadily after $t_L \approx 5$ s. This decrease is enticing; given that later experimental times probe spins progressively farther from the NV centers, the observed decrease is consistent with the laser exerting a spatially varying influence on the ^{13}C nuclei. Should the proposed laser-induced fluctuations be the mechanism of action, these fluctuations would dissipate spin polarization nearby, requiring

spin diffusion to return polarization to the vicinity of the electron. As the experiment progresses, less polarization is diffused into the region of influence of the electron from larger distances, resulting in a decrease in the rate of decay caused by the electron.

It is unlikely that this decrease is due to heating or any other form of temperature effect; all experiments are performed under equal cryogenic conditions and the laser is applied for an equal amount of time (1 s) for every dataset. (The total time of the laser application is unaffected by the mistimed initiation of the laser block.)

The shape of the observed decay is impossible to deduce based on the dataset presented here; rather we present this hypothesis in order to stimulate interest in the possibility that the effect of the laser may be directly measurable over the course of an experiment.

Ultimately, no definite conclusions can be drawn from this data without careful calibration of laser timing and a deeper understanding of the specific decay behavior governing the background (no laser applied) relaxation. Moving forward we would recommend this type of dataset being collected at a transmitter offset value such that the spins are locked at the magic angle and the relaxation behavior is well-approximated by a stretched exponential of $\beta = 0.5$. Ultimately, if the data were taken with increasing laser power, the average rates would be expected to increase as per Selco et al. [173]; however, cleaner data may reveal an interesting dependence on experimental time, allowing mapping of the decay rate during the experiment to the action of the electron.

5.4 Extensions to Decoherence Model

Although the above analysis has been performed in the context of a recent manuscript by colleagues Selco et al. [173], the data presented in this chapter was collected several years prior (hence the laser block timing errors which have since been resolved). Indeed, progress on this analysis was limited without the key advancements presented by Selco et al., namely the decoherence model that treats the spinlock decay as a product of a monoexponential and stretched exponential, where regimes can be identified in which each dominates.

Selco et al. built on discoveries presented in Chapter 7 in which the transmitter offset is used to tune the angle of the axis protected by the pulsed spinlocking sequence. Here, they use both regimes identified in Chapter 7 to determine the primary method of decoherence: a stretched exponential with $\beta = 0.5$ dominates when the spinlock axis is along the magic angle, while a monoexponential dominates when the spinlock axis is tipped nearly to the $\hat{\mathbf{z}}$ axis [173, 85]. They further extend these observations by repeating them as a function of laser power, noting that both the stretched and monoexponential mechanisms change when not suppressed by the pulse sequence.

An impressive addition presented by this work is the attribution of the stretched exponential decay stemming from fluctuations of the paramagnetic center in the absence of spin diffusion, while the monoexponential decay describes spin-diffusion-dominated processes, which can be observed as the paramagnetic dissipation is suppressed [173]. These conclusions are corroborated by previous work by Tse et al. [188] and Stockmann et al. [184], who

observed similar behavior in different samples. Selco et al. support their model with extensive simulations and theoretical modeling to better understand the complex dynamics [173].

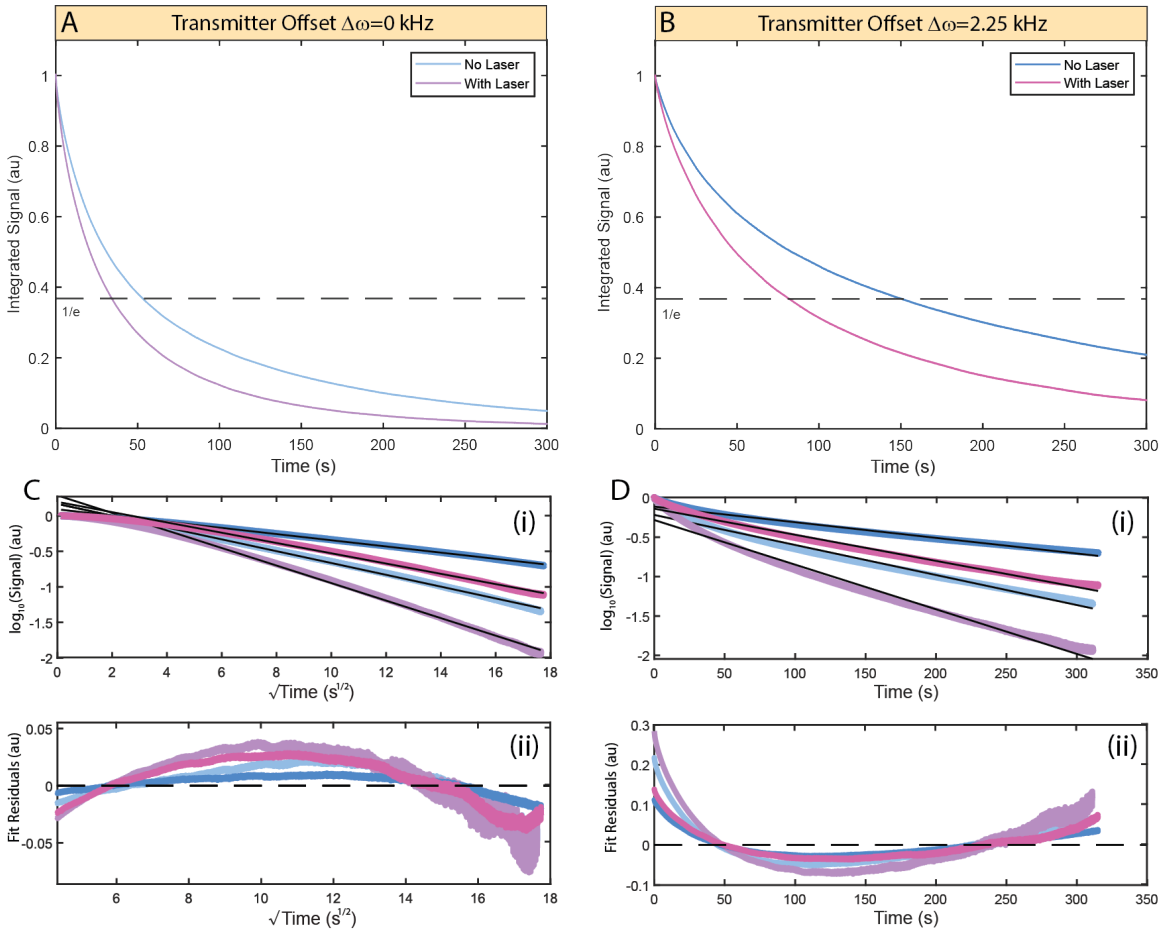


Figure 5.1 **Effect of laser application on spinlock dynamics.** (A) Pulsed spinlock signal S vs time decay curves comparing the application of a 532 nm CW laser during RF acquisition (purple) to a comparable dataset where no laser is applied during RF acquisition (light blue). Here, the spinlock pulses are applied on resonance ($\Delta\omega = 0$ kHz). (B) Pulsed spinlock signal S vs time decay curves comparing the application of a 532 nm CW laser during RF acquisition (pink) to a comparable dataset where no laser is applied during RF acquisition (medium blue). Here, the spinlock pulses are applied off resonance such that the protected spinlock axis is along the magic angle ($\Delta\omega = 2.25$ kHz). (C) Fitting of all spinlock curves from A–B to a stretched exponential model with stretching factor $\beta = 0.5$. (i) The fits (black) are plotted against their respective datasets on a log vs $\sqrt{t}$ axis such that the fits are depicted linearly. (ii) The residuals of the fits are plotted, demonstrating concave curvature across all four datasets. (D) Fitting of all spinlock curves from A–B to a monoexponential. (i) The fits (black) are plotted against their respective datasets on a log vs t axis such that the fits are depicted linearly. (ii) The residuals of the fits are plotted, demonstrating convex curvature across all four datasets, with greater magnitudes of residuals than those of the stretched exponential fit in C for all four datasets.

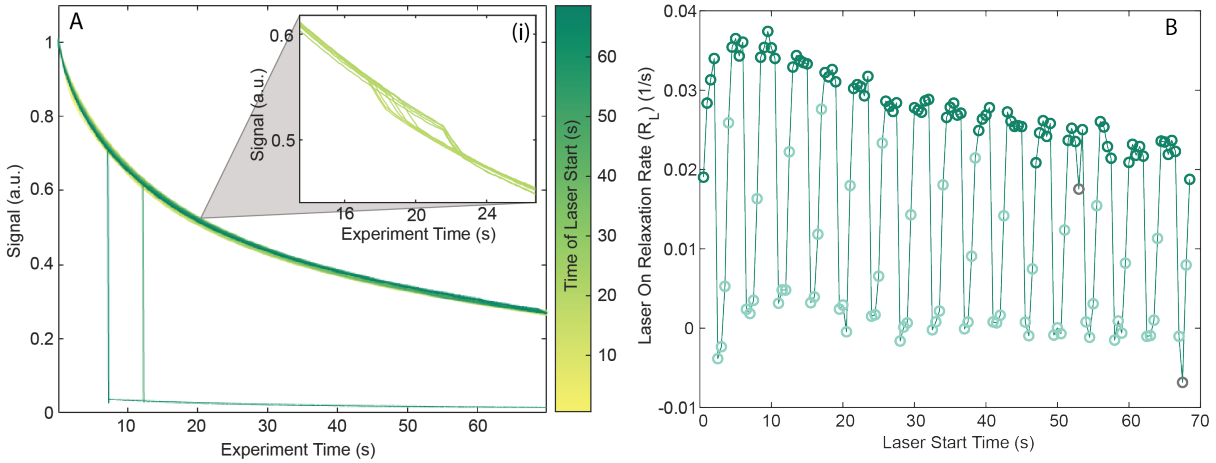


Figure 5.2 **Investigating rate of laser-induced decay.** (A) Pulsed spinlock signal S vs time decay curves on which laser "blocks" of 1 s each are applied starting from $t_L = 0$ s (yellow) to $t_L = 69$ s (green). Notably, two curves corresponding to data where $t_L = 53, 68$ s experience arcing that reduces the signal to zero. Inset (i) depicts a subset of 10 datasets where $17 \leq t_L \leq 21.5$ s for clarity. Here, the rapid decrease in signal upon application of laser and subsequent return to typical decay upon its termination are readily apparent. (B) Calculated relaxation rates R_L due to laser application, plotted as a function of t_L. Mistiming of laser blocks stemming from the pulse sequence results in miscalculated R_L rates (plotted in mint green). R_L rates calculated from laser blocks that were applied correctly are plotted in dark green and show slow decay over the experiment. R_L rates calculated from datasets that demonstrate arcing in A are plotted in gray.

Part IV

Pulse Sequence Control

Chapter 6

Development of Hyperpolarized "Shells"

In the introduction of this dissertation (Chapter 1), the "pulsed spinlocking" sequence which is used for all previously shown data was described in great detail. This sequence was demonstrated in previous work [25] to extend the coherence time of the nuclear spins in our system. It was also used in that work to provide insight on the thermalization process.

Thermalization and, more broadly, how quantum systems approach equilibrium is of interest to a variety of research areas including the Eigenstate Thermalization Hypothesis for closed quantum systems [180, 160, 52], anomalous transport and emergent hydrodynamics [202, 194, 196], and the creation of prethermal ordered states of matter [62, 117].

Thermalization in quantum systems proceeds analogously to its classical counterpart: entropy grows with time, erasing traces of the system's prior history and gradually reducing accessible information. In most cases, such loss of information is irreversible, impeding the capacity to harness quantum systems. Consequently, a broad endeavor has been underway to retard, even preclude, these thermalization processes. Techniques range from physically isolating quantum systems (e.g., in vacuum) or through quantum control [193], cooling them to temperatures near absolute zero [31], or, in a complementary manner, exploiting theoretical paradigms of many-body localization to inhibit the onset of thermalization [2].

In nuclear spin systems, this loss of information corresponds to the loss of spin coherence. Viewed through this lens, the methods detailed in this dissertation for extending relaxation times and thus delaying or halting spin thermalization can be understood as an NMR-focused approach to this endeavor: how to preserve information in quantum spin systems against the tendency toward thermal equilibrium.

The thermalization process is often depicted as leading to mundane, featureless states that are set by the bath from the world around them. However, this chapter explores a specific method where thermalization leads to stabilized shell-like nuclear spin polarization textures; a surprising feature considering the relatively high temperatures (> 100 K) under which we are working.

These shell-like textures are formed in the same system of NV diamonds with which

we have been working in this dissertation. In this chapter, the role of the NV center will be placed under stronger scrutiny. In addition to serving as the polarization "injector" (as described in detail in Chapter 1), the electron spin character of the center also serves as a localized polarization sink. Indeed, this was briefly touched on as part of the rationale for exploring low temperatures in Chapters 2 and 3. The electron spin also serves an additional role: creating a hyperfine interaction which is dependent on the interaction distance. This acts as an "antenna" creating a nanoscale radially dependent gradient field across the system of ^{13}C spins.

With the addition of a time-periodic drive created by a variation on the pulsed spinlocking sequence, the nuclear spins in the system prethermalize [164, 67, 144] to a metastable state [89] that contains these spin shells with constant-in-time domain boundaries. Indeed, the shells (which we refer to as "Hamiltonian Engineered" [37, 74, 57]) are stable over a measurement period of several minutes and are estimated to span several nanometers in real space.

While a similar spin texture can be created by hyperpolarizing the nuclei successively with opposite sign, such that a shell of positively polarized ^{13}C spins is formed around a core of negatively polarized ^{13}C spins, this method of "State Engineered" spin texture lacks stability and nuclear spin diffusion melts the domain boundary [48] as a result of thermalization.

In this chapter, we will first investigate the "State Engineered" method of forming spin shells so that we can identify where thermalization and spin decoherence contribute to the loss of system information (Section 6.1). We will then discuss the "Hamiltonian Engineered" method of stabilizing spin shells against thermalization in Section 6.2 with associated experiments that further elucidate the behavior of the spins in Sections 6.3 and 6.4. Important theoretical calculations and simulations which confirmed the surprising stability of the shells are presented in Section 6.7.

This chapter is adapted from Ref. [84] to which many people made notable contributions. In particular, we must acknowledge N. D'Souza and Dr. D. Marchiori as equal co-authors. Furthermore, Dr. W. Beatrez and Q. Reynard-Feytis provided all data shown in Section 6.1. Under the supervision of Dr. M. Bukov, all theory work presented in this chapter was performed by collaborators Dr. C. Fleckenstein, P. Schindler, and Dr. C. Artiaco as equal co-authors.

6.1 Method of Hyperpolarization Injection

The Hyperpolarization Injection method to create an initial shell-like state does not differ greatly in protocol from a typical hyperpolarization scheme as detailed in Chapter 1. In a sample of NV diamond (sister to that which has been discussed previously, with identical characteristics), first positive and then negative hyperpolarization [13, 10] is performed for periods τ_+ and τ_-, respectively (Figure 6.1A inset). Note that the sign of polarization can be flipped based on the sign of the slope of the MW chirps that are applied [10]. Direct ^{13}C hyperpolarization occurs rapidly over a short range, with distant nuclei polarized more

slowly via spin diffusion. Thus, the hyperpolarization strategy works by first polarizing the ^{13}C nuclei close to the NV center, allowing the polarization to spread to more distant nuclei while being constantly replenished. Then the negative polarization begins but only in the ^{13}C nuclei close to the NV center. Since the more distant nuclei are left positively polarized, a shell-like texture emerges. Varying τ_- at a fixed τ_+ provides a means to tune the shell size.

The resulting net ^{13}C polarization can be tracked over many spin-injection experiments, as shown in Figure 6.1A. The positive spin injection is varied up to τ_+=60 s after which the sign of the injected polarization is reversed (dashed vertical line). In the boxed region around $t_{pol}\approx$100 s (τ_-=40 s) the total net polarization approaches zero. Although there is limited net polarization, the system can still exhibit shells of locally large spin expectation.

At this point, a typical spinlock experiment can be performed to observe the created shell-like state. These experiments utilize the typical pulsed spinlocking sequence described in Chapter 1 but it is notable that they are performed on a B_0 = 7 T room-temperature field-cycling apparatus, described in Ref. [11]. This apparatus is notable for its fast shuttling speeds from the hyperpolarization position into the magnet bore for a pulsed spinlocking experiment of $<$ 0.5 s.

Figure 6.1B(i) shows signal amplitude S vs experiment for a select (boxed) set of polarization build-up experiments summarized in Figure 6.1A. We consider first the signal curve associated with point *(a)* at the top of the polarization build-up curve in Figure 6.1A (τ_-=0). This dataset is a result of purely positive polarization with no shell structure formed and can thus be considered the profile of a typical spinlock under these experimental conditions. Shown as a black dashed line in Figure 6.1B(i), the signal curve demonstrates a long-lived decay with an associated T_2' lifetime of $\sim$93.4 s as a result of $\hat{\mathbf{x}}$ (quasi-)conservation by an effective spinlock [25].

In comparison to this slow, featureless decay, the signal profiles from the zero total net polarization region (boxed in Figure 6.1A) exhibit distinct differences. As an example, let us consider the representative trace shown in bold orange in Figure 6.1B(i), in which τ_-=44.8 s. A sharp feature shows the normalized signal goes steeply to zero at t=t_{zc} ($\approx$11.34 s) and recovers to the envelope predicted by decay curve (a). As the signal amplitude reflects the magnitude of the projection on the $\hat{\mathbf{x}}/\hat{\mathbf{y}}$ plane, we turn to the phase data in Figure 6.1B(ii) to determine the cause of this feature.

Notably, Figure 6.1B(ii) demonstrates an abrupt reversal in total net polarization sign from $-\hat{\mathbf{x}}$ to $+\hat{\mathbf{x}}$ at the same time as the feature in Figure 6.1B(i). This indicates that the feature is a zero-crossing between net negative and net positive polarization.

The other colored traces in Figure 6.1B(i) show corresponding signals S for different τ_- (see color bar). Note that the zero-crossing point t_{zc} shifts to the right with increasing τ_-. The t_{zc} values for the data shown in Figure 6.1B(i,ii) as well as additional t_{zc} values for subsequent τ_- data sets are pictured in Figure 6.1B(iii), showing the rapid rightward shift. A movie showcasing data for 151 changing values of τ_- is accessible online [84].

One might naively imagine that, since the NMR measurement being taken is an average magnetization, the successive positive and negative polarization would simply cancel out the total signal and yield a decay curve similar to that of (a) which simply decreases in

magnitude as the relative proportion of negative polarization increases and overtakes that of the positive polarization. Indeed, this happens — to an extent. Since the data in Figure 6.1B is normalized to demonstrate the surprising profile of the feature, this figure fails to convey that the signal curve from point (a) is an order of magnitude larger than those of the colored curves. The zero-crossing only occurs, then, when the net polarization is near zero, alluded to by the selection of the boxed data in Figure 6.1A.

To rationalize the formation of the zero-crossing in Figure 6.1B, recall that we earlier stated that the NV electron acts as a polarization sink [24]. It is strongly coupled to a phonon bath to which the ^{13}C spins are only weakly coupled. Consequently, the NV acts as a dominant local relaxation source for the ^{13}C nuclei; proximal nuclei (with a dependence of $\sim 1/r^6$) dissipate polarization faster than more distant ones. A treatment of this dissipation with the Lindblad master equation in the strong coupling limit is shown in the SI of Ref. [84]. Measurements at longer times (t), therefore, probe nuclei progressively further away from the NV as ^{13}C closer to the NV (with relaxation times $< t_m$) are no longer polarized and do not contribute to the signal.

Figure 6.1C shows a schematic representation of the polarization distribution as the experiment progresses, focusing on specific points (I-IV) along the bold orange trace (τ_-=44.8 s) in Figure 6.1B. The polarization distribution is shown as spherical shells for simplicity; in reality, it possesses an angular dependence inherited from the hyperfine interaction that is discussed later in Section 6.7. This simplistic picture is sufficient to demonstrate the interplay between spin diffusion and relaxation which causes the formation of these shells.

The initial texture shown in Figure 6.1C(I) is the state at ($t = 0$), immediately after hyperpolarization and shuttling into the magnet. Here, red areas correspond to positive polarization while blue areas correspond to negative polarization. Due to the short timescale, we represent the state as having well-defined shells and the NV has not yet had time to act as a polarization sink. Subsequently, both spin diffusion and dissipation from the NV center begin to act, creating regions of no polarization (white). The zero-crossing at $t = t_{zc}$ corresponds to an equal distribution of positive and negative polarization, as shown in Figure 6.1C(II). Further dissipation leads to a polarization sign inversion (Figure 6.1C(III-IV)). The overall radius of the outer shell continues to expand as the system progresses from point (I) to (IV) due to spin diffusion continuing to spread polarization to unpolarized bulk spins. Spin diffusion also acts between the oppositely signed polarization shells, flattening the polarization landscape. Overall, Figure 6.1 illustrates the ability to discriminate spins without relying on the electronic "frozen core", constituting a departure from previous work [183, 127].

The last section of this figure (Figure 6.1D) shows the ^{13}C NMR spectrum for data corresponding to 91 τ_- values from $\tau_- = 30$ s to $\tau_- = 48$ s. These were obtained by applying a Fourier transform (FT) to the sign-corrected decay curves in Figure 6.1B; Figure 6.1D(i) demonstrates an exemplary set of three at $\tau_- = \{30, 34, 37\}$ s. These FT data sets shows a noticeable narrowing in the spectral linewidth and decrease in background Fourier intensity followed by a sharp increase in the background intensity and subsequent widening of the spectral linewidth. This was initially attributed to the changing shell radii and zero-crossing

feature, as shown in Figure 6.1C; however, we believe that this should instead be analyzed with an overall understanding of shell polarization in the initial state. ^{13}C spins closer to the NV produce broader spectral lines because they experience faster relaxation. They can thus be seen to contribute to the spectral wings around 0 Hz. Conversely, more distant, bulk ^{13}C nuclei are centrally located in the spectrum due to longer relaxation times. As τ_- increases, the negative polarization forms in the nuclei near to the NV center; the net positive polarization therefore comes primarily from the long-lived bulk nuclear spins leading to the observed spectral narrowing. As the negative polarization continues increasing with τ_-, there is a point where the total net polarization changes from positive to negative. This occurs at $\tau_- \approx 37$ s with a faint discontinuity in the baseline arising from the apparent "reappearance" of the nuclei nearest to the NV center. Indeed, this data indicates the minimum amount of negative polarization which must be injected in order to form a shell structure which manifests as a zero-crossing.

The effect of spin diffusion inherently makes the "State Engineered" spin texture unstable. Over time, any injected domain boundaries dissolve regardless of the action of the NV center as a sink. This loss of spin texture can be observed in experiments where a delay period t_{wait} is introduced before the spins are tipped into the $\hat{\mathbf{x}}/\hat{\mathbf{y}}$ plane and driving is started (see Figure 6.2A). This delay period happens after shuttling, while the sample is in the magnet, where the NV-driven dissipation of the still-$\hat{\mathbf{z}}$-polarized ^{13}C spins is negligible. The orientation of the spins in the $\hat{\mathbf{z}}$ direction means that the energy of the noise necessary to relax the spins increases to the Larmor frequency $\gamma_n B_0$, as opposed to the Rabi frequency Ω when nuclear spins are precessing in the $\hat{\mathbf{x}}/\hat{\mathbf{y}}$ plane. This higher energy barrier is reflected in the extremely long nuclear lifetimes $T_1 \approx 1$ hr in the 7 T magnet center. Consequently, spin dynamics in the t_{wait} period is primarily affected by spin diffusion.

Figure 6.2B shows the signal S dependence on the delay period t_{wait}, starting from a spin texture produced with $\tau_+ = 60$ s and $\tau_- = 42$ s. These parameters were chosen as they are known to produce a spin texture at an early t_{zc}. As t_{wait} increases, the signal curves flatten as the negative and positive polarization diffuse into one another, resulting in an unpolarized region at the boundary. Because of this, as well as the spin diffusion pushing positive polarization into the surrounding bulk spins, a rightward shift of t_{zc} is also observed. A schematic representation of how spin diffusion acts as t_{wait} increases is shown in Figure 6.2C.

We can track the effect of spin diffusion on both of these parameters by plotting t_{zc} as a function of t_{wait} (Figure 6.2D) and by plotting the normalized value of the signal at a fixed value of t as a function of t_{wait} (Figure 6.2E). Note that the normalization is against the signal at $t_{wait} = 0$ s. The fixed value of t is chosen to be $t = 50$ s, which occurs after the signal recovers from the zero-crossing for all included data sets. We compare this plot of signal intensity at t to the signal intensity at t for a homogeneously polarized state ($\tau_- = 0$ s), where the normalized signal instead increases slightly with t_{wait}. In this case, spin diffusion pushes polarization away from the NV, and thus is less affected by dissipation when the experimental RF sequence begins. These observations are supported by numerical simulations (Figure 6.2F–G) performed by collaborators [84] and are notable

for all qualitative features being well reproduced.

6.2 Method of Hamiltonian Engineering

A surprising observation led to the discovery of a more stable method of generating spin texture. When deploying the pulsed spinlocking sequence with flip angle $\theta \approx \pi$ (Figure 6.4A), we observe that over time, the signal S exhibits a sharp zero-crossing and subsequent sign inversion. This is surprising for several reasons: first, the initial state of the ^{13}C spins is positively polarized ($\tau_+ = 90$ s, $\tau_- = 0$ s) with no possible injection of negative polarization; and second, extensive use of π-trains (CPMG experiments [39, 125]) across various contexts including dynamical decoupling and quantum sensing has never, to the best of our knowledge, given rise to this phenomenon.

We attribute the creation of this texture to our particular system, and specifically to the NV electron's capability for generating a nanoscale hyperfine magnetic field gradient $\eta(\mathbf{r})$ imposed on the nuclear spins (schematically shown in Figure 6.3A as a pink gradient). As a consequence, the direction and magnitude of the Rabi field (Ω) experienced by the nuclei depends on their proximity to the electron.

This NV field gradient acts on the nuclear spins in all experiments, including those presented in Section 6.1. When $\theta \neq \pi$, this creates a slight alteration of the effective spinlock axis $\hat{\mathbf{x}} \rightarrow \hat{\mathbf{x}}'(r)$ (derived explicitly by our collaborators in the SI Section 8B of Ref. [84]). On the other hand, when $\theta = \pi$ exactly and we ignore the NV-induced gradient field, the absence of $\hat{\mathbf{x}}$-polarization conservation leads to the rapid decay of the spins within T_2 [25, 8], as would be governed by an un-optimized CPMG sequence.

The shell-like texture is thus only created when the field gradient of the NV center is dressed by the (near) π-train drive. We can consider the average Hamiltonian for the system when a train of $\theta = \pi + \epsilon$ with $|\epsilon| \ll \pi$ pulses is applied to ^{13}C spins in the NV field $\eta(\mathbf{r})$ (again derived in detail in SI Section 8B of Ref. [84]):

$$\mathcal{H}_{eff} = \mathcal{H}_{dd} + \sum_{\mathbf{r}} \varphi_{\mathbf{r}} I_{x,\mathbf{r}} \tag{6.1}$$

Here, $\varphi_{\mathbf{r}} = \eta(\mathbf{r}) + \epsilon/\tau$ describes the effective potential which the ^{13}C spins experience (Figure 6.3C). Spatial discrimination comes primarily from the spatially varying field $\eta(\mathbf{r})$. While the hyperfine interaction will also shift the ^{13}C nuclear spins' nominal angle away from π (a feature that is encapsulated in ϵ), we primarily consider our system to be that of bulk spins where this effect is weak. Another way of describing this is to consider that we are in the regime where the electronic field gradient is weak ($\varphi_{\mathbf{r}} < 1$ kHz), and thus we are not investigating the spins in the frozen-core limit [3, 183].

A key feature of this potential can be seen when $\epsilon < 0$. If the radially decreasing field strength $\eta(\mathbf{r})$ is weak enough such that $\eta(\mathbf{r}) < \|\epsilon/\tau\|$, the on-site potential will flip sign from positive ($\varphi_{\mathbf{r}} > 0$) to negative ($\varphi_{\mathbf{r}} < 0$) for far-away nuclear spins. This sign flip occurs at a critical radius r_c which is determined by the ^{13}C slice for which $\varphi_{\mathbf{r}} = 0$ (Figure 6.3C).

Crucially, the sign change of $\varphi_{\mathbf{r}}$ on either side of r_c means that the Hamiltonian governing the system, $\mathcal{H}_{eff}$, internally encodes spatial structure with r_c serving as the domain boundary. This means that, regardless of initial state, the $\hat{\mathbf{x}}$-polarization will thermalize to opposite signs on either side of r_c, forming the quasi-equilibrium "shell" within the prethermal plateau (Figure 6.3B).

The data shown in Figure 6.4B–C depicts the signal S vs time plots for such shell formation on linear (B) and logarithmic (C) scales, respectively. A full accounting of the traces during shell formation and under typical spinlock conditions where no shell formation occurs is presented in Figure 6.5, indicating that the shell recovery is comparable to that of Figure 6.1. Figure 6.5D also demonstrates the repeatability and stability of the experiment with > 10 data sets overlapping perfectly. We also note that there is no phase data presented in Figure 6.4 as there was in Figure 6.1. This was due to a small bug in phase data correction for the particular dataset shown in Figure 6.4B; however, the phase behavior is identical to that shown in Figure 6.1. Further confirmation of this is presented in Section 6.3.

Another feature of note is that the data in Figure 6.4B demonstrates a sharp initial decay which evens out followed by the zero crossing. Later experiments determined that this was likely caused by differences in transmitter offset and sample alignment, discussed later in Section 6.4. Note that this initial decay and evening out does not occur in Figure 6.4C, as the logarithmic data is taken from an analogous data set which does not exhibit initial fast decay.

A trace in Figure 6.4B is highlighted in purple for visibility, corresponding to a pulse train pulse angle of $\theta = 0.94\pi$. Here again, different notable regions in the data set are indicated by (I-IV) which are depicted schematically in Figure 6.4D. In (I), the initial state of the system is shown, where only positive hyperpolarization is generated nearby the NV center, with $r_{hp} < r_c$. By (II) the polarization has spread to near r_c. The point of the zero crossing is shown in (III) where the generation of negative polarization from thermalization to the potential $\varphi_{\mathbf{r}}$ surpasses the amount of positive polarization in the system. Finally, in (IV), the negative polarization continues to grow until spin relaxation starts to decrease the absolute value of the signal.

We note a key nuance in how the polarization spreads. While Section 6.1 focused on the interplay of spin diffusion and dissipation from the NV center the thermalization dynamics discussed here must be understood in terms of energy diffusion, as it is immediately obvious that the formation of negative polarization indicates a lack of polarization conservation. The initial state of the system is far from the equilibrium set by $\mathcal{H}_{eff}$, thus it possesses energy which can diffuse throughout the system via (quasi-)conservation. This drive towards equilibrium is what creates negative polarization outside of r_c, and, as the domain boundary is created only in the equilibrium state, is what stabilizes the formation of the domain boundary against spin diffusion on prethermal time scales ($t < T_2'$). Indeed, this stabilization of the boundary was surprising from experimental data alone; it was only with simulations and modeling from our theory collaborators that this energy diffusion picture was reached. It is described in great detail in Section 9 of the SI of Ref. [84].

The different green-colored traces in Figure 6.4B show S vs time for values of θ in the

vicinity of $\theta{=}\pi$ (see color bar). The zero-crossing position is observed to change with θ. A movie of this data is accessible online via Ref. [84]; by viewing it in movie form, it is apparent how the change in zero-crossing moves with pulse angle θ. We attempt to convey this change in t_{zc} using a 2D plot in Figure 6.4E for 120 different values of θ. Here a logarithmic scale in intensity is used, where the darker blue colors highlight the zero crossing. Notably, a distinct dataset, where no zero crossing is observed, displays rapid signal decay (indicated by the dashed line). This is attributed to bulk ^{13}C nuclei, which are far removed from the NV influence, corresponding to $\theta = \pi$. This qualitative behavior can be reproduced in numerical simulations (see Refs. [103, 19]). While the exact shape of the zero-crossing arc depends on the details of the model (such as $\varphi_{\mathbf{r}}$), we observe that the movement of t_{zc} qualitatively matches the theoretical prediction (Figure 6.4F).

We can calculate an approximate critical radius for which we are observing shell formation. Assuming that the gradient field induced by the NV electron follows the dipole-dipole form $B = 2P\frac{\mu_0}{4\pi}\frac{\hbar\gamma_C\gamma_e}{r^3}(3\cos^2\theta - 1)$ where P is the electron spin polarization ($\approx 10\%$), and considering the specific experimental parameters for the dataset highlighted in purple ($\Omega \approx 50$ kHz, $t_{acq} = 51$ μs, $\theta = 0.94\pi$), we find the critical radius $r_c \approx 2.7$ nm$\cdot\sqrt[3]{|3\cos^2\theta - 1|}$ encompassing $\approx$150 spins assuming a spin density of $\approx$ 1 ppm ^{13}C. There is an angular dependence on the potential when considering the system in three dimensions which ought to appear both in Figure 6.4D and therefore in the calculation of r_c. For simplicity, we ignore the angular dependence in Figure 6.4D and note that it reduces to a simple multiplicative factor in the calculation of r_c; further detail of this calculation and the simplifications made to perform this estimate are presented (again) in the SI Section D of Ref. [84]. This calculation confirms the observation that began this endeavor: that adjusting the kick-angle θ close to π, we can modify the effective on-site potential and thus the critical radius r_c, allowing us to tune the shell size from tens (≈ 50) up to mesoscopic numbers ($\gtrsim 300$) of spins [156].

We note some brief housekeeping details for full transparency. The astute reader will notice that electron spin polarization used for the estimation of r_c ($\approx 10\%$) is too high for experiments performed at room temperature. Indeed, this is because the experiments performed in this "Hamiltonian Engineering" section are conducted on the cryogenic field-shuttling apparatus described in Chapter 2. All experiments are performed at 9.4 T and 100 K with hyperpolarization of $\sim$ 90 s. The shuttling time of this apparatus is likewise longer than that used in Section 6.1. Indeed, this is the primary reason that the cryogenic field-cycling apparatus is not used for "State Engineering" experiments — the shuttling time is so long that the fragile states created by State Engineering have been subject to too much spin diffusion such that the domain boundaries have melted before observations. As a stark comparison between the two experiments, one can see the difference in total signal in similar zero-crossing experiments generated by "State Engineering" (orange) and "Hamiltonian Engineering" in green in Figure 6.6. Spin texture created by "State Engineering" starts from a regime of low net polarization (Figure 6.2A) and sign inversion occurs because of electronic dissipation. On the other hand, "Hamiltonian Engineering" starts with large net polarization, and sign inversion occurs on account of thermalization into the imposed potential. As a result, the measured signal and the magnitude of the zero-crossing drop in

the "Hamiltonian Engineering" method are over one order of magnitude larger than those of "State Engineering".

This is not to say that electronic dissipation does not occur under the near-π drive of "Hamiltonian Engineering" experiments. Indeed, when considering Figure 6.4D, dissipation from the NV center certainly acts to relax nearby ^{13}C spins that are positively polarized. This contributes to a more rapid overtake of the positive polarization by the negative polarization (in regime IV) but we note that this dissipation is not necessary to form the zero-crossing.

Another interesting question is: if the "State Engineering" experiments cannot be performed on the cryogenic field-cycling experiments, could the "Hamiltonian Engineering" experiments be performed on the room temperature field-cycling apparatus? Furthermore — is the ability to engineer the potential unique to the cryogenic field-cycling apparatus' experimental conditions? Experimental data from the room-temperature field-cycling apparatus demonstrated the formation of this zero-crossing with near-π train pulsed spinlocking experiments before the conception of this publication as well as in various miscellaneous experiments since. At the time of this work, however, the ability to generate this type of data on the room-temperature instrument proved challenging; likely due to effects from sample orientation and temperature, as will be discussed in Sections 6.4 and 6.5.

6.3 Interrupted Driving

When we first encountered the zero-crossing through the method of "Hamiltonian Engineering", the data was strange and surprising. When considered objectively, the data indicates that a high amount of signal on the $\hat{\mathbf{x}}/\hat{\mathbf{y}}$ plane rapidly disappears over a few seconds (though not so rapidly that it could be due to arcing of the probe) and then reappears coherently to nearly the same height that would have occurred should the system have undergone typical relaxation. While phase data indicated that the polarization direction appeared to change from $\hat{\mathbf{x}}$ to $-\hat{\mathbf{x}}$, the method in which this polarization change occurred was not yet established. In this section, we present experiments probing the $\hat{\mathbf{z}}$ component of the spin vector at various time points t along experimental traces similar to those of Figure 6.4B. This allows us to examine whether the observed zero-crossings in Figure 6.4 are trivially the result of the spin vector tilting towards the $\hat{\mathbf{z}}$ axis, where the spins become unobservable.

The pulse schematic describing the sequence that we perform is in Figure 6.7A. The spins are subject to the same near-π pulsed spinlocking drive as before, but it is interrupted at time t=t_c with $\pi/2$ pulses applied in either the $\hat{\mathbf{x}}$ direction or the $\hat{\mathbf{y}}$ direction. If the net magnetization vector had become unobservable on the $\hat{\mathbf{y}}/\hat{\mathbf{z}}$ or $\hat{\mathbf{x}}/\hat{\mathbf{z}}$ planes, these $\pi/2$ interrupt pulses would return them to the visible $\hat{\mathbf{x}}/\hat{\mathbf{y}}$ plane at t_c. Setting $t_c = t_{zc}$, we can probe the $\hat{\mathbf{z}}$ component exactly at the zero-crossing point; or, by varying t_c, we can track the $\hat{\mathbf{z}}$ component throughout the various regimes of the "Hamiltonian Engineering" experiment.

As is apparent in Figure 6.7B(i) and C(i), no significant $\hat{\mathbf{z}}$ signal was observed. The small residual signal observed in Figure 6.7C(i), where the interrupt pulse is in the $\hat{\mathbf{y}}$ direction is attributed to a build-up of pulse imperfections, and specifically the frequency offset of

the pulses employed in these experiments. Furthermore, varying t_c, as in Figure 6.7B(ii) and C(ii) demonstrate negligible change in $\hat{\mathbf{z}}$ amplitude with t. This data rules out the explanation that the polarization spin vector is simply tilting through the $\hat{\mathbf{z}}$ axis, and in that manner, supports the explanation of the zero-crossing being caused by thermalization of the spins under the electron gradient induced potential.

6.4 Orientation Dependence

We show data examining the effect of changing the diamond sample orientation in Figure 6.8. We compare two slightly different sample orientations, where the NV center families have different directions relative to B_0. This is evident based on the DNP-measured EPR spectra of the NV centers in both cases (Figure 6.8A-B), where the first orientation appears to have two broad peaks, while the second has a third peak with shoulders shifted to higher frequencies. We note that the ideal EPR shape—with respect to hyperpolarization—is similar to that of Ref. [145], where a single peak is visible. This single peak comes from the alignment of all NV center families such that they have an equi-angle relationship to B_0.

The presence of multiple peaks in these EPR spectra indicates that the sample is not ideally aligned with respect to hyperpolarization; there are multiple groups of NV families that have slightly different relationships to the B_0 field. We note that this lack of alignment prompts the discussion of the goniometer advancement in Chapter 2. However, upon comparing the two DNP-measured EPR spectra in Figure 6.8, one will notice that these are not markedly dissimilar; especially when comparing the shape of the two broad peaks to the ideal alignment of a single peak.

When we examine the 2D zero-crossing plots of Figure 6.8A(iii) and B(iii) we find qualitatively identical development of spin-shell texture. Notably though, the S vs time datasets in Figure 6.8A(ii) and B(ii) appear quite different. In A(ii) the initial decrease followed by a flattening before the zero-crossing appears (as described in Figure 6.4B) does not appear; the zero-crossing is formed very near $t = 0$. In B(ii) the initial decrease *does* appear and in fact manifests as a local minimum, with S rising slightly before forming the zero-crossing. This small change in orientation, therefore, leads to a significant change in zero-crossing appearance. We attribute the minimum to the presence of multiple NV center families which, due to orientation with respect to the B_0 field, create the required zero-crossing condition at slightly different pulse lengths.

While performing this work, any changes made to the probe or experimental apparatus seemed to suppress the zero-crossing. It would disappear for months, seemingly without reason, despite attempts to alter experimental parameters to find the zero-crossing behavior again. Nearing the end of completion of this work, we noticed that the appearance of a zero-crossing seemed to coincide with this particular form of EPR lineshape that was "misaligned" with respect to hyperpolarization. Thus, the careful alignment of the diamond sample that we were painstakingly performing would, in fact, result in the elimination of the effect we wanted to observe. We believe that a small change in the sample mounting of the room-

temperature apparatus (which was re-mounted less frequently than that of the cryogenic field-cycling instrument) during the time of this work resulted in the inability to see the zero-crossing experimentally.

We intuit that the small change in the sample orientation would effectively change the on-site potential strength. Consider Figure 6.3C where the potential is depicted. A simple scalar increase or decrease to the potential could make the on-site potential entirely positive or entirely negative within the range of observable spins. While the physics underlying Figure 6.4 and the "Hamiltonian Engineering" method can be considered independent of the exact sample orientation, the appearance of the zero-crossing in a manner that is observable by our experimental conditions *is* strongly dependent on the sample orientation.

6.5 Temperature Dependence

Another consideration which may have affected the presence of the zero-crossing on the room temperature instrument compared to the cryogenic instrument is, in fact, the changing temperature. A decrease in temperature has previously been shown to have a strong effect on rates of electronic relaxation T_{1e} (of both NV and P1 centers). We note that Refs. [186, 94] found that for samples with comparable NV center densities as the one employed here, T_{1e} increases sharply near 100 K and can exceed $T_{1e} > 1$ s under these conditions. Earlier in this dissertation, low temperatures of 100 K were shown to increase the T_{1C} of the ^{13}C nuclear spins in the diamond lattice (Chapter 3).

Figure Figure 6.9 presents experiments conducted at six representative temperatures. To ensure consistency, we maintain the same nuclear Rabi frequency for all experiments (Figure 6.9B). Results indicate that the time at which the zero-crossing occurs (t_{zc}) increases as the temperature decreases. This can be seen as a direct reflection of the increase in the NV center T_{1e}, which in turn decreases the strength of the dissipation acting on the ^{13}C nuclear spins. While this dissipation is not necessary to form or read out the "Hamiltonian Engineered" shells, strong dissipation at high temperatures can further constrain the conditions in which a zero-crossing is formed experimentally.

6.6 Experimental Sequence Dependence

Hyperpolarization Time

Earlier in this dissertation, we briefly investigated the results of increasing hyperpolarization time on spin temperature (Chapter 4). We again turn to this investigation, now focusing on the relationship between the zero-crossing and the amount of hyperpolarization injected into the ^{13}C nuclear spins. Figure 6.10 depicts these experiments, where the amount of time τ_+ for which hyperpolarization is performed is varied. These experiments are performed under conditions in which the zero-crossing is reliably formed and relatively centered with respect to the time axis so that motion caused by the change in hyperpolarization will be

evident. These conditions include a pulse train of nominally $\theta = 160^\circ = 0.89\pi$ and a system temperature of 115 K.

The amplitude signal obtained in these experiments (Figure 6.10) shows the expected zero-crossing and subsequent phase inversion. As the hyperpolarization time τ_+ increases, the zero-crossing time shifts slightly leftward. One would expect that decreasing spin temperature through hyperpolarization would lead to a shift similar to that of the cooling experiment performed previously (Figure 6.9). Interestingly, the zero crossing time t_{zc} shifts in the opposite direction.

In Section 6.5, we indicate that the large shift in the t_{zc} with temperature was a reflection of the increased NV center T_{1e} and thus decreased action as a dissipator. Here, changing hyperpolarization time has no effect on the NV center's action as a dissipator, only changing the initial amount of polarization of the ^{13}C system. Adding polarization to the ^{13}C spins, in a simplistic picture, decreases the amount of time it takes between stages (I) and (II) in Figure 6.4D. However, with the same $\mathcal{H}_{eff}$, this change is not very large, which is demonstrated by the relatively small shift in t_{zc} even over large hyperpolarization gains. (We note that the apparent fuzziness in the grey data sets where τ_+ is small is due to low SNR stemming from very low hyperpolarization). The persistence of the zero-crossing, even through very weakly hyperpolarized initial states, supports the fact that spin texture engineered via "Hamiltonian Engineering" is qualitatively independent of the initial state of nuclear spins.

Rabi Frequency

Several factors ought to control the zero-crossing behavior more strongly than the hyperpolarization as they affect the effective Hamiltonian and thus r_c. Among these is the nuclear Rabi frequency, Ω_{eff}. Since the effective flip angle θ is determined as an interplay between the electronic gradient field and the strength of the $\hat{\mathbf{x}}$ Rabi field, changing Ω_{eff} would directly affect r_c. We anticipate from theory that decreasing Ω_{eff} should result in a leftward shift in t_{zc}. Although only one true zero-crossing is shown at the fastest duty cycle of 42 μs, the other signal traces indicate the expected leftward shift. These traces all show the characteristic shape which occurs prior to the zero-crossing. We refer the reader to the previous section on orientation (Section 6.4) as an explanation for why the zero-crossing first occurs at $t \approx 35$ s as opposed to at earlier times t.

In Figure 6.11, we manipulate Ω_{eff} by modifying the duty cycle of the drive, as schematically denoted in the inset. This is atypical when considering typical NMR schemes of varying the Rabi frequency which alter the pulse power. In conventional NMR, the Rabi frequency is directly related to the pulses and the frequency at which the pulses are driven. In this driving scheme and under Floquet conventions, however, we refer to the Rabi frequency as the driving frequency of the whole sequence; that is to say, the gaps between the pulses change the length of time over which an entire Floquet cycle occurs. Increasing these gaps is an effective way to alter the duty cycle and thus Rabi frequency with minimal other effects. If, for example, we changed the pulse power (the conventional way to affect the Rabi frequency in NMR), this would increase the pulse length needed to perform the same near-π

angle which would *also* increase the duty cycle. We note that these experiments were performed and exhibited a similar trend as simply changing duty cycle. However, the longer pulse lengths led to increased arcing in the data sets; thus, they are not presented here. We note that arcing is minimally present in data presented in Figure 6.11, represented as sharp discontinuities between $40 < t < 50$ s in the fastest duty cycle datasets.

Transmitter Offset Frequency

Similarly, changing the pulse frequency offset at fixed Ω should result in a shift of the ^{13}C spin layer that has a flip angle matching π, thereby changing r_c and t_{zc}. In the rotating frame of the periodic drive, changing offset refers to applying a global $\hat{\mathbf{z}}$-oriented field to the ^{13}C nuclei. Since this field can either enhance or counteract the local field from the NV center gradient, the precise magnitude of the shift to r_c is challenging to predict.

However, qualitative trends in these shifts are easily observable. Figure 6.12A demonstrates the effect of changing the offset at a fixed length t_p of the applied pulses. The zero-crossing is readily apparent over a range of offsets, although t_{zc} appears to move. For large offsets, the zero-crossing no longer appears within the 70 s experiment time. This is consistent with effectively shifting the position of the ^{13}C slice corresponding to r_c. In Figure 6.12B, the plot of t_{zc} vs offset reveals a near symmetrical shape, centered around an offset of ≈ 4.7 kHz. We note that later experiments, presented in Chapter 7, reveal that this "offset" in fact corresponds to approximately on-resonant pulses for bulk ^{13}C spins.

We note that, on occasion, the zero-crossing behavior switched between occurring before $\theta = \pi$ and after (compare Figure 6.4 where the zero-crossing behavior occurs after $\theta = \pi$ and Figure 6.8 where the zero-crossing behavior occurs before $\theta = \pi$). We attribute this switch to a lack of calibration of transmitter offset during early experiments; this lack of calibration would result in the $\theta = \pi$ condition being met for bulk spins at a different pulse length than anticipated from our calculations of nominal pulse width. We find that regardless of exact features, the resonance offset, as anticipated, is capable of shifting r_c and the physics underlying the formation and thermalization of the spin shell remains unchanged.

6.7 Theoretical Results

With a large number of variables affecting the formation of the spin texture and the manifestation of zero-crossings, collaboration with a theory group to perform simulations and model the interplay between the NV center and ^{13}C spins was imperative to understand the system. These simulations, both quantum in one dimension and classical in three dimensions, act to confirm the experimental data and identify parameters which act to tune the zero-crossing behavior, including the transmitter offset frequency and duty cycle.

The quantum simulations presented here use Local-Information Time Evolution (LITE) [103, 19], a recently developed algorithm suited to investigate diffusive and dissipative quantum dynamics. While a simplified one-dimensional toy-model Hamiltonian must be used due to

numerical tractability constraints, all relevant features of $\mathcal{H}_{eff}$ are captured. LITE is designed to investigate the out-of-equilibrium dynamics of quantum systems, including open systems governed by the Lindblad equation. Its adaptive system size allows effective simulation of infinite systems. All simulations using LITE and corresponding theoretical descriptions are performed by Dr. C. Artiaco and Dr. C. Fleckenstein under the supervision of Dr. M. Bukov.

The one-dimensional toy-models that are used for Hyperpolarization Injection and Hamiltonian Engineering, respectively, are as follows:

$$\mathcal{H}_{\pi/2} = \sum_r J_r \left(\frac{3}{2}(I_{ry} I_{(r+a)y} + I_{rz} I_{(r+a)z}) - \mathbf{I}_r \cdot \mathbf{I}_{r+a} \right), \tag{6.2}$$

$$\mathcal{H}_{\pi} = \sum_r J_r (3 I_{rz} I_{(r+a)z} - \mathbf{I}_r \cdot \mathbf{I}_{r+a}) + \varphi_r I_{rx}. \tag{6.3}$$

The subscripts indicate the corresponding partner Hamiltonian in the actual system: $\pi/2$ refers to the system kicked with $\theta = \pi/2$; likewise, subscript π refers to a kick angle $\theta \approx \pi$. We note that $r = 0$ corresponds to the location of the NV center with r being the distance from the NV center, a is the lattice constant and $\delta\theta$ is the deviation in the kick angle from π. In the "Hamiltonian Engineered" system, the on-site potential follows $\varphi_r \sim \frac{1}{r^3} - \delta\theta$. For the simulations in Figure 6.13 $a = 0.2/\sqrt[3]{\pi}$, $\delta\theta = 0.05\pi$, and $J_0 = -0.025$ are used to emulate the real NV system dynamics. While these models may appear simplistic compared to the actual experimental system, as they lack the complexity of higher dimensions and long-range spin-spin couplings, they capture the essential physics of diffusion and dissipation, since they obey the same conservation laws as their three-dimensional counterparts.

Figure Figure 6.13A(i) shows simulations corresponding to "Hyperpolarization Injected" spin-shell experiments. Time is represented on the horizontal axis in units of inverse median coupling (J^{-1}) while the vertical axis represents the distance from the NV. The color bar shows the local $\hat{\mathbf{x}}$-polarization I_{rx}. We observe that the dynamics over time demonstrate a rapid "melting" of spin texture. While the effect of dissipation is not immediately evident from this plot, an in-depth description of the effect of dissipation and simulations when dissipation is not active is found in the SI of Ref. [84]. To summarize these results, in the absence of dissipation total $\hat{\mathbf{x}}$ polarization is (quasi-)conserved and thus will appear approximately constant throughout the simulation.

In contrast, Figure 6.13B shows simulations of the "Hamiltonian Engineered" spin shells where polarization is initially entirely positive. Over time, by virtue of energy diffusion, the spins prethermalize to a polarization gradient under the NV-induced potential. The total polarization inverts as the majority of spins attain negative polarization. Since the on-site potential is governed by $\mathcal{H}_{eff}$, the domain boundary r_c separating the positive and negative polarization regions is stable and unaffected by the initial state.

In the plots of net polarization (Figure 6.13A(ii),B(ii)), corresponding zero-crossings can be observed. They are in qualitative agreement with our experiments, especially with respect to the signal magnitude difference between the "State Engineered" and "Hamiltonian Engi-

neered" methods; the zero-crossing in Figure 6.13A(ii) only spans 2 orders of magnitude compared to the nearly 5 orders of magnitude spanned by the zero-crossing in Figure 6.13B(ii). This zero-crossing feature also arises in the absence of dissipation for the "Hamiltonian Engineered" system (see the SI Figure S28 of Ref. [84]); dissipation in this case only serves to extinguish polarization at distances close to the NV, accelerating the inevitable polarization inversion.

Additional classical simulations are performed based on a three-dimensional long-range model comprising $\approx 10^3$ dipolar-interacting spins on a diamond lattice. These simulations and corresponding theory are performed by P. Schindler under the supervision of Dr. M. Bukov. Performing a classical simulation allows the study of considerably larger system sizes of hundreds of spins, enabling the study of 3D systems with a finite linear extent. At the same time, however, a classical simulation comes at the expense of neglecting all quantum correlations. In addition, the number of spins in a three-dimensional system scales cubically: $L \propto r^3$, where L is the number of spins and r is the linear dimension. Thus, studying quasi infinite systems, i.e., systems with a linear extension far exceeding the support of the initial state, as is needed to model an open system, is beyond the scope of this simulation. Diffusion, therefore, cannot be included in the classical model, restricting the three-dimensional simulations to the "Hamiltonian Engineered" spin texture which does not need dissipation to form.

The angle dependence of the NV gradient field is able to be included in these 3D simulations. The initial state is fully polarized near the NV center and unpolarized at far distances r. As the simulation progresses in time, the polarization reorganizes and the energy diffuses to match the on-site potential. Figure 6.13C, D show the result of these simulations where Figure 6.13C is a vertical slice of Figure 6.13D.

6.8 Discussion

The manipulation and control over the ^{13}C spin system that we demonstrate in this chapter is of interest to a variety of fields. For example, creating on-demand magnetic domain wall states within quantum simulators can potentially be useful for investigations of spin dynamics [113, 194, 162] and one can envision generating a potential that yields a stable spin texture at negative temperatures [35]. This may enable applications in quantum memories [100, 53] and solid-state systems at low temperatures, such as phosphorus-in-silicon systems [118, 131], where spin texturing within nuclear spins (e.g., silicon-29) around phosphorus donors could create a memory resource that can be used in conjunction with the donor electronic qubit, similar to Refs. [138, 133, 32]. While our experiments have been performed on nuclear spins, the theoretical results apply to any spin system, e.g., electronic spins, opening possible applications in spintronics [96, 182] through nanoscale electronic spin bath texturing [154, 55, 115, 78, 114].

We find this investigation into spin texture to be particularly compelling in the context of this dissertation. At first glance, spin lifetimes are shortened through the zero-crossing

behavior with the rapid collapse of net polarization. Upon further consideration, one realizes that these spin lifetimes are largely unaffected when comparing the coherence time to the traditional decay under normal spinlock conditions (i.e., comparing the orange trace to the dashed trace of point (a) for "State Engineering" in Figure 6.1 or comparing the traces across the three panels B-D for "Hamiltonian Engineering" in Figure 6.5) the magnitude of the end of the experiment at $t = 60$ s is largely unaffected.

The real insights in this chapter into nuclear spin lifetime, then, come from the region of spins around the domain boundary in the "Hamiltonian Engineered" experiments. Conventional arguments indicate that these spins should relax quickly from the homogenizing action of diffusion; this chapter demonstrates that protection arising from the effective Hamiltonian $\mathcal{H}_{eff}$ provides another method for extending nuclear spin lifetimes.

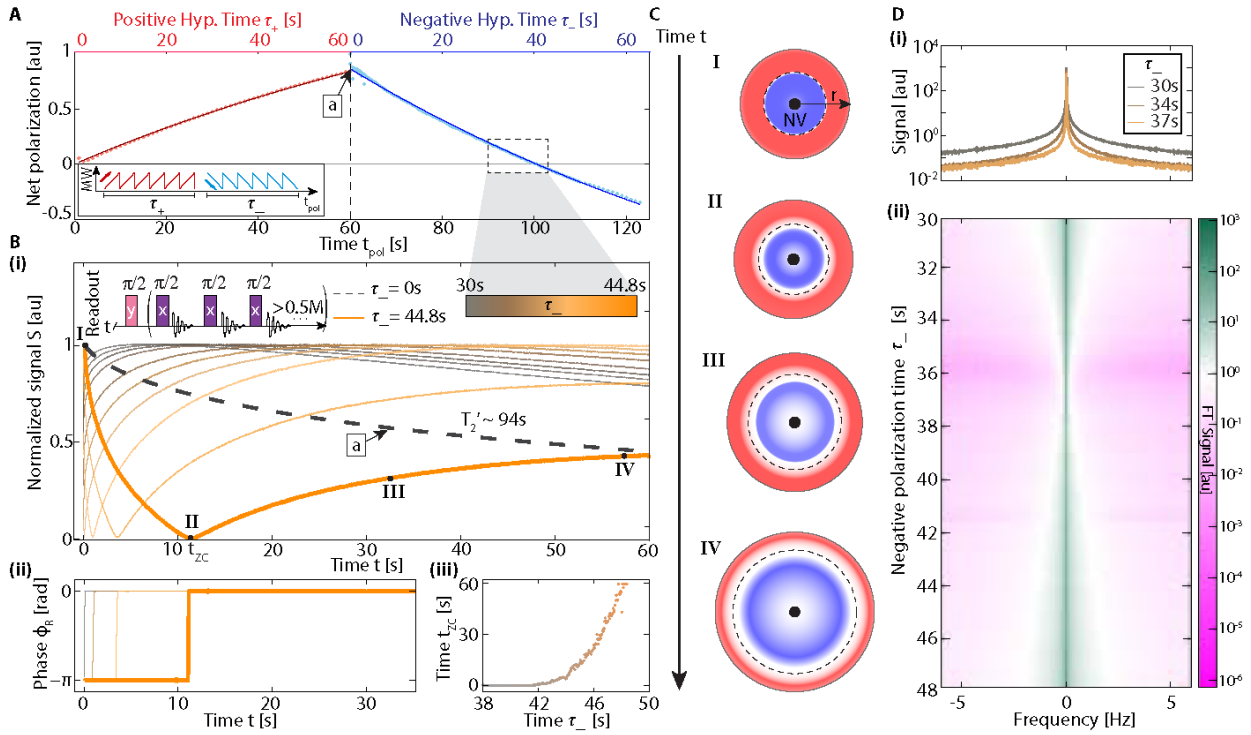


Figure 6.1 **Spin textures created via hyperpolarization injection.** (A) Net ^{13}C spin polarization under positive (τ_+, red points), followed by negative (τ_-, blue points) hyperpolarization injection at room temperature. Solid lines represent a biexponential fit. Boxed outline centered on $t_{pol} \approx 100$ s highlights region of ≈0 net polarization for closer examination. (B) Normalized spin-lock decays under periodic drive with $\theta \approx \pi/2$ (inset), showing (i) signal S and (ii) rotating-frame phase ϕ_R. The spinlock decay corresponding to $\tau_+ = 60$ s, $\tau_- = 0$ s (point a in A) is represented by a dashed black line. Data for different τ_- values from the inset in (A) exhibit a sharp zero-crossing at t=t_{zc} and associated phase inversion (see ii). (iii) Plot of zero-crossing t_{zc} with increasing τ_-. (C) Schematic representation of polarization with increasing experiment progression time t. Representative points (I-IV) are marked in (B) for dataset τ_-=44.8 s. Electron-driven dissipation decreases polarization (white) around r=0. Growing texture size and an increasing white region at the shell boundaries indicate spin diffusion; dashed line represents polarization domain wall boundary. (D) (i) Fourier transformed ^{13}C NMR spectrum of full S vs time data for τ_-=30, 34, and 37 s. (ii) FT data for varying τ_- is plotted on a logarithmic scale comprising 91 τ_- slices, separated by 0.2 s with a $>10^9$ variation in intensity.

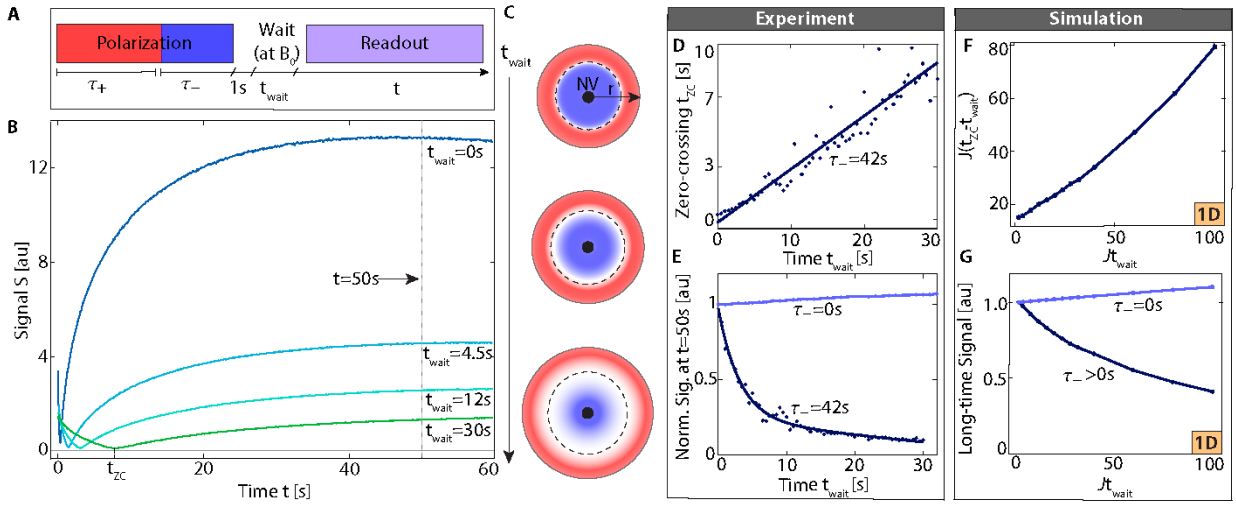


Figure 6.2 **Melting of initial state spin texture due to spin diffusion.** (A) Experiment schematic shows how hyperpolarization injection experiment is modified. After successive τ_+, τ_- spin injection, a waiting period t_{wait} at high field is introduced prior to the application of the periodic spinlock drive. (B) Representative signal traces showing changes in decay profiles with variable t_{wait} for texture generated with $\tau_+ = 60$ s and $\tau_- = 42$ s. The decrease in signal amplitude between $t_{wait} = 0$ s and $t_{wait} = 30$ s demonstrates the susceptibility of state-engineered spin texture to spin-diffusion-mediated relaxation. (C) Schematic representation of the melting of spin texture during t_{wait} due to spin diffusion at the boundary between polarization layers. The dashed line indicates the domain wall boundary. (D) Points show the movement of the zero-crossing t_{zc} position with t_{wait} for data in (B). The solid line is a linear fit. (E) Signal intensity at $t = 50$ s for data in (B), normalized to its value corresponding to the $t_{wait} = 0$ s case. Loss of spin texture due to diffusion manifests as a decrease in signal. Solid line is a biexponential fit. The light blue line corresponds to equivalent data where the initial state lacks spin texture ($\tau_+ = 60$ s, $\tau_- = 0$ s). (F–G) Simulations corresponding to (D–E) showing zero-crossing times and $|I_x|$ extracted from numerical time evolution in a one-dimensional short-range model using a similar shell-like initial state. Simulations show qualitative agreement with experimental results.

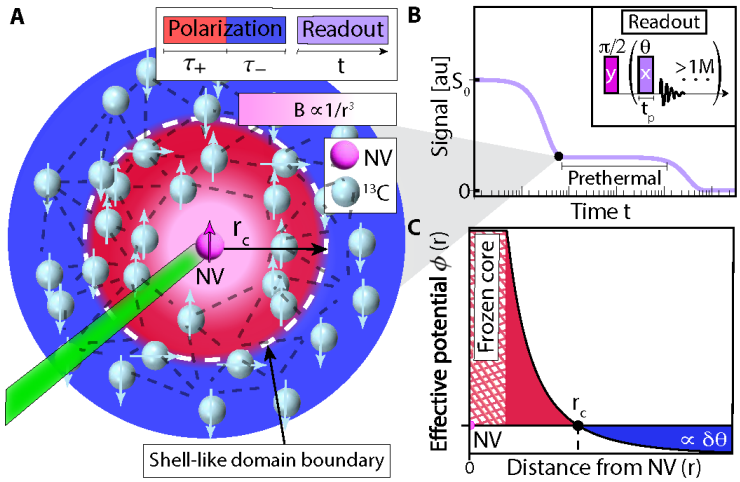


Figure 6.3 **NV-mediated gradient potential to form stable "shell-like" textures.** (A) Controllable "shell-like" spin texture of positive and negative polarization (shaded red and blue, respectively) is generated in a nanoscale ensemble of ^{13}C nuclear spins surrounding a central NV electron (manipulated by an external laser, shown in green). The domains are separated by the critical radius r_c at the domain boundary (dashed white line). The texture encompasses ~ 100 spins within the critical radius and remains stable for minutes. The optically pumped electron serves both to hyperpolarize the ^{13}C spins and produce a nanoscale magnetic field gradient B (shaded light pink), encoding spatial information. (B) Experimental schematic showing prethermalization caused by periodic driving at high magnetic field, with a train of spinlocking θ-pulses of length t_p. $\hat{\mathbf{x}}$-$\hat{\mathbf{y}}$ spin polarization is interrogated in windows between the pulses for total readout times $t > 60$ s (> 0.5 M pulses). (C) A spatially-varying potential $\varphi_{\mathbf{r}}$ is created upon driving with $\theta \approx \pi$ in the presence of the NV gradient.

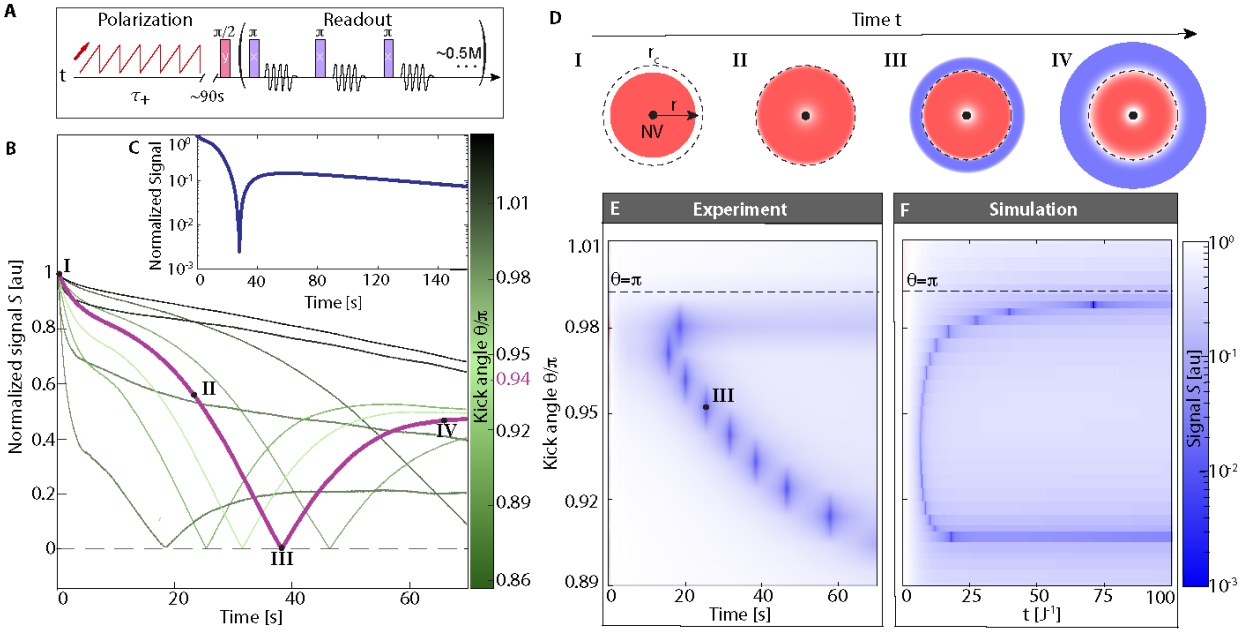


Figure 6.4 **Formation of zero-crossing behavior from Hamiltonian Engineered drives.** (A) Experiment schematic demonstrating that spins are hyperpolarized for $\tau_+ = 90$ s and subject to a spinlocking train with $\theta \approx \pi$. (B) The measured signal S undergoes sharp zero-crossing at t_{zc} and associated sign inversion. Colored lines show variation with θ (see color bar). Each trace has ≈0.5 M points. Dark purple trace highlights representative data at $\theta = 0.94\pi$ for clarity. (C) Analogous signal to the purple trace in (B). The signal is plotted on a logarithmic scale and extends for t>150 s. (D) Schematic representation of the formed spin texture for different regimes of the purple trace in B (marked I-IV). These stages represent progressive thermalization to an effective Hamiltonian $\mathcal{H}_{eff}$ bearing spatial texture arising from the NV-imposed gradient. Dashed black line indicates the domain boundary at r_c. Spin texture remains robust against spin diffusion, although dissipation from the NV center continues to act. (E–F) Movement of the zero-crossing with θ near π represented as a 2D color plot. (E) Logarithmic scale visualization of data in B is plotted in horizontal slices. Zero-crossing appears as an abrupt decrease in signal (colored blue). $\theta = \pi$ slice for bulk ^{13}C nuclei corresponds to a rapid signal decay. Point III corresponding to the zero-crossing in B is marked. (F) Numerical simulations performed with LITE for the simplified short-range model match the qualitative behavior of the experimental data.

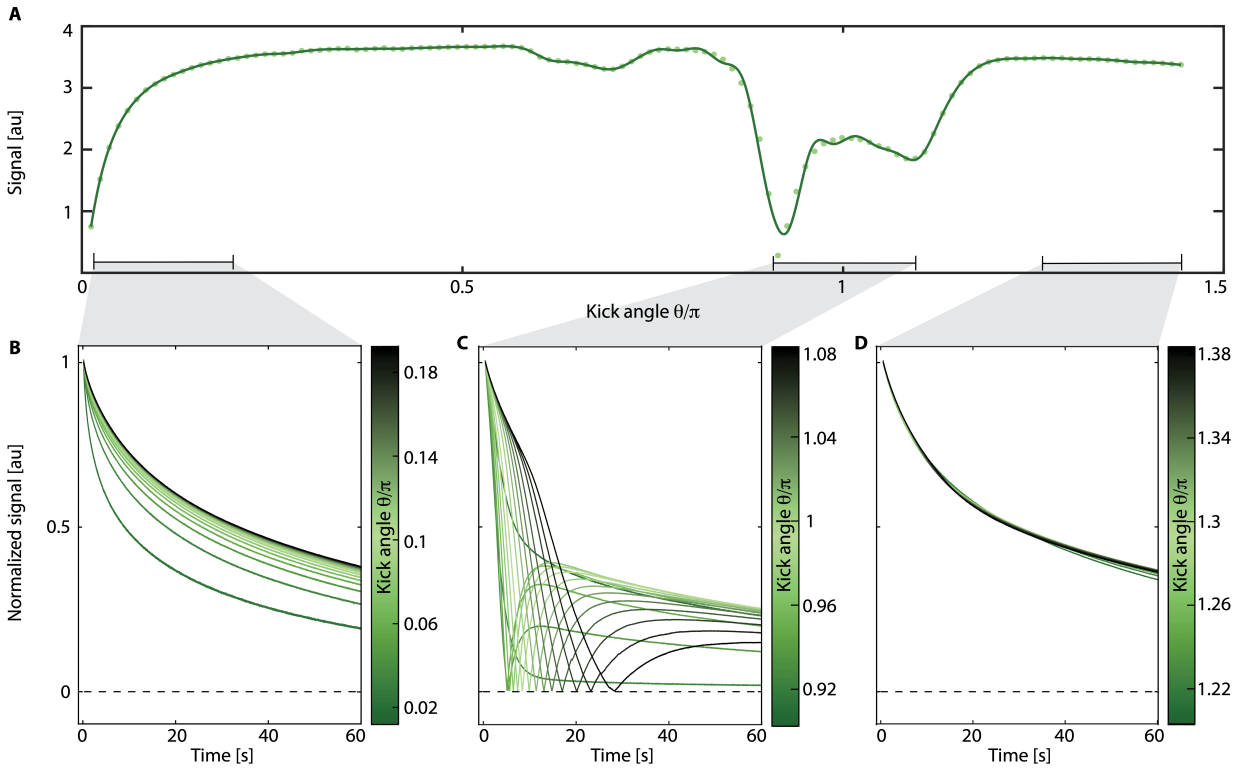


Figure 6.5 **Data for a wide range of spinlocking angles.** (A) Integrated signal S_{int} over the first 60 s of experiment time as a function of pulse train flip angle $0 < \theta < 1.5\pi$. Representative regions centered at θ=0.1π, π, and 1.3π, respectively, are indicated. (B-D) Decay profiles for the shaded regions in (A) are shown, with pulse flip angle values indicated by the color bar. Decay curves are featureless for far away pulse angles on either side of $\theta = \pi$. Near $\theta = \pi$, however, there is a significant change in the signal profile resulting in zero-crossings which we associate with the formation of shell-like spin textures.

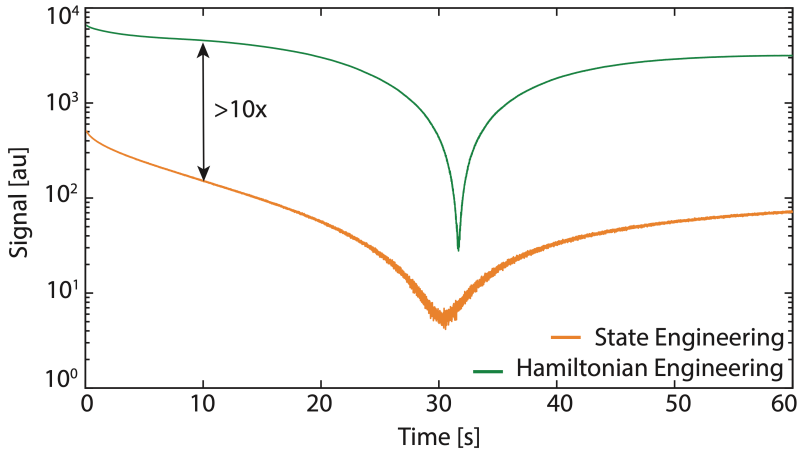


Figure 6.6 **Comparison of State and Hamiltonian Engineering signal magnitude.** Comparison of signal S for State Engineering and Hamiltonian Engineering data for comparable zero-crossing times $t_{zc} \approx 31$ s. Data is shown on a logarithmic scale for clarity. The measured signal is over an order of magnitude greater in the Hamiltonian Engineering method, due to formation of shells with high levels of net polarization.

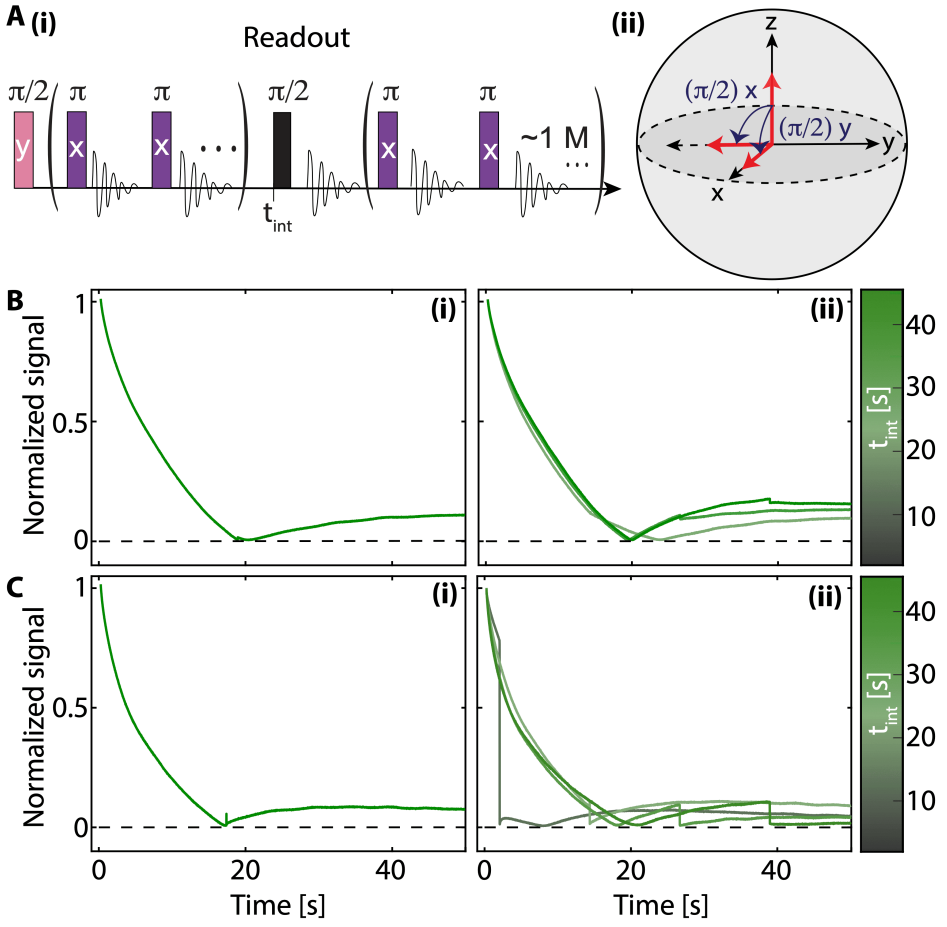


Figure 6.7 **"Interrupted" periodic driving experiments.** (A) i) Schematic of the experiment, consisting of a spinlock train interrupted by an orthogonal $\pi/2$ pulse in $\hat{\mathbf{x}}$ or $\hat{\mathbf{y}}$ at $t = t_{int}$ that reorganizes population from the $\hat{\mathbf{z}}$ axis to the $\hat{\mathbf{x}}/\hat{\mathbf{y}}$ plane. (ii) Bloch sphere representation indicating schematically how the interrupt sequence will reveal population along the $\hat{\mathbf{z}}$ axis. (B–C) i) Signal S vs time at t_{int}=t_{zc} for the case of $\pi/2|_x$ in (B) or $\pi/2|_y$ in (C) interrupt pulses. The measured amplitude in the $\hat{\mathbf{x}}/\hat{\mathbf{y}}$ plane does not significantly change. (B–C) ii) Signal S vs time profiles where $t_{int} \neq t_{zc}$. In (B), the $\pi/2|_x$ pulse caused minimal disruption to the signal decays. However, in (C) the $\pi/2|_y$ pulse reorganized the population of spins from the $\hat{\mathbf{x}}$ axis to the unobservable $\hat{\mathbf{z}}$ axis, causing an abrupt loss of signal.

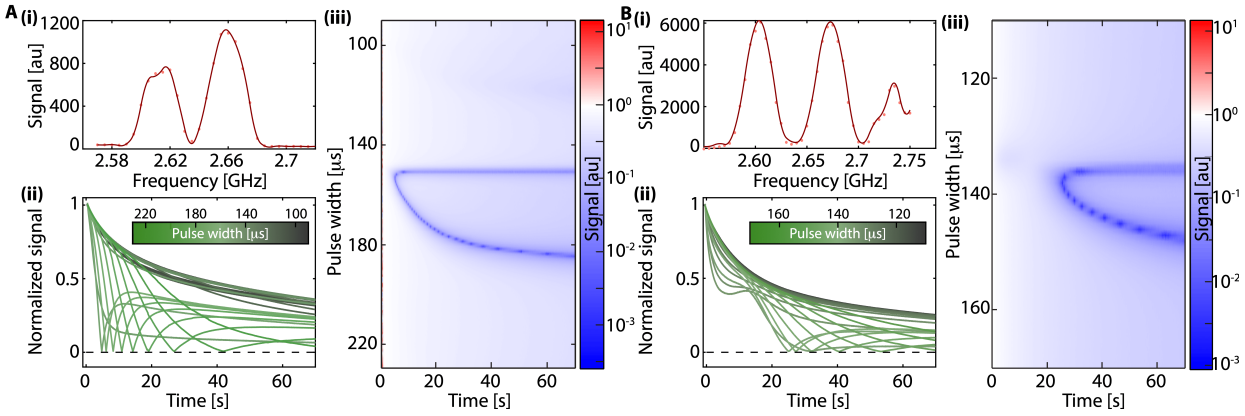


Figure 6.8 **Formation of "Hamiltonian Engineered" spin texture for two different sample orientations.** (A,B) i) Indirectly obtained EPR spectrum via ^{13}C DNP, produced by sweeping hyperpolarization MW chirps in narrow 25 MHz windows. The integrated signal of the resulting NMR decay curves is plotted as a function of the center frequency of the swept MWs. The solid line is for visualization purposes. (A-B) ii) Representative signal decays in the proximity of $\theta = \pi$ show zero-crossings. (A-B) iii) 2D color plots showing full data from (ii) as a function of pulse train pulse angle θ, highlighting the movement of the zero-crossings for the two orientations.

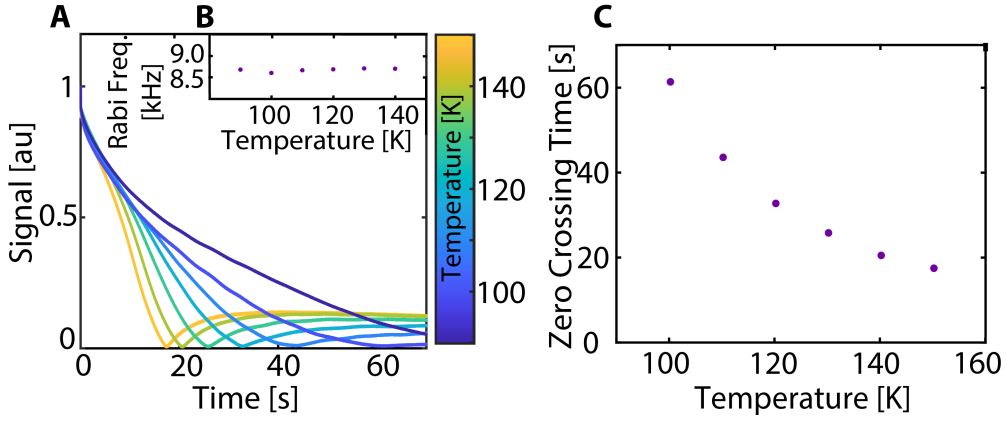


Figure 6.9 **Effect of temperature on "Hamiltonian Engineered" spin-shell profile.** (A–B) Spin-lock decays forming shells via near-π spinlock driving as they change with temperature (see color bar). Experiments are performed at a fixed flip angle and identical Rabi frequency. (C) Variation of zero-crossing time t_{zc} with temperature.

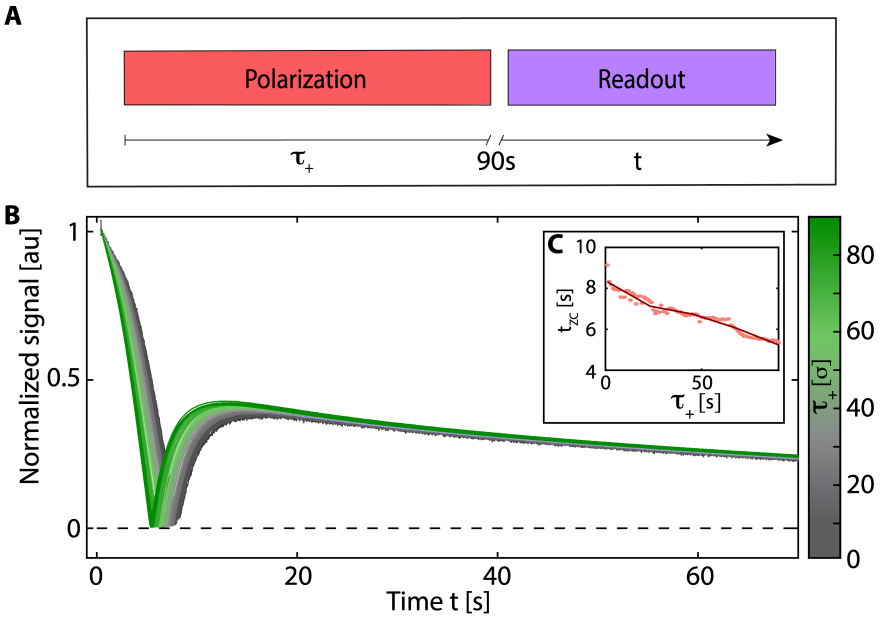


Figure 6.10 **Effect of hyperpolarization injection τ_+ on "Hamiltonian Engineered" spin-shell texture.** (A) Schematic of the experiment sequence, where injection time τ_+ is varied. Here, as with all "Hamiltonian Engineered" experiments, a shuttling time of t_s=90 s is performed (not to scale in this schematic). (B) Normalized signal decays for different values of τ_+, as indicated by the color bar. Spin shells are formed using a near-π pulse train of $\theta = 0.89\pi$. (C) Variation of zero-crossing time t_{zc} with τ_+. Solid line is a spline fit to aid in visualization of the trend.

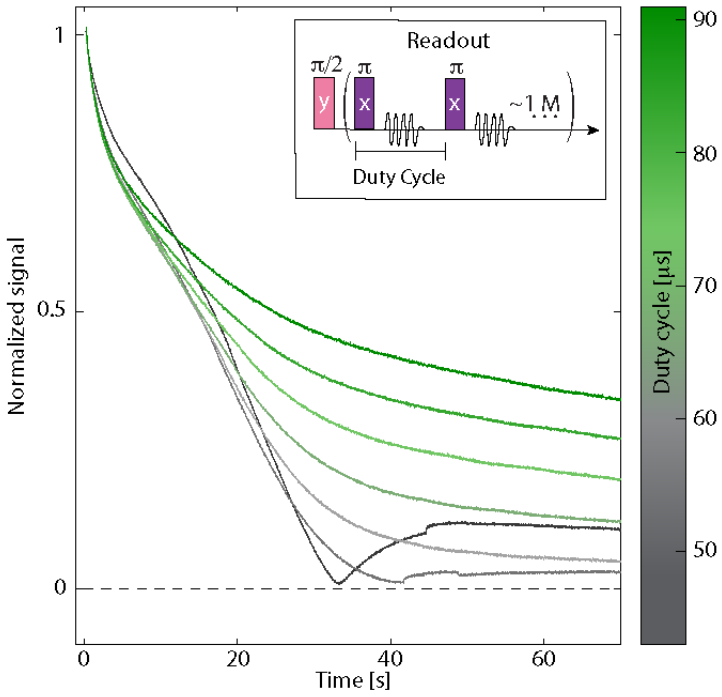


Figure 6.11 **Variation of "Hamiltonian Engineered" spin shell with pulse duty cycle.** Spinlock signal decay profiles for increasing duty cycle (see color bar) applied to the nuclear spins. The pulses of the drive are $\theta \approx \pi$, as is required for "Hamiltonian Engineered" shells. Control of the duty cycle while maintaining a fixed flip angle θ results in a linear increase of effective Rabi frequency of the drive Ω_{eff}. Inset shows pulse sequence schematic, with definition of the duty cycle being the total time between the start of one pulse and the next.

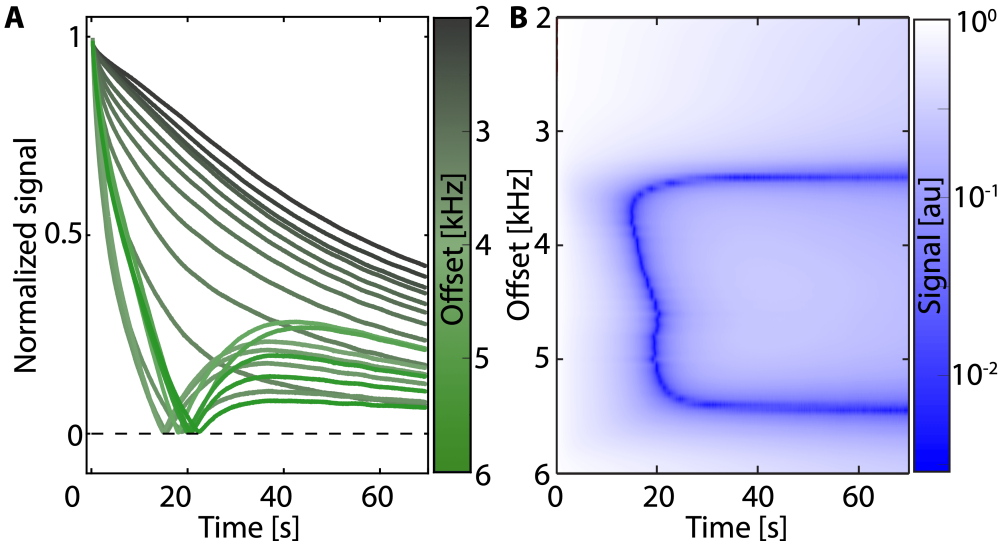


Figure 6.12 **Effect of frequency offset on "Hamiltonian Engineered" spin shell formation.** (A) Normalized spin-lock profiles of S vs t at different frequency offset values for the drive (see color bar). (B) Movement of zero-crossing t_{zc} with offset. The 2D color plot shows signal data from (A) plotted on a logarithmic scale as a function of offset. the zero-crossing appears as an abrupt decrease in signal (colored blue). There is a wide range of offsets ($\sim$2 kHz) for which a zero-crossing is observed.

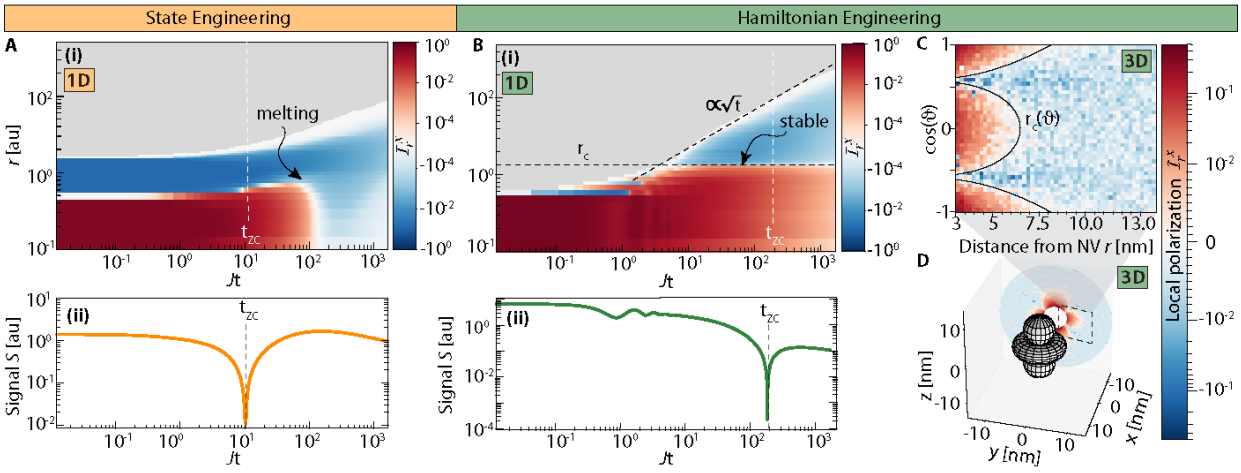


Figure 6.13 **Simulations of spin texture formation.** (A) 1D short-range simulation using the LITE algorithm. 11 spins are positively polarized close to the NV center at $r = 0$ followed by 18 negatively polarized spins. System extends in both directions, but only positive values are shown. Horizontal axis displays interrogation time t in J^{-1} units, vertical axis displays distance r from NV in arbitrary units (a.u.). (i) Polarization is shown at different sites as a function of time t (vertical slices). Initialized shells melt under diffusion. (ii) Integrated polarization over the spin ensemble, analogous to signal S measured in experimental data. Simulations reveal formation of a sharp zero-crossing, occurring at the instance of zero total net polarization. (B) 1D short-range simulation using the LITE algorithm for the "Hamiltonian Engineered" case. The initial state at t=0 contains 11 positively polarized spins within a background of spins in a fully mixed state. (i) Polarization shows that spin texture forms via thermalization. Late time behavior (dashed line) is characteristic of energy diffusion $\propto\sqrt{t}$. The shell critical radius r_c (horizontal dashed line) is stable throughout the experiment. (ii) Integrated ensemble polarization shows formation of zero-crossing. (C–D) 3D classical long-range simulation shows late-time dynamics forming spin-shells via "Hamiltonian Engineering". Dissipation is not considered and spins within the frozen core (white region in D) are not simulated.

Chapter 7

Transmitter Offset Engineering of Protected Spinlock Axis

Thus far, we have touched on a variety of experiments that alter the properties of relaxation behavior. This chapter, then, demonstrates what is arguably the longest extension in transverse lifetime yet seen in this dissertation, stemming from discoveries presented in nearly all previous chapters. In Chapter 2 we designed an instrument that was capable of performing cryogenic interrogation of pulsed spinlock lifetimes, then in Chapter 3 we discussed the effect of the electronic fluctuations that change strongly as a function of temperature. In an initial dataset collected as a function of temperature, there appeared to be a strong temperature dependence of lifetime. Upon further examination, however, this lifetime was actually a result of off resonant pulses which stemmed from a lack of calibration of the probe circuitry with temperature. This result, coupled with the strong effect of transmitter offset on the formation of the spin polarization barrier in Chapter 6, was a driving force for the investigation of the effect of transmitter offset on transverse nuclear spin lifetimes.

Previously, in Chapter 6, we have visited the concept of Floquet control in the context of the pulsed spinlocking sequence. In Floquet sequences, periodic kicks avert rapid heating and induce the system to enter a long-lived metastable state, enabling applications that exploit many-body couplings before the system ultimately thermalizes to infinite temperature [176, 25, 144, 164]. This description matches the pulsed spinlock sequence exactly, supporting our description of the experimental sequence with Floquet terminology.

A key focus of Floquet control is to develop strategies to extend prethermal lifetimes [56, 67, 200] and to understand the origins of heating and relaxation processes during the different stages of thermalization [89, 195, 119, 25, 29]. Long lifetimes boost sensitivity and resolution, making Floquet prethermal states a good candidate to explore for quantum sensing [165]. In addition, longer prethermal lifetimes and coherence times may extend the ability to detect transient signals that occur within unpredictable time windows. To these ends, the last section of this chapter will explore continuing work that develops the long transverse lifetimes explored here into sensors for AC magnetic fields. Here, we measure magnetic fields continuously for $\approx$10 minutes following our rapid hyperpolarization step. We will analyze the

sensitivity of our quantum sensor as a function of resonance offset and pulse angle, providing additional insights into the regimes where the sensor achieves optimal sensitivity.

Overall, in this chapter, we observe that transverse lifetimes can be significantly increased through tailored off-resonant excitation. We describe two methods in which this is done: first, in Section 7.3 we describe using the transmitter offset to place the protected axis along the magic angle with respect to the bulk ^{13}C spins, analogous to Lee-Goldberg decoupling. The second method, in Section 7.4, combines strongly off-resonant excitation (up to 5 kHz) with short angle pulses (nominally τ<10°), extending the $1/e$-lifetime to T_2'>800 s, a >533,000-fold increase over T_2^* under identical conditions. Remarkably, this extension is achieved with only a single (nominal) π rotation applied per T_2^* period, counterintuitive when considering that the Floquet framework through which we consider the pulsed spinlock typically requires averaging over many cycles.

In this chapter also, we finally address the form of the spinlock decay. As briefly remarked on in Chapter 5, these spinlock decays are not mono-exponential (except for certain circumstances). Here we utilize the high SNR from hyperpolarization and rapid data sampling enabled by the pulsed spinlock sequence to perform an analysis of the spinlock decay profiles via Laplace Inversion (LI) [179, 190]. Laplace Inversion separates the relaxation profiles into individual exponential decays, providing more detailed information than simple $1/e$ intercepts. The millions of data points from the pulse sequence necessitate a powerful Laplace Inversion script, developed by collaborator Dr. Yiqiao Song. This work was also performed in collaboration with C. Selco with theory support from Dr. C. Bengs, while further analysis of the AC field sensing in later sections is enabled by C. Shah, E. Richter, and L. Moon.

7.1 Adaptation of Experimental Protocol

The pulsed spinlock sequence described in Chapter 1 is the basis for the experimental protocol here. As described previously, we start with hyperpolarization at low field, followed by shuttling to high field. All experiments in Sections 7.3 and 7.4 are performed at 100 K on the cryogenic field cycling instrument; all experiments described in Section 7.5 are performed on the room temperature field cycling instrument. Just as in the spinlock sequence, RF control is applied via fast RF pulses with tip angle θ_x where the projection of the magnetization of the nuclear spins onto the $\hat{\mathbf{x}}/\hat{\mathbf{y}}$ plane is measured as S.

We note here that the estimation of tip angle is of paramount importance to much of this chapter. To this end, we conduct ^{13}C Rabi experiments and fit the obtained nutation to a sinusoidal curve. A spin-locking train of $\sim\pi/2$ pulses and continuous readout for t=70 s is employed while the pulse length of the initial pulse θ_{init} is varied (Figure 7.1A–B). The integrated signal is measured and fit to a sine curve, as shown in Figure 7.1C. High SNR yields a high-precision estimate of θ, with an error of within 1%.

In Section 7.3, an additional transmitter offset is applied, using the Varian VNMRJ software. This affects both the frequency of the transmitted pulses and the frequency at

which the receiver is set; however, since the solid NV diamond sample has a broad ^{13}C linewidth, and our calculation of S relies on the integrated area over this broad linewidth, the resulting frequency shift is already encompassed in the measured signal. Otherwise, a typical pulsed spinlock sequence is used, with $\theta = \pi/2$ (nominally). We note that as the transmitter offset changes, "pulse error" is accumulated. Pulse error from transmitter offsets is typically avoided in conventional NMR experiments [111, 68] which rely on well-calibrated pulses in order to manipulate the nuclear spins as anticipated. However, we note that the pulsed spinlocking sequence is agnostic to the flip angle experienced by the nuclear spins and continues to preserve the spin lifetime regardless of the pulse error.

In Section 7.4 the same transmitter offset is applied in the same manner—during both RF pulse application as well as receiving nuclear spin precession. However, the pulsed spinlocking sequence here utilizes small angle pulses: nominally $\theta_x = 10°$, where the pulse length is minimally $t_p = 2$ μs. While this sequence may be performed with an initial tipping pulse (nominally) of $\theta_y = \pi/2$, the signal in this case is extremely low. We plot the signal of these spinlock curves at very short pulse angle as a function of the initial pulse angle in Figure 7.2. (This, essentially, is a Rabi experiment performed with a spinlocking train of pulses at $t_p = 8$ μs and 5 kHz off resonance.) Notably, using a nominal $\pi/2$ pulse of $t_p = 33$ μs results in very low signal. We posit that this is because the magnetization is tipped near the $\hat{\mathbf{x}}/\hat{\mathbf{y}}$ plane and far away from the protected axis, leaving large amounts of magnetization to decay as the nuclear spin trajectories converge on the spinlock protected axis [166]. Instead, setting $\theta_y = \theta_x$, such that the initial tipping pulse is the same length as the spinlock train of pulses results in higher overall signal. The reasons behind this choice are discussed further in Section 7.4.

7.2 Laplace Inversion

It is relevant to briefly discuss Laplace Inversion and the assumptions underpinning this technique before its use in understanding our data decay profiles. Laplace Inversion (LI) or, as it is commonly termed in NMR, Inverse Laplace Transform (ILT) is a numerical method used to represent relaxation decay behavior as a distribution of exponential components. However, ILT is fundamentally known as an ill-posed problem [148, 41, 108, 178]; that is, small changes and errors in the input data can lead to drastically different results. This ill-posedness can be mitigated through truncated Singular Value Decomposition (SVD) [178]; regularization methods such as Tikhonov regularization [178, 41]; or other methods including non-negative least squares (NNLS) [41, 33, 63], non-linear least squares (NLLS) [41] or maximum entropy [33], which all add constraints to the results in order to force convergence. For example, truncation of SVD imposes a maximum number of components which are meaningful to the spectra [178], Tikhonov regularization imposes that the resulting function of the Laplace Inversion be smooth [179], NNLS forbids negative peaks [41], and NLLS and maximum entropy both attempt to converge the results into a pre-specified number of exponentials (maximum entropy converges to the minimum number of exponentials) [41, 33].

It is thus important to choose the additional constraints as a function of the system under study, with prior knowledge of the expected outcome.

In this dissertation, we use both truncated SVD and Tikhonov regularization, as per the algorithm presented by Song et al. in Ref. [178] to perform Laplace Inversion. (We note that the use of the term "Laplace Inversion" over the more commonly used "Inverse Laplace Transform" is chosen in this dissertation to emphasize that the result is obtained by numerical inversion of an ill-posed inverse problem rather than by exact analytic inversion.) This algorithm holds two main advantages: first, the truncating of SVD and Tikhonov regularization are relatively mild constraints which make few assumptions about the data: truncation of SVD is confirmed by the noise level of each individual dataset, such that all singular values that contribute more significantly than the noise are included; Tikhonov regularization simply makes the resulting function smooth, which is a reasonable assumption based on our knowledge that the system is a distribution of ^{13}C nuclei which is spatially varying from the NV center electron. The second advantage of this algorithm is that since it is built for two dimensional datasets, it is capable of handling large quantities of data. The ill-conditioned nature of the Laplace transform is known to make its solving slow; the algorithm used here is capable of processing hundreds of datasets with up to 12 million data points each, with no truncation.

Mathematically, LI solves the equation

$$S(t) = \int w_{T_2'} e^{-t/T_2'} dT_2' + \epsilon(t), \tag{7.1}$$

where S(t) is the signal decay data collected by the experiment. We discretize this form into a sum of exponentials with different weights (W_j) and decay times (T_{2j}'). $\epsilon(t)$, then, is the accounting of the noise contribution which is actually present in the experiment. Mathematically, it becomes the residual error of the model.

In practice, the LI is performed numerically by performing a regularized ℓ^2 optimization on the following objective [179, 190]

$$\min_W ||S - KW||_2^2 + \alpha ||W||_2^2, \tag{7.2}$$

where S and W are the discretized vectors of the signal and weights, respectively. $K_{ij} = e^{-t_i/T_2^j}$ is a matrix representation of the exponential kernel function, and α is the aforementioned Tikhonov regularization parameter.

The reason for controlling smoothness with α is to prevent both overfitting and underfitting. Overfitting (fitting to noise) occurs when α is non-existent or set too small, resulting in an unstable inversion. In contrast, if α is chosen to be too large, the fit will miss some of the finer features in the data by broadening and smoothing all resultant T_2' peaks. We choose α through the S-curve method described by Song et al. [179], which validates the choice of α through balancing the fit error (χ) with the noise in the experiment. A typical experimental S-curve is shown in Figure 7.3 where the fit error is plotted as a function of α. The optimal α from this plot, then, occurs at the heel: above any instability from overfitting

to noise (shown as minor changes in the baseline of the S-curve) but below the large, near vertical increase in the fitting error. Extensive comparison of S-curves across many datasets revealed optimal α values which ranged between $0.1 \leq \alpha \leq 10$ depending on the SNR of the original dataset.

Figure 7.4 demonstrates how the LI maps change as a function of α. In the top row, Figure 7.4A–C, the dramatic effect that α can cause on the datasets is visible. First, in (A) α is set to be too small for the dataset. Here, overfitting to noise occurs, allowing for the "detection" of many small peaks with LI, which are unstable and move around at different (small) values of α. In comparison to a more reasonable value of α for this dataset ($\alpha = 1$, shown in Figure 7.4B), these peaks are narrow, and in certain datasets, contain maxima which are up to an order of magnitude higher (appearing as yellow in the color bar). Figure 7.4C demonstrates the opposite problem, where α is too large for the dataset. At $\alpha = 1000$ the peaks smear and broaden into each other, losing the LI result which indicates that multiple small peaks appear between $1 \leq T_2' \leq 100$ s. Instead, these are treated as a single broad contribution. The fit error with this value of α is high, indicating that multiple small peaks are a better representation of our data.

Within the range of optimal α values, we find there is minimal difference in the outcome of the LI. These are plotted for the same LI map of 51 datasets in Figure 7.4D–F. We observe that across the LI maps where $\alpha = 0.1$ (D), 1 (E), or 10 (F), all small peaks are maintained with stability. Some slight broadening occurs as a function of α (most visible in (F)) but fit errors do not increase so much as in (C). Thus, we can safely fit most datasets to any α within the optimal range without significantly changing the results of the inversion.

Typically, LI is limited by experimental noise. Indeed, this is a concern especially for data taken at small angle where (as we will later see) the signal is up to 90% lower than experiments presented in Section 7.3. In our case, this issue is largely mitigated by our high initial polarization levels and quick sampling rates of 10^9 samples per second. However, we can experimentally demonstrate the robustness of LI to noise in Figure 7.5. The addition of Gaussian white noise to an example spinlock decay curve is demonstrated in Figure 7.5A–C. Here, an additional value of "noise" of up to 0.01 (B) or 0.03 (C) times the value at that point is added or subtracted randomly using a native MATLAB function. Gaussian white noise is chosen as this is the form of noise that is assumed by ϵ in Eq. 7.2. Other types of noise would not be well-modeled by this method of analysis and result in a high fit error [179]. The addition of Gaussian white noise is performed across all data sets from offsets of -5 kHz to $+5$ kHz, which is the main focus of data presented in Section 7.3. In Figure 7.5D–F we observe that across these experiments, the addition of white noise did not significantly change the LI result, with near identical weights and T_2' values across the addition of Gaussian noise. We note that the addition of noise is chosen to mimic the SNR of our lowest SNR dataset from Section 7.4, supporting the robustness and usability of this data analysis method even for such datasets.

Finally, we address the effect on the LI that occurs when the entire exponential decay curve is not captured by the dataset. Especially with datasets in Section 7.4, the calculated T_2' lifetimes are longer than what can be captured by the instrument, as the rapid sampling

necessary for high SNR also fills up the 16 GB of memory available on our instrumental hardware. At the minimum sampling frequency practical with our hardware, we are still limited to experimental times of less than 10 min (600 s) of quasi-continuous sampling. While initially thought to be sufficient when considering the on-resonance T_2' lifetime of $\sim$ 100 s, it quickly became apparent that the long ($>$ 800 s) lifetimes of small-angle, off-resonant datasets would exceed the measurement capabilities of the instrument. The question then arose: how can LI be used on incomplete decaying datasets?

In principle, the LI will continue to function even when incomplete data is input. However, a decreased number of singular values may be available [178] resulting in peak broadening, especially at T_2' values beyond what is measured. Should enough of the decay be measured, LI will be able to anticipate the long time components but will be unable to identify their length exactly, leading to broadening as an intrinsic form of uncertainty. To test this, we again turn to our exemplary dataset of LI maps of 51 values ranging from offsets of -5 kHz to $+5$ kHz. We again note that this is a dataset which will be discussed in more depth in Section 7.3; it is most pertinent here to mention that all of the datasets included in this map decay fully within the measurement window of 10 min but most do not decay fully by 3 min.

Figure 7.6 shows the effect on LI when datasets do not achieve their full decay. In Figure 7.6A, we show the LI map of the normal datasets, with data collected to 10 min. In Figure 7.6B–C, we truncate the raw datasets at 5 min and 3 min respectively and perform the same data analysis and LI on each. As the same datasets are examined, we clearly see the expected effect of truncation on LI through the resulting maps. All components experience some broadening, with the shortest T_2' components being least affected and the longest T_2' components becoming extremely broadened with truncation. While in (A), the longest T_2' component is well localized between 100–200 s for most datasets, in (B) and especially in (C), the longest T_2' component for these datasets show a distribution whose tail extends to $\sim$ 1000 s. As we can see by the fact that these datasets decay completely by 10 min (600 s), this additional tail is a result of the truncation and uncertainty that is added—the inversion can fit the truncated data with a wide array of long time exponentials. However, we note that qualitative features captured by the LI mapping remain similar across Figure 7.6, regardless of truncation. When datasets have longer decay times than are captured experimentally, we may use LI to interpret the change in qualitative features with the acknowledgment that the inclusion of T_2' values beyond 600 s is a result of poor LI from incomplete decay.

Before examining the results in detail, it is worthwhile to first consider the choice of Laplace Inversion as the analytical method for this data and the assumptions underlying its use. LI fundamentally treats the decay curves as a sum of exponentials (see Eq. 7.1); because of this, it is widely used in NMR literature [41, 63, 108]. Relaxation behavior is typically treated as families of spins relaxing independently according to the Bloch equations (see Chapter 5 for more discussion), thus a sum of exponentials describes relaxation well in conventional NMR treatments. At the time of this analysis, there was no reason to believe that the data did not fit well to this sum of exponentials; while results from Beatrez et al. [25] indicated that this system was well fit by a stretched exponential, the decay curves measured

on resonance did not seem to fit the stretched exponential behavior previously reported. Further modeling and theory (reported in Chapter 5 as resulting from work by Selco et al. [173]) have indicated that these decays are better understood as a product of a monoexponential and stretched exponential; we see evidence in the LI maps that supports this explanation in future sections. Nonetheless, LI still produces informative data: as a stretched exponential can be represented by a broad distribution of monoexponentials, the inversion's broadening can be representative of the stretched exponential behavior. Throughout this chapter, we ought to view the inversion results as a qualitative description of the relaxation dynamics and how they change with offset and pulse angle, rather than attempting to interpret the T_2' values as independent, discrete exponential components.

7.3 Magic Angle Decoupling

We finally turn our attention to the details of the LI maps and the data contained within. The same data as was used to explore the effects of LI in Figure 7.4, Figure 7.5, and Figure 7.6 is presented as the optimized LI map, with $\alpha = 0.1$ in Figure 7.7. The frequency offset is varied over 51 values from $\Delta\omega\in[-5, 5]$ kHz using a pulse train of pulses with a nominal flip angle θ=90°. LI analysis of the normalized time-traces is then performed using the full datasets taken to t=600 s. We then show the LI results as a 3D plot; $T_2'^j$ values are plotted on the logarithmic vertical axis, the offset $\Delta\omega$ is plotted on the horizontal axis, and weights w_j are represented by colors (see color bar). In Figure 7.7A, the solid green spline is a guide, highlighting the longest-time $T_2'^j$ component present in each dataset and its motion as a function of offset. A significant increase in this component is demonstrated at $\Delta\omega\approx\pm 2$ kHz (red dashed line) where the $T_2'^j$ is calculated to be $\approx$ 680 s by the LI analysis. This creates a prominent horn-like feature in the LI map. In contrast, the shorter-time components remain largely unchanged regardless of offset (gray dashed lines). Black points (joined by the dark gray line) show the corresponding T_2' values obtained from just a $1/e$ intercept; a common method of deriving T_2' when it is assumed that a single spin population is present in the sample. While interpretation of the data through a $1/e$ intercept reveals a similar trend (with the appearance of the horn-like feature at $\Delta\omega\approx\pm$ 2 kHz), the information content within it is much lower. With LI we can resolve that the longest time component appears to be driving the extension of lifetime around an offset of 2 kHz.

To understand the cause of the extension of lifetime that causes the horn-like feature, Figure 7.7B depicts an analogous set of experiments for the right half of Figure 7.7A, i.e., $\Delta\omega\in[0, 5]$ kHz. We choose this limitation to decrease total experimental time; as the system appears symmetric in the $\Delta\omega\in[-5, 5]$ range, only one half of this range need be examined to understand the qualitative behavior. Thus, in Figure 7.7B, the pulse power was decreased (the bottom panel represents data taken at identical pulse power to Figure 7.7A), a nominal $\pi/2$ pulse was re-calibrated and applied for each data set. In the top right corner of each panel, the time-averaged (effective) Rabi frequency Ω of the drive (considering both the pulses and the delay between the pulses) is calculated. As the effective Rabi frequency

increases, the horn-like feature of the long-time $T_2'^j$ component shifts to higher $\Delta\omega$ as indicated by the dashed lines. We also note that at higher pulse powers (and thus higher effective Rabi frequencies), there is increased broadening in the long-time $T_2'^j$ component; we attribute this to the fact that at higher effective Rabi frequencies, the pulsed spinlocking drive better preserves magnetization, resulting in longer lifetimes. This effect has previously been reported in Chapter 6 and Refs. [25, 84].

The resulting shift of the long-time component with $\Delta\omega$ approximately matches with $\Delta\omega = \Omega/\sqrt{2}$ — the condition matching Lee-Goldburg decoupling [110, 123]. This condition occurs when the effective spin-locking axis aligns to the magic angle ($\vartheta = 54.74°$), thus decoupling the ^{13}C nuclei [80]. The time-averaged effective Hamiltonian $\mathcal{H}_{\text{eff}}$=0 of the spinlock vanishes to zeroth order in the Magnus expansion, self-decoupling the ^{13}C nuclei. Lee-Goldburg decoupling is typically performed by the addition of a second off-resonance irradiation which tilts the spins to the magic angle. Since the 1960s, it has been well-studied especially in combination with Magic Angle Spinning (MAS) of solid-state samples [88]. Further development of frequency-switched Lee-Goldburg (FSLG) [123, 112, 28] and phase-modulated Lee-Goldburg (PMLG) [192] pulse sequences have corrected for hardware imperfections and the need to measure more complex or low abundance samples on resonance [191, 88].

It was noted by Mehring and Levitt [123, 112] that the addition of measurement windows into the sequence was challenging; pausing the secondary irradiation in order to open the receiver for measurement, even when inserted in a way to preserve the dipolar decoupling, leads to higher-order terms hastening decay [112]. While advances in hardware have since allowed for much faster receiver switching and thus minimization of this effect, the field has largely targeted improvements of homonuclear decoupling sequences such as PMLG and DUMBO that are performed during evolution and not simultaneously with acquisition [132, 192] and faster MAS speeds where appropriate [137]. This pulsed spinlocking method of constructing the Lee-Goldberg condition is interesting, then, as it embeds the measurement window into the sequence: the window-opening problem is avoided by the fact that off-resonant irradiation occurs only with the pulses. Thus, the opened windows for measurement act as a modulation to the Rabi frequency of the drive (similarly as to what was described in Chapter 6) as opposed to creating sporadic imperfections in the drive.

We attribute slight discrepancies between $\Delta\omega = \Omega/\sqrt{2}$ and the actual $\Delta\omega$ at which the longest lifetime occurs to errors in pulse calibration. Since the off-resonant RF field is being created as a result of off-resonant pulses, significant pulse errors are introduced, making the calculation of the effective drive more difficult. We note that the effective drive frequency reported in Figure 7.7B is calculated based on the tip angles achieved by nominal pulse lengths (see Figure 7.1) where a 2π rotation is completed with four $\pi/2$ pulses in the drive. The significant offsets present in these experiments create a shift in the actual tip angle of the pulses, which varies with offset across the LI map. For this reason, only the nominal effective drive frequency is reported. Still, we find only minimal discrepancies between the actual peak $\Delta\omega$ and that predicted by $\Delta\omega = \Omega/\sqrt{2}$.

In general, while both pulsed spinlocking on resonance and off resonance at the LG

condition lead to extended T_2', we rationalize the extension in the LG case as due to (1) the reduced weight of higher-order terms which are suppressed due to the spin vector being at the magic angle, and (2) the suppression of spin-diffusion effects among ^{13}C nuclei. This suppression is discussed in greater detail in Ref. [173]. Figure 7.7C depicts this schematically.

The results presented here are generally a successful reformulation of Lee-Goldberg decoupling in a manner where the observation windows are integrated into the decoupling sequence. However, the LI maps offer a glimpse of more insightful questions that can be gleaned from this data. When achieving the LG condition at ~ 2 kHz offset, why does the broadest T_2' component exist for the dataset which does not contain the longest $1/e$ lifetime? And why does the $1/e$ lifetime decrease slightly in a location which corresponds with a discontinuity in the LI map at ~ 3.2 kHz off resonance? The pursuit of answers to these questions led us to discover several interesting behaviors.

We first attempted to isolate how the effect of the weakened Rabi frequency (caused by lower power pulses) may change the overall LI signal; after all, as described in Chapter 6, weakening the effective Rabi frequency may be performed by weakening the pulses (which alters the pulse length of the nominal $\pi/2$ and thus the length of the overall cycle) or simply by lengthening the overall cycle by increasing spacing between pulses. This result produces the same conclusions as were depicted in Figure 7.7B. However, in performing these datasets, we noticed a change in the LI maps as a function of the weakened spinlock. As the interpulse spacing was increased (legend, Figure 7.8A) the pulsed spinlock lifetime decreased; this certainly is to be expected: the longer cycle time "kicks" the spins less frequently to maintain them along the spinlock axis. The form of the LI inversion also changes (Figure 7.8B–C), surprisingly. Notably, as the interpulse spacing increases, the inversion results begin to appear more similar to what an LI would produce were it given a simulated stretched exponential, with a stretching factor close to 1/2, matching previous experiments [25].

If changing pulse power is considered a fine tuning knob, then changing interpulse spacing can have much more dramatic effects. Sweeping offset at very long interpulse spacing (doubled, creating an effective Rabi frequency $\Omega_{2\tau} \approx 0.6\Omega_\tau$, Figure 7.9) creates an LI map with the LG condition at ~ 1.2 kHz followed by multiple decreases in lifetime where the results from LI poorly fit the data. The cause of these decreases were poorly understood; their best explanation comes from investigating how pulse length affects LI maps.

When considering Figure 7.7, four regimes are of particular interest: on resonance ($\Delta\omega =$ 0 kHz), the LG condition ($\Delta\omega = 2.0$ kHz), the strange decrease in signal lifetime ($\Delta\omega =$ 3.4 kHz), and the furthest extent we can measure off resonance ($\Delta\omega = 5$ kHz). As an attempt to identify the cause of the decrease in signal lifetime at $\Delta\omega = 3.4$ kHz in Figure 7.7 as well as in Figure 7.9, the LI is calculated as a function of pulse width at each of these key offsets. Figure 7.10 shows these four LI maps. In all four, a standout drop in signal lifetime is apparent in the $1/e$ lifetimes, marked in red. This drop in signal lifetime also results in large fluctuations in the LI components. When examining Figure 7.10A, we realize that this is simply the resulting LI map from the data with which we are familiar in Chapter 6; varying pulse train pulse width on resonance from $t_p = 0$ μs ($\theta = 0$) to $t_p = 80$ μs ($\theta \approx 1.2\pi$). From this context, we quickly realize that the drop in $1/e$ lifetime is due to the zero-crossing that

occurs around $\theta = \pi$ — in this dataset, where $t_p = 66$ μs. Importantly, LI attempts to fit the data, resulting in a single, sharp fast decaying component (from the sharp drop to $S = 0$) as well as a long-lived component (which comes from the signal recovery and subsequent decay, see Figure 6.4). However, *the LI does not produce meaningful results when the zero-crossing occurs* due to the fact that the lineshape cannot be represented by the kernel of exponentials. The zero-crossing is confirmed by investigating the decay curves of S vs t and observing their presence.

The same zero-crossing-related decrease in lifetime also appears in Figure 7.10B–D, albeit shifted leftward to shorter pulse lengths: starting at $t_p = 60$ μs in (B), at $t_p = 48$ μs in (C), and at $t_p = 38$ μs in (D). A recovery to the initial form of decay (and to a better description of the decay when using LI) occurs in (C) and (D)—in both (A) and (B), the zero-crossing is still present in the S vs t decay curves at $t_p = 80$ μs. Even at long pulse lengths, LI still accurately describes the decay so long as some other process is not occurring.

Yet we see a still unexplained decrease in signal lifetime in Figure 7.10B–C occurring before the zero-crossing formation. The decrease in Figure 7.10C is centered around $t_p = 33$ μs, which is the pulse train pulse length for Figure 7.7; this effect is occurring in Figure 7.7 because changing the resonance offset simultaneously changes the effective pulse length through the addition of the pulse error. We note that this small decrease in lifetime was also observed in Chapter 6 in Figure 6.5, at kick angles $\theta/\pi \approx 0.65$. This decrease in signal was ultimately explained by C. Selco in Ref. [172] and attributed to triple spin flip resonances which hasten heating. Following from this conclusion, the last decrease in signal lifetime, at $t_p \approx 70$ μs in Figure 7.10D is likely the double spin flip resonances which are predicted to occur at large detuning [172].

Another interesting feature appears when we consider the four LI maps of Figure 7.10: the $1/e$ lifetimes and longest-lived T_2' component surprisingly demonstrate an extension at very short t_p when off-resonant. Short angles such as these ought to result in a weaker pulsed spinlock, as so many more pulses are necessary in order to complete a full 2π cycle. This result merits a deeper inspection.

7.4 Small Tip Angle Lifetime Extensions

In Figure 7.10, we notice that at small tip angles off resonance, the spin lifetime seems to get longer, as evidenced by an increase in $1/e$ lifetime as well as the longest-lived T_2' component. In Figure 7.10A, however, where the sequence is on resonance, the short angle pulses do not result in an extension in lifetime. The lifetime decays quickly when using short $t_p = 2$ μs pulses, as predicted from Floquet theory [1, 25]. This indicates that the addition of off-resonance to the pulses is what results in this long-lived component.

We track the behavior of the short angle pulsed spinlock decays as a function of offset in Figure 7.11. In Figure 7.11A, normalized decay traces are shown on a semi-logarithmic scale with nominal pulses θ=5°. The change in color from orange to blue represents increasing

offset values from $\Delta\omega = 0$ kHz to $\Delta\omega = 5$ kHz. As anticipated, the shortest lifetime (T_2'=34 s) occurs on resonance (bottom trace in Figure 7.11A).

Surprisingly, the increase in T_2' upon going off-resonance occurs immediately with even moderate offsets. At $\Delta\omega = 5$ kHz, we estimate $T_2'\approx$800 s (purple curve in Figure 7.11A) from the $1/e$-crossing. This corresponds to a remarkable >533,000-fold increase in T_2' lifetime over the free induction decay T_2^* value, and constitutes a record value for lifetime extension compared to other platforms where Floquet prethermalization has been observed before [56, 142, 176, 164, 144, 25] (see SI of Ref. [85]). Importantly, this is achieved with a rather minimal amount of spin control: within one T_2^* period, the pulses only add up to a single (nominal) π rotation. We therefore consider this to be an unexpected extension in the T_2' lifetime.

Another noteworthy finding is that the traces in Figure 7.11A become progressively more monoexponential with higher $\Delta\omega$. To illustrate this, Figure 7.11B shows a T_2' LI map of the normalized traces as a function of $\Delta\omega$. The data reveals a significant increase in the position and weight of the long-time T_2' component away from resonance, while the shorter-time components diminish. The cyan solid line is a spline fit to the longest component, while dark blue points show the corresponding $1/e$ intercepts.

There are several salient features to point out in Figure 7.11B. First, the $1/e$ intercepts are only shown for $0 \leq \Delta\omega \leq 1.8$ kHz. At offsets $\Delta\omega \geq 2$ kHz, the signal decays become exceedingly long lived and do not cross $1/e$ in the available experimental time. Note that since pulses are $t_p = 2$ μs for this dataset, the duty cycle is only ≈ 40 μs; slightly more than half of a typical duty cycle — this means that almost double the number of acquisition windows are opened using this sequence and hence nearly double the amount of data is collected. To compensate, the total experimental time is decreased by half to $t_{max} = 300$ s (5 min). Any decay curves that do not decay to $1/e$ by 5 min do not report a $1/e$ value; only the long time component T_2' values from LI are examined.

Another salient feature is, in fact, these long-time component T_2' values. One may consider two possible reasons for a lifetime extension when the dataset is composed of multiple short and long-lived components: first, that the longest-lifetime component simply becomes more dominant, or second, that some or all of the components shift to longer time constants. It appears that the lifetime extension due to short angle, off-resonant pulses is mainly driven by this latter reason. The longest-time T_2' component shifts from being centered around 100 s while on resonance to achieving nearly 800 s at 5 kHz off resonance. We note that earlier, when discussing the Laplace Inversion method, we specifically noted that assignment of T_2' components that are longer than that of the measurement period is inherently uncertain; this uncertainty likely contributes to the fluctuations in broadness of the long T_2' components in the LI maps. We note that the continued progression of T_2' to higher values as the data goes farther off resonance is supported by the normalized signal decays in Figure 7.11A, which demonstrate this extension visually. Later experiments, performed after a system upgrade enabling continuous collection of data up to 30 minutes also demonstrate that the predicted long T_2' lifetime was approximately correct (Figure 7.12).

Figure 7.11C presents line cuts at $\Delta\omega$=0 kHz (orange, shaded) and 5 kHz (blue); for

the latter, the T_2' spectrum is dominated by a single component at T_2'≈800 s, estimated by the centroid. This comparison of the two extremes of this behavior (lifetime shortening on resonance, lifetime extension off resonance) is also useful to visually compare the shape of the LI results. At this short angle condition and off resonance, the single component of the T_2' spectrum emphasizes that this decay curve can be well approximated with a monoexponential. In comparison, at the short angle condition and on resonance (orange, shaded) the T_2' spectrum appears very similar to one which would be produced by simulated stretched exponential behavior with a stretching factor of $\beta = 1/2$. Selco et al. reproduced and built on these results when crafting Ref. [173], determining the reason for the emergence of the monoexponential behavior at this far off resonant condition.

This unexpected extension in lifetime can be intuitively understood using the vector picture. In short, the prethermal axis aligns more towards $\hat{\mathbf{z}}$ with increasing offset, schematically shown in Figure 7.13A, allowing T_2' to asymptotically approach the T_1 limit far off-resonance. The theoretical model in the SI of Ref. [85] supports this picture. Since the protected spinlocking axis is so close to the $\hat{\mathbf{z}}$ axis, the processes which are typically associated with T_1 relaxation contribute increasingly to the T_2' decay. Consequently, referring to these only as T_2' values obscures the continuous ability to tune spin control between the $\hat{\mathbf{x}}$ and $\hat{\mathbf{z}}$ axes.

We emphasize finally that the data in Figure 7.11A shows normalized signal vs time decays. Indeed, tilting of the prethermal axis towards $\hat{\mathbf{z}}$ with increasing $\Delta\omega$ leads to a significant loss in absolute signal. Figure 7.13B shows the initial signal amplitude (at t=0 s) as a function of $\Delta\omega$ for nominal θ=5°. We note that the high SNR achieved by hyperpolarization and the long lifetimes when collecting data at cryogenic temperatures are the two major advancements which allow us to collect usable data from this pulse sequence.

In many ways, the extension of lifetimes at short-angle and high-offset is obvious. As elucidated in Chapters 3 and 4, the electron bath, and especially the NV center electron that is in close proximity to the hyperpolarized region of ^{13}C spins, is the main source of nuclear spin relaxation. And, as elucidated in Chapter 6 (more specifically, Figure 6.2), when the ^{13}C spins are oriented in the $\hat{\mathbf{z}}$ direction, the NV center electron does not strongly act to relax the spins. In this way, placing the protected spinlock axis at the minimum deviation from the $\hat{\mathbf{z}}$ axis as possible to still yield a measurement results in the ^{13}C spins acting as though they are experiencing the same relaxation behavior which gives rise to T_1.

7.5 Application for AC Sensing

While overcoming several measurement challenges, neither of the results presented in Sections 7.3 or 7.4 are particularly surprising or novel. However, they do open a regime which is seldom used for quantum sensing: measurement of a non-optimized M_{xy} in favor of the long lifetime available when the protected axis resides close to I_z. We consider, in particular, the sensing of time-varying (AC) magnetic fields $B_{sens}(t) = B_{AC}\cos(2\pi f_{AC}t + \phi)$ using the hyperpolarized ^{13}C nuclei, adapting a method previously described in Ref. [165].

Figure 7.14A shows a schematic of the protocol we use where the ^{13}C spins are subject to the pulsed spinlocking sequence either at short angles and far off resonant or on resonant with typical $\theta = \pi/2$ pulses in order to compare with the sequence of Ref. [165]. The AC field does not need to be synchronized with the sequence, although we find that in the case of on-resonance $\theta = \pi/2$ sequences, making the AC field synchronized with every full 2π rotation yields the highest sensitivity [165, 166]. The sensing principle involves ^{13}C nuclei prethermalizing to a time-varying Hamiltonian that includes the AC field; the spin micromotion dynamics then reports a direct imprint of $B_{sense}(t)$ [166, 165]. This results in oscillatory deviations ΔS on top of the signal S and proportional in magnitude to B_{AC}.

The data presented in Figure 7.14 is notably taken at room temperature, on the fast field-cycling instrument described in Refs. [11, 129]. This is due exclusively to the fact that this instrument contains a well-characterized AC field coil for applying small fields at the sample from its previous use in Refs. [165, 166]. The cryogenic field-cycling instrument, on the other hand, has yet to integrate an additional coil within the probe geometry for AC sensing (see Chapter 2). While the effect of temperature on transverse lifetime extension is not pronounced when compared to the effect of the offset (Chapter 3), the continuous cryogenic cooling of the probe components protects them from the millions of pulses that are being sent. Attempting to perform a similar sequence to the same experimental times of 5–10 min on the room temperature instrument can cause probe arcing and subsequent death; while some probes in the room temperature setup may die, this was a sacrifice that the graduate students predominantly working on this instrument were not willing to make. Thus, with the exception of the two experiments shown in Figure 7.14B, all other calibration or comparative datasets, including those presented in Figure 7.14D–E, were limited to maximum experimental times $t_{max} = 180$ s; the data in Figure 7.14B was not replicated to experimental times beyond $t_{max} = 180$ s.

Sensing is effective over a relatively wide bandwidth of $f_{AC} \in [10\text{ Hz}, 1\text{ MHz}]$; where the lower limit is determined by the experimental time while the upper limit is determined by the shortest interval between pulses. This sensing bandwidth lies in a blind spot [130] between vapor cell magnetometers [36, 90, 105] and electron-based sensors such as NV centers [122, 106, 165], and is therefore in a practical useful range.

Figure 7.14B, then, shows the sensing results for a single-tone AC field at $f_{AC} = 50$ Hz with $B_{AC} = 82$ μT. In contrast to other quantum sensing platforms [51], only a single-shot of initialization (hyperpolarization) is applied here. Signal S is measured continuously for $t\sim$10 min; signal deviations ΔS are extracted by baseline correction as per Ref. [165]. These deviations are shown more clearly in Figure 7.14B by presenting windows of $\Delta t = 100$ ms at $t = 1, 3, 5$, and 9.6 min, respectively. In Figure 7.14B(i), the on-resonant case is shown in green with flip-angle $\theta = 90°$, while the off-resonant case is shown in Figure 7.14B(ii) in yellow with nominal $\theta = 10°$ pulses. Both of these sub-figures show data in a lighter version of green/yellow with a sinusoidal curve fit to the response plotted in a darker green/yellow overlaid on top. The numbers marked in gray indicate the measured SNR of the AC field signature over the noise floor measured in a 1 s interval for each window. While the SNR of both signals in (i) and (ii) decay with the signal baseline, the SNR is sustained in (ii) at

off-resonant and short angle pulses, continuing to yield reliable signal measurements through the last time window shown here at 9.6 min.

Evidently, ΔS demonstrates a direct imprint of B_{AC}. However, while the same B_{AC} was applied to both signals, the frequency response visible in ΔS is different: the on-resonant scheme in Figure 7.14B(i) is more sensitive to the second harmonic $2f_{AC}$, while the off-resonant sensing in Figure 7.14B(ii) captures the first harmonic f_{AC}. When a Fourier transform is taken of both datasets, however, both harmonics (as well as significantly weaker $3f_{AC}$ and $4f_{AC}$) are present. Indeed, the relative weights of the f_{AC} and $2f_{AC}$ components, from our calibration experiments, seem to largely depend on the offset. This indicates that choosing an off-resonance sequence under which to perform sensing can bias the same sensor to select between f_{AC} and $2f_{AC}$.

We note that to make a comparison in Figure 7.14B, the same B_{AC} was applied to both sequences. However, this frequency was optimized for the off-resonant sensing case, with the same field applied to the on-resonant case. In Ref. [166], the importance of aligning f_{AC} with the on-resonant $\pi/2$ sensing scheme is made apparent. Thus, while a direct comparison was attempted, in fact, the results compare an optimized off-resonant sensing scheme with an non-optimized on-resonant sensing scheme. This understanding did lead to a promising future direction, however. Data taken and analyzed by L. Moon is shown in Figure 7.15 where the f_{AC} is swept from 100 Hz to 5 kHz over the course of an experiment (as described by the methodology presented in [165]). Here, the FFT is shown as a function of the instantaneous f_{AC} for different offsets. In this dataset, the pulse sequence varies from on-resonance to 5 kHz off resonance, yet the pulse sequence remains the same, using $\theta = 15^\circ$ pulses. A peak in the FFT, shifting rightward, is the location of the optimal f_{AC}, which varies with offset. Since the short angles of the sequence result in very low SNR and fast signal decay for offsets close to resonance (less than 1 kHz); for these datasets the location of the optimal f_{AC} is obscured. Regardless, this preliminary data gestures towards an interesting use of the offset: to act as a tuning knob for the optimal sensing frequency of a sensor.

In Figure 7.14B, regardless of optimization, it is surprising that the ΔS deviations continue to live for so long in the off-resonant, short angle sensing scheme, as approximately 90% of the initial signal decays within the first T_2^* (as per Figure 7.13B). Physically, for sensing, we care most about the excursions of the spin vector which are due to the AC field away from the originally defined prethermal axis; measuring their projection on the $\hat{\mathbf{x}}/\hat{\mathbf{y}}$ plane. Naively, one might expect that lower SNR of the decay would result in lower SNR of the excursions which ride upon the decay. However, it is obvious that the strength of the oscillations that constitute the sensing signal are in fact larger for the off-resonant case, even though the on-resonant signals have the larger absolute magnitude. Additionally, the on-resonance ΔS signal decays significantly faster, as is evident moving rightwards in Figure 7.14B. By t=580 s, the off-resonance, small-angle signal (Figure 7.14B(ii)) shows an SNR that is almost an order of magnitude larger than the on-resonance case (Figure 7.14B(i)).

When considered more closely, the behavior of the spins becomes obvious. We grow accustomed to the decrease in SNR of the decay also corresponding to a decreased SNR in the deviations due to the fact that, typically, the decrease is a function of relaxation.

However, in this case the decreased SNR reflects a maintained coherence which simply has a small projection on the $\hat{\mathbf{x}}/\hat{\mathbf{y}}$ plane. When the B_{AC} field is applied, it moves the spins in a circular trajectory around the prethermal axis [166], with the width of the circle based on the $\hat{\mathbf{z}}$ deviation caused by B_{AC}. We examine this schematically with the vector picture shown in Figure 7.14C. On resonance, the large absolute signal moves in a deviation with a relatively small circular projection on the $\hat{\mathbf{x}}/\hat{\mathbf{y}}$ plane. In comparison, off-resonance near the $\hat{\mathbf{z}}$ axis, the same B_{AC} will result in a very large circular projection on the $\hat{\mathbf{x}}/\hat{\mathbf{y}}$ plane, more than compensating for the low absolute signal. This, combined with the incredibly long signal lifetimes at off-resonant, short-angle pulse sequences, potentially indicates the discovery of a new ideal sensing regime.

We evaluate the relative performance of the two sensing protocols over a range of offsets in Figure 7.14D by comparing the sensitivity. The signal intensity of the f_{AC} harmonic is calculated and integrated over the 3 min experimental time for pulse sequences where the nominal $\theta = 90°$ (green) and nominal $\theta = 15°$ (orange). We note that probe arcing for the $\theta = 90°$ sequence limits interpretation of the data above 4 kHz offsets. The slightly different short-angle condition is chosen to provide higher SNR over the full range of resonance offsets chosen. The measure of sensitivity as pT vs $\sqrt{Hz}$ is based on calibration with a known 82 μT B_{AC} applied through the coil as per the methodology described in the SI of Ref. [165]. We note that Sahin et al. [165] measure a best sensitivity of 410 ± 90 pT/$\sqrt{Hz}$; this corresponds to their sequence of $\theta = 90°$ pulses on resonance. In Figure 7.14D, we observe a similar sensitivity for this condition; however, even slight off-resonance pulses for this $\theta = 90°$ create dramatic improvements to sensitivity. Notably, we observe that the small-angle case outperforms in sensitivity to f_{AC} across the entire range; even on-resonance ($\Delta\omega$=0), it yields almost a 10-fold greater sensitivity.

Figure 7.14E shows T_2' values estimated from $1/e$ intercepts for both sensing datasets at room temperature, closely matching trends in Figure 7.7 and Figure 7.11B. We identify, for instance, the horn-like feature around $\Delta\omega$=2 kHz in the green trace and the lower T_2' lifetime for the small-angle case on-resonance which rapidly increases upon increasing $\Delta\omega$.

Finally, we comment that while data in Figure 7.14 considers a single AC tone, any complicated signal within the detection bandwidth will show a similar imprint [165]. We also note that the data in Figure 7.14B has not been optimized for sensitivity, and significant gains are possible through better hyperpolarization [168] and increasing sample occupation (filling-factor) in the readout cavity. However, the ability for long-time sensing demonstrated in Figure 7.14B allows for a reduced smallest detectable field via averaging [163], and a high-resolution discrimination of AC fields of comparable frequency [170].

This section ends, then, with the realization that the parameter space to choose an optimal regime for sensing is much broader than first anticipated. Even using $\theta = 90°$, moving slightly off resonance improves sensitivity. The fact that there is a two-dimensional (offset and pulse angle) sequence parameter space to tune, in addition to the f_{AC} which might be more or less sensitive to certain sequences, creates a vast realm of tunable parameters for sensing. Our next effort will be to attempt to quantify and measure this space. Additionally, effects may be more or less pronounced at different temperatures; longer lifetimes

and cryogenic cooling of the probe to enable long $\sim$ 10 min sequences may enable short-angle off-resonant sensing schemes to thrive as compared to the same experiments at room temperature which are limited in measurement scope by probe arcing and thus cannot take advantage of the whole lifetime of the sensor.

Preliminary data taken at a single AC field but varying both offset and pulse angle have thus far confirmed the picture that both off-resonance and short angle pulses are needed to maximally tip the protected axis towards $\hat{\mathbf{z}}$; however, both have an effect (pulse angle having a significantly smaller effect than transmitter offset). Attempts are ongoing by E. Richter and colleagues to simulate this behavior in order to predict which sensing is most optimal.

In summary, this chapter demonstrates long-time, reinitialization-free quantum sensing by exploiting extended prethermal lifetimes with small-angle off-resonance pulses. Since it is the deviations ΔS which control the sensitivity of the sensing and not the absolute signal level S of the prethermal state, we anticipate full use of the long T_2' times that were identified in Sections 7.3 and 7.4. Moreover, experiments in Figure 7.14 show sensing for $\sim$10 min with no re-initialization, also setting a record in both duration and the number of pulses ($\sim$7 M) employed. Even in its current form, this opens new applications in sensitive detection in a blind-spot region of ULF and VLF fields [130] and for underwater magnetometry [141]. We also envision similar approaches being applied to polarized ^{1}H nuclear spins in organic crystals, such as pentacene-doped naphthalene, where long T_1 times, due to diamagnetic singlet ground states, can exceed 100 hrs [60, 175]. The achieved $T_2'\approx$800 s values themselves, asymptotically approaching T_1, are a significant achievement demonstrating the greatest contribution to extensions in transverse spin lifetimes seen in this dissertation.

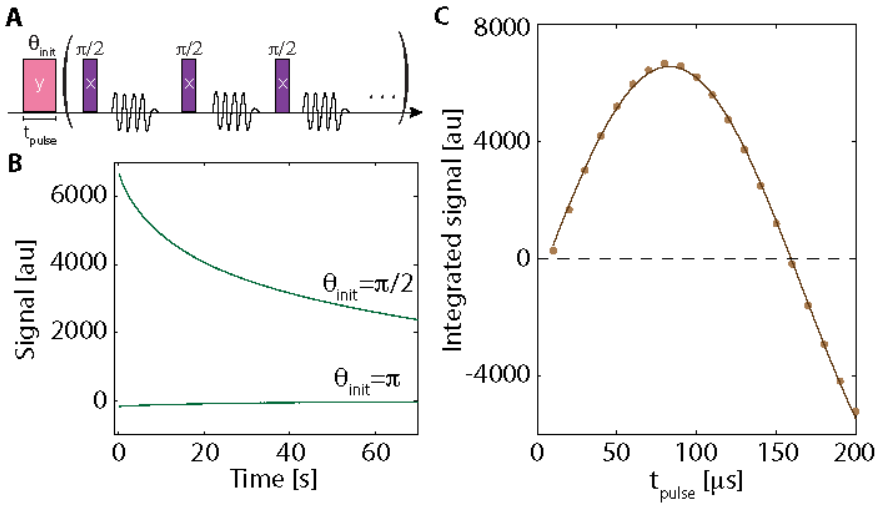


Figure 7.1 **Estimation of flip angle.** (A) Schematic of spinlocking Rabi experiment, consisting of a train of $\pi/2$ pulses, where the angle of the first pulse θ_{init}, is varied. (B) Typical signals in case of θ_{init}=$\pi/2$ and θ_{init}=π, with total measurement time of t=70 s, corresponding to $>$ 0.5 M pulses. (C) Variation of integrated signal S with length of the first pulse. Solid line represents sinusoidal fit. Slight off-resonance in the pulses leads to a finite signal even at θ_{init}=0.

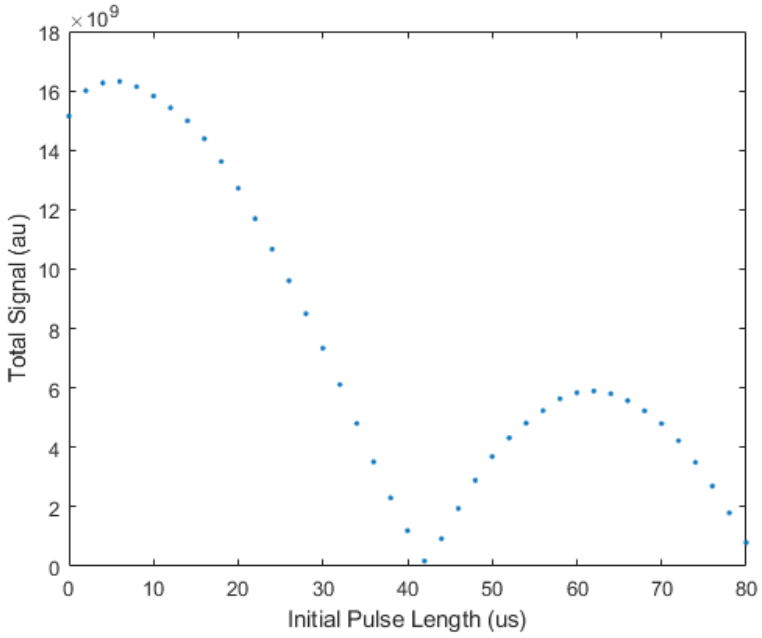


Figure 7.2 **Decrease in signal with initial pulse.** A "Rabi" nutation curve performed at 5 kHz off resonance using short, $t_p = 8$ μs pulse train pulses. The optimal initial pulse to use, based on the maximum total signal is $t_p = 6$ μs.

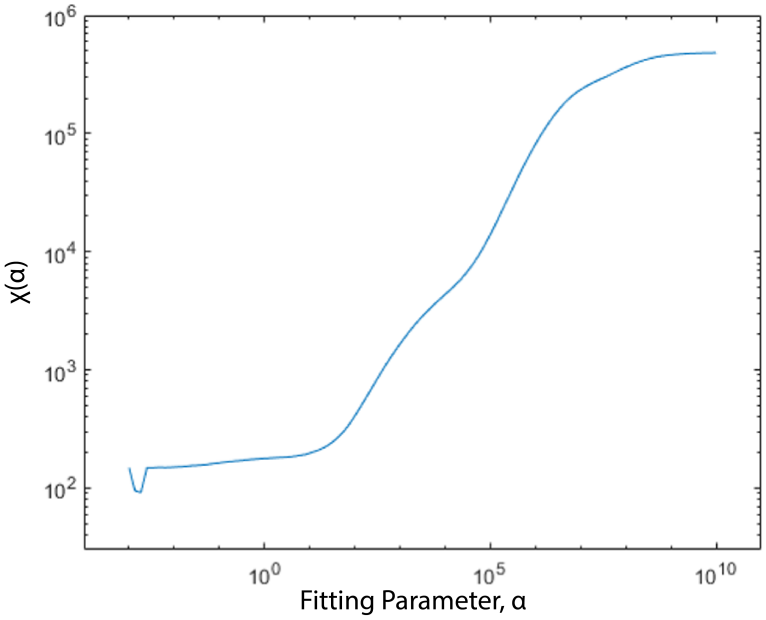


Figure 7.3 **Example S-Curve for α analysis.** Plotting regularization parameter α, which controls smoothness versus the fit error χ reveals optimal choice of α. Choosing α at the heel of the curve (≈ 10) minimizes fit error while ensuring that the resulting LI is not susceptible to noise instability (seen in the dip in baseline at $\alpha \approx 10^{-3}$). The baseline of the S-curve corresponds to a fit error of ≈ 120 a.u., comparable to the noise of the dataset.

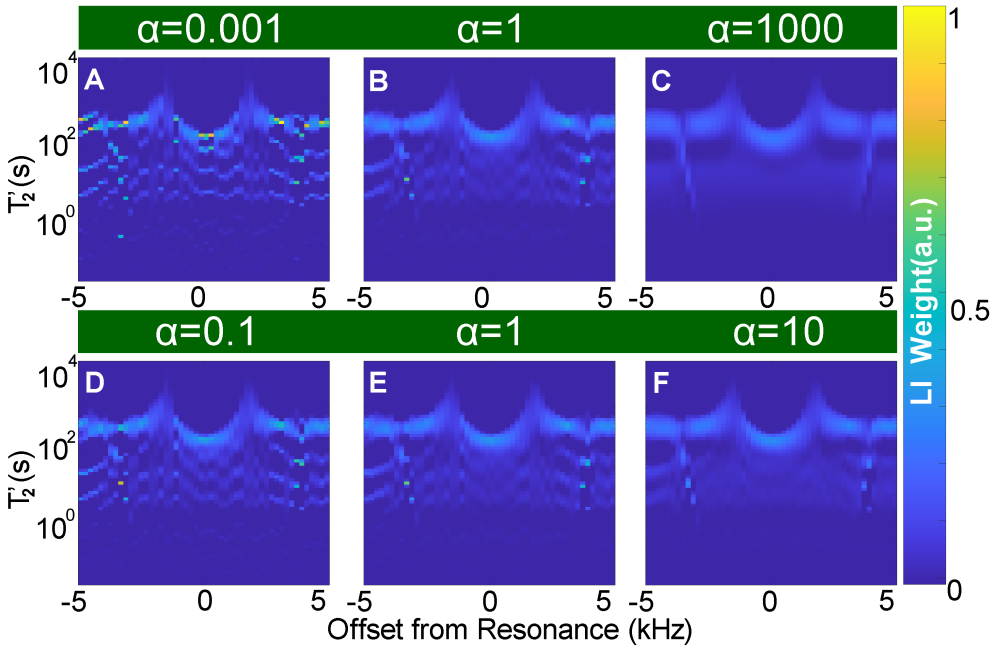


Figure 7.4 **Impact of regularization parameter α on Laplace Inversion.** (A) Small $\alpha = 10^{-3}$ results in high resolution, sharply peaked LI fits but risks potential overfitting, especially at shorter $T_2'^j$ components. (B) Compromise value of $\alpha = 1$ balances resolution and overfitting. (C) Large $\alpha = 1000$ causes LI components to blur, reducing effective resolution. (D)–(F) Varying α over 1-2 orders of magnitude ($\alpha = 0.1$ in D, $\alpha = 1$ in E, $\alpha = 10$ in F) does not significantly change the results of the LI fit, however, varying α over many orders of magnitude (A–C) can have significant changes on the outcome of the LI fit.

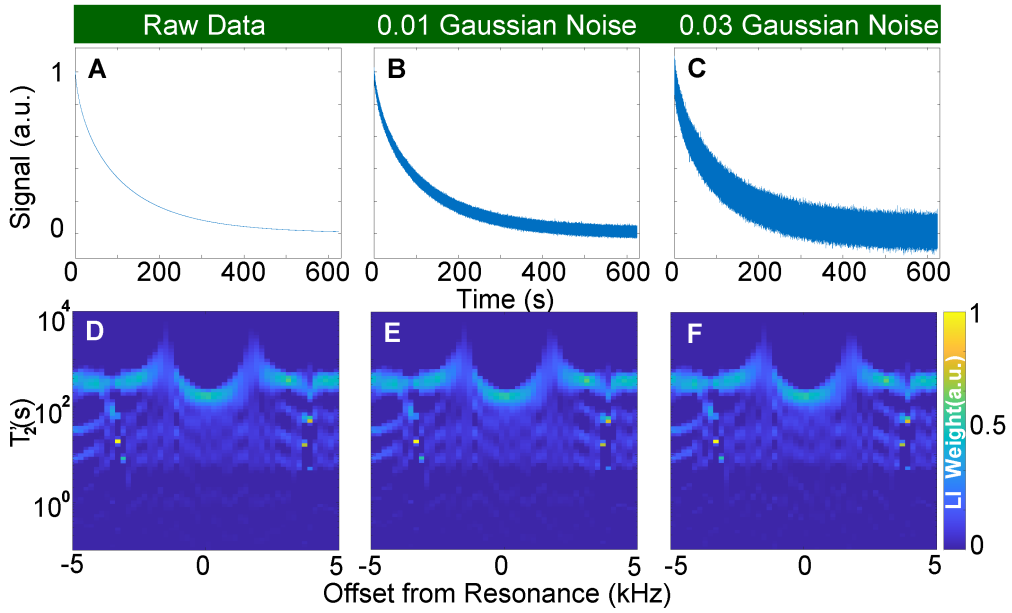


Figure 7.5 **Effect of noise on Laplace Inversion.** (A) On resonance decay curve of S vs t with white Gaussian noise of amplitude 0.01 (B) and 0.03 (C) added to the raw data. Data is taken beyond $t = 600$ s and sampled every $\tau = 43$ μs, yielding > 8 M data points. (D–F) LI maps corresponding to panels (A–C). It can be seen that the LI algorithm is robust even against large amounts of noise added to the raw data as the LI map has almost no change across the three different noise levels.

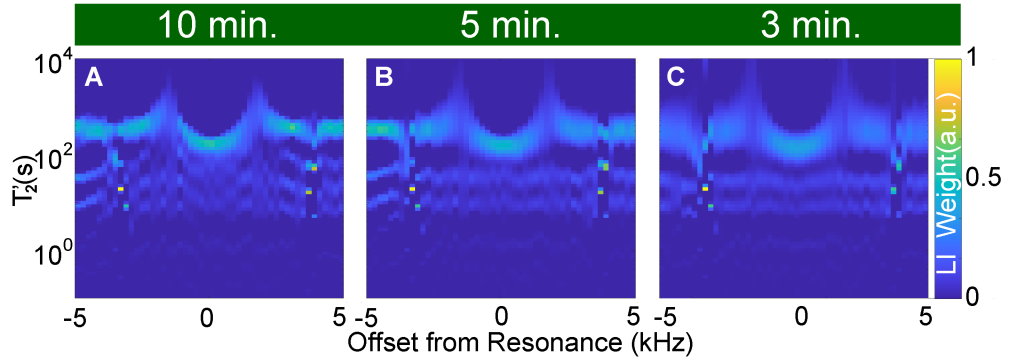


Figure 7.6 **Effect of truncating data on Laplace Inversion maps.** (A) The LI map is shown for data spanning 10 min (the complete dataset collection time). Fitting quality is best for the 10-minute data where the entire decay trace is captured. (B–C) Truncated data (truncated at 5 minutes in (B) and at 3 minutes in (C)) show similar behavior, allowing technically sound conclusions about individual $T_2'^j$ components despite the truncation. However, some broadening is observed in the LI maps, especially at long-time $T_2'^j$ components.

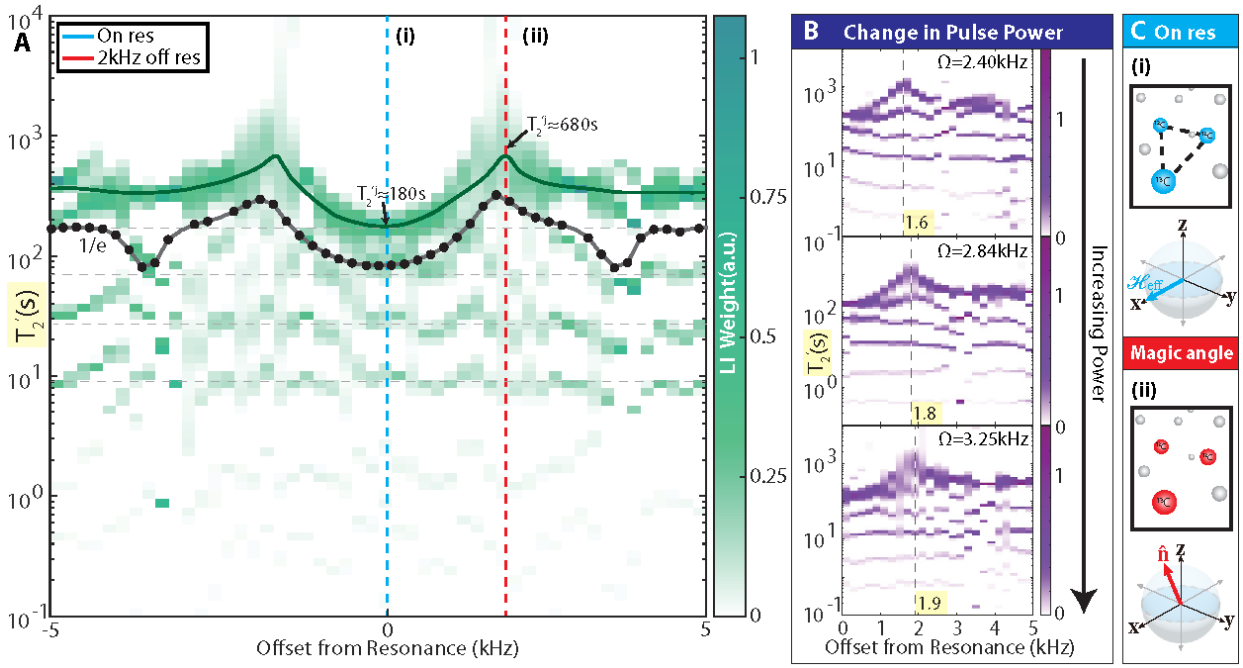


Figure 7.7 T_2' **lifetime extension due to frequency offset..** (A) Laplace Inversion (LI) map constructed from a dataset with 51 values of $\Delta\omega \in [-5, 5]$ kHz. Here t_p=34 μs (nominally $\pi/2$), τ=43 μs, and t_{acq}=4 μs in. Extracted $T_2'^j$ values are plotted on the vertical axis with offset at which dataset was taken plotted on the horizontal axis. The colors represent the strength of constituent LI weights w_j (color bar). Extension of long-time $T_2'^j$ component at $\Delta\omega = \pm$ 2 kHz is evident, yielding two horn-like features with $T_2'^j \approx$680 s. Shorter time components remain consistent across offsets (gray dashed lines). Black points indicate T_2' extracted from a $1/e$ intercept; solid green line is a spline along the longest $T_2'^j$ component. (B) Effect of changing Rabi frequency Ω: LI maps with increasing pulse power and fixed nominal θ=90°. Horns move to larger offset values $\Delta\omega$ (dashed vertical lines and highlighted numbers), consistent with Lee-Goldberg decoupling. (C) Schematic depiction of how on-resonance (i), the ^{13}C nuclei prethermalize to effective Hamiltonian $\mathcal{H}_{\text{eff}}$ aligned with the RF drive along $\hat{\mathbf{x}}$. Dashed lines indicate dipolar couplings. Off-resonance at the LG condition (ii), ^{13}C nuclei prethermalize along magic angle $\hat{n}$ and are self-decoupled to zeroth order.

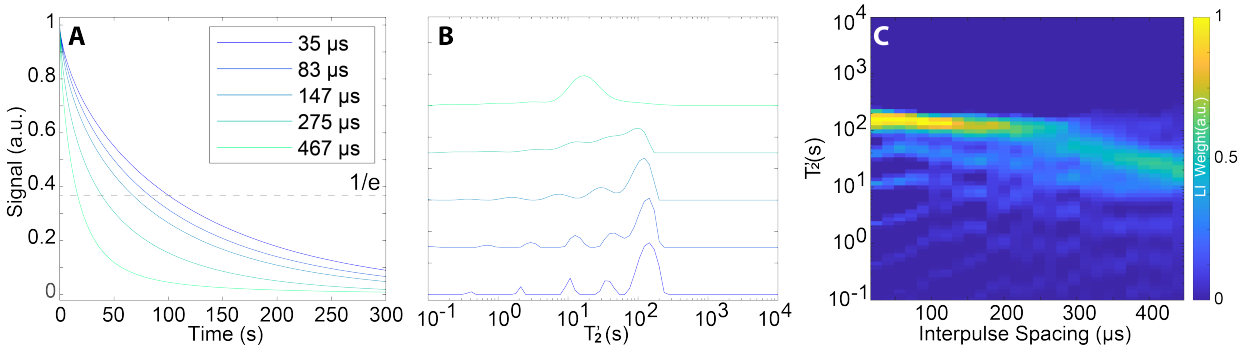


Figure 7.8 **Variation of T_2' as a function of interpulse spacing τ.** (A) On-resonance traces for varying τ (see legend) with a fixed 90-degree pulse. Increasing τ leads to an decrease in T_2' lifetimes. (B) Select 1D LI results for traces in A. The peaks shown here get converted to colors in the color bar in C. (C) LI maps for 28 slices with T_2' values on the vertical axis (logarithmic scale) and interpulse delay τ in μs on the horizontal axis. Shortening of T_2' values at long τ is indicated by the slight negative slope in the traces.

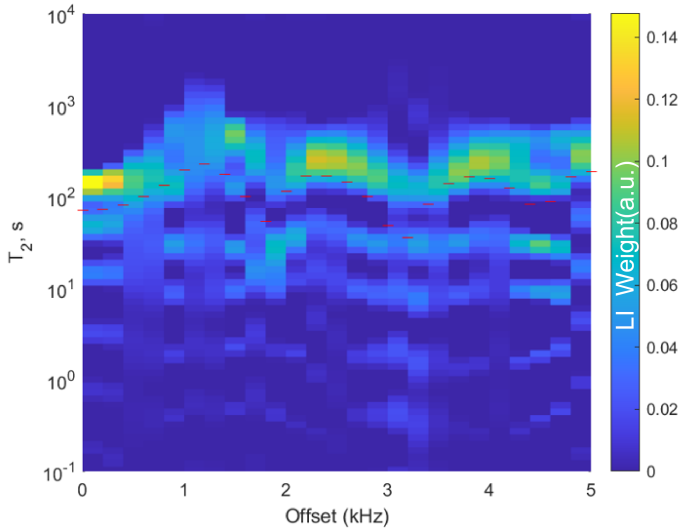


Figure 7.9 **LI as a function of offset for high interpulse spacing.** Laplace Inversion map constructed as a function of offset for pulse sequence with pulse train nominally $\theta = \pi/2$ occurring when $t_p = 33$ μs. Interpulse delay of $\tau = 104$ μs effectively doubles the duty cycle; halving the Rabi frequency of the drive. This results in changes of $\Delta\omega$ to the Lee-Goldburg condition, as well as the $\Delta\omega$ where the decrease in lifetime due to shells formation occurs. Inversion performed with $\alpha = 0.1$, results in narrow, well-defined peaks at short T_2'. Red horizontal bars indicate calculated $1/e$ crossings.

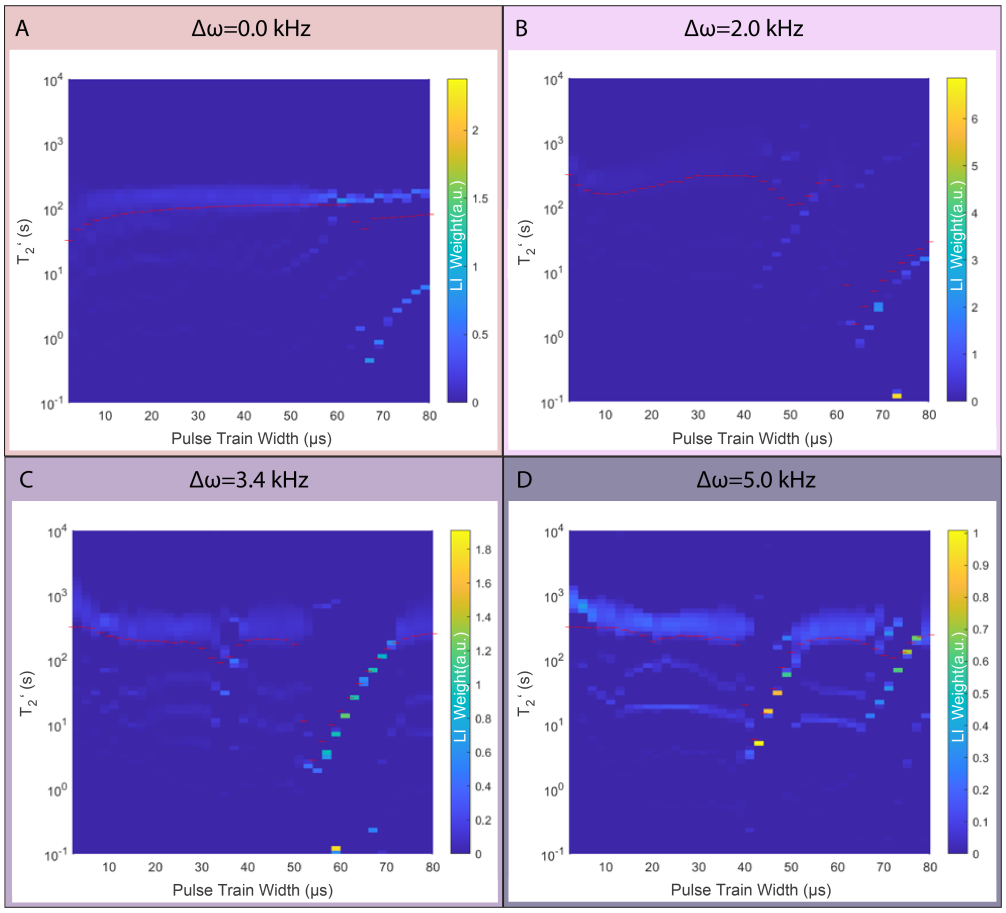


Figure 7.10 **LI maps as a function of pulse train pulse width and transmitter offset.** Laplace Inversion maps constructed as a function of pulse train pulse width t_p, varying from $0 \leq t_p \leq 80$ μs. Red horizontal bars indicate calculated $1/e$ crossings. (A) On resonance, the data is similar to that shown in Chapter 6. Fast decays at short pulse train widths occur due to the extended length of time necessary to complete a full 2π cycle with $t_{cycle} > T_2^*$. When $\theta \approx \pi$ at $t_p \approx 66$ μs, the previously described zero-crossing occurs, causing a dip in $1/e$ time as well as higher weighted short T_2' components. (B) At 2 kHz off resonant, where the LG condition occurs at $t_p \approx 33$ μs, there are three notable features in the data: first, that at short t_p the lifetimes and T_2' become longer; second, that there is a small decrease in lifetime centered around $t_p \approx 50$ μs; and third, that the large decrease in lifetime coupled with the change in LI results indicative of zero-crossing behavior occurs at $t_p \approx 60$ μs. (C) Similar behavior occurs here as in B, with the lifetime extension around short t_p, the decrease in lifetime (here centered around the nominal $\pi/2$ pulse length of $t_p \approx 33$ μs), and the formation of the zero-crossing. (D) Lifetime extension at short t_p is at a maximum, while zero-crossing behavior occurs as early as $t_p \approx 40$ μs. While the small decrease in lifetime (seen in B and C before the zero-crossing is less apparent, there is a decrease in lifetime of similar magnitude occurring after the zero-crossing.

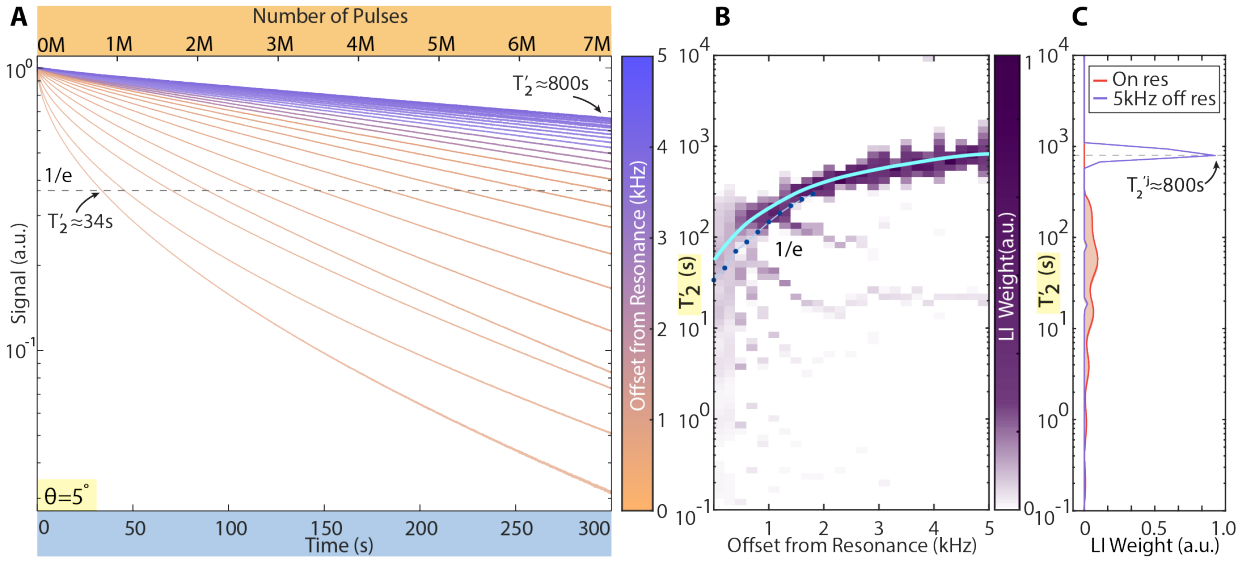


Figure 7.11 **Anomalously long T_2' lifetimes with small-angle pulses.** (A) Normalized decay profiles of S vs t on a semi-log scale for 26 $\Delta\omega$ offset values (see color bar) under a pulsed spinlock of nominal θ=5° pulses. Each trace has >7 M pulses (upper axis). Dashed line shows $1/e$ intercept; we estimate T_2'≈800 s for $\Delta\omega$=5 kHz. (B) Laplace Inversion (LI) map for data in A demonstrates that curves become increasingly mono-exponential with increasing offset. Solid cyan line is a spline fit for the longest $T_2'^j$ component. Black points are corresponding to values extracted from the intercept with $1/e$ line. (C) Representative LI traces for on-resonance (orange shaded) and $\Delta\omega$=5 kHz off-resonance (purple) curves. The latter shows a single T_2' component at ≈800 s, while the former shows a broad distribution of T_2' components.

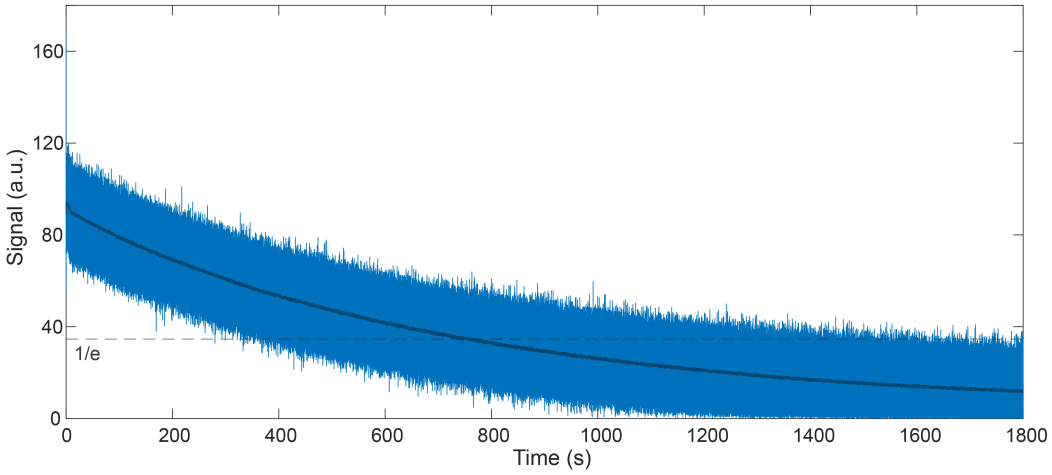


Figure 7.12 **Full decay for longest T_2' spin lifetime.** Unsmoothed decay of S vs t demonstrates typical noise level for experiments where $\Delta\omega = 5$ kHz with $t_p = 2$ μs. $1/e$ based on average of initial 50 data points respresented by dashed grey line. Dark blue line is a result of a 500 point moving average filter, allowing interpretation of $1/e$ crossing at $t \approx 780$ s. Signal is measured until it reaches the noise floor at a total experimental time of 30 min.

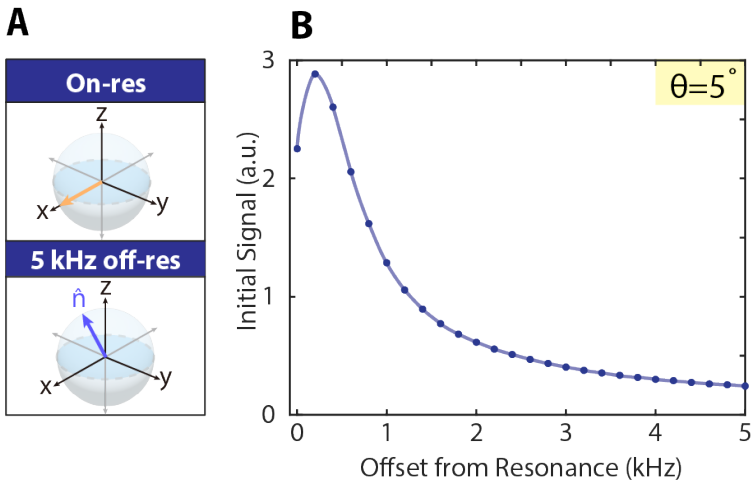


Figure 7.13 **Signal loss due to tilted prethermal axis.** (A) Schematic Bloch sphere description on- and off-resonance at short pulse lengths θ. While the prethermal axis is along the $\hat{\mathbf{x}}$ axis on resonance, off-resonant short-angle pulsing tips the prethermal axis towards $\hat{\mathbf{z}}$. (B) Amplitude change of the initial signal S (integrated over the first second of data) as a function of offset for θ=5°. Solid blue line is a guide to eye. The increase in calculated signal amplitude between $\Delta\omega = 0$ kHz and $\Delta\omega = 0.2$ kHz is due to the integration over the first second of data; the on-resonance signal lifetime is short and thus dies quickly.

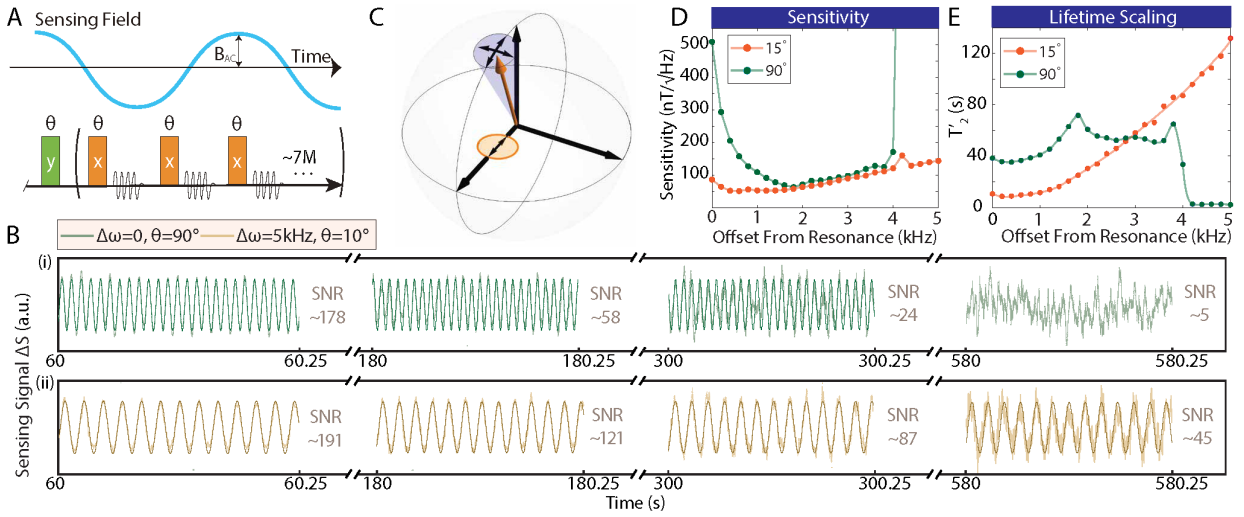


Figure 7.14 **Long-time quantum sensing at room temperature.** (A) Sensing protocol under pulsed spinlocking pulse sequence. Spins are simultaneously exposed to sensing AC field with frequency f_{AC} and amplitude B_{AC}. (B) Comparison of sensing signal ΔS for B_{AC}=82 μT and f_{AC}=50 Hz (i) on-resonance and θ=90° (green), and (ii) $\Delta\omega$=5 kHz off-resonance and nominal θ=10° (yellow). Light line is data, dark line is a sinusoidal fit. Shown are four Δt=100 ms windows centered at t = 60 s, 180 s, 300 s, and 580 s. The SNR in each window is calculated over 1 s which includes the window. Data is smoothed using a moving average filter of 30 points. Off-resonance small-angle sensing signal begins with higher deviations ΔS and persists significantly longer. (C) Schematic Bloch sphere depiction of how the applied AC field results in large deviations ΔS on the $\hat{\mathbf{x}}/\hat{\mathbf{y}}$ plane. (D) Sensitivity of integrated signal as a function of offset $\Delta\omega$ for nominal flip angles θ=15° (orange) and θ=90° (green) for data measured over t=180 s. This sensitivity is calculated from the the absolute value of the Fourier transform at f_{AC}. (E) T_2' lifetime as a function of offset $\Delta\omega$, calculated from $1/e$. Lifetime is significantly extended far off-resonance for θ=15°.

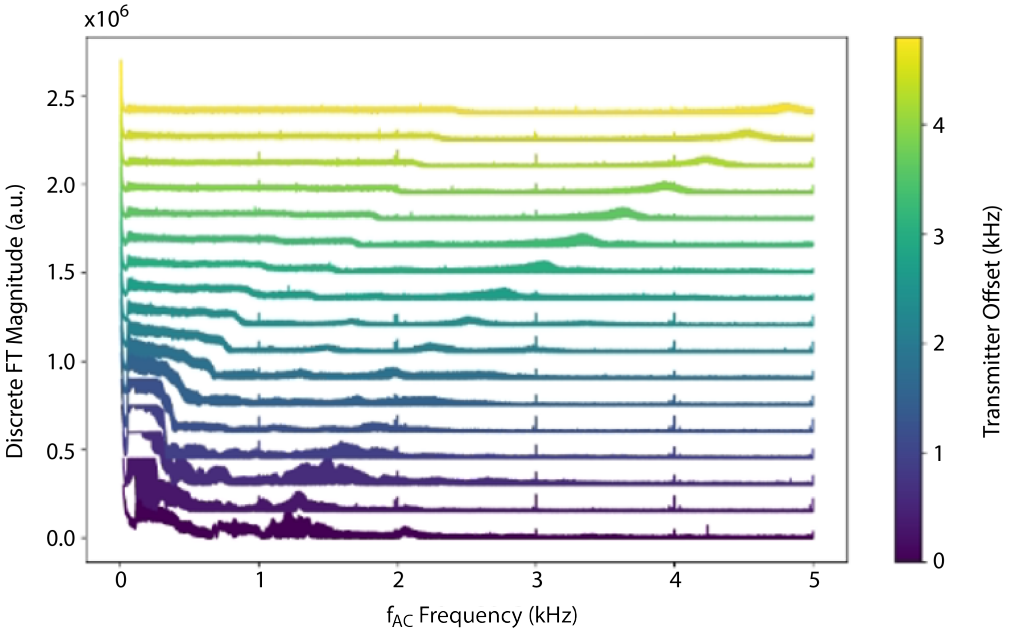


Figure 7.15 **Magnitude of discrete Fourier transform for frequency swept AC field.** Signal decays under which the f_{AC} is swept from 100 Hz to 5 kHz during the experiment. Each dataset is taken at a different offset from $0 \leq \Delta\omega \leq 5$ kHz, under a pulsed spinlock sequence with nominal $\theta = 15°$ pulses. Notably, the small angle pulses result in poor SNR on- and near-resonance, leading to high noise at low f_{AC} frequencies. A peak in the signal demonstrates a rightward shift at higher offset, indicating that the optimal f_{AC} sensing condition changes as a function of transmitter offset. Data collected at room-temperature by L. Moon.

Part V

Conclusion

Chapter 8

Conclusion

Nuclear spins are ubiquitous. As such, they are useful tools to inform on their surroundings, through quantum sensing or other more classical magnetic resonance techniques. However, the usefulness of these approaches can be limited by their finite coherence times. The work presented in this dissertation attempts to address this fundamental limitation by building instrumentation to reach new, promising regimes; change the spin temperature of the nuclear spins and surroundings to extend their lifetimes; and alter the pulse sequence in a way that controllably tunes nuclear spin polarization longevity, both locally through the development of spin polarization shells as well as globally across the ensemble through the addition of a transmitter offset.

Across these approaches, it becomes clear that the challenge of extending nuclear spin lifetimes lies in the understanding of the complex interplay of relaxation effects within the system. Hyperpolarization and local control of spins allow for measurements of selective non-equilibrium spin populations which can demonstrate remarkably long lifetimes (Chapter 7) or unforeseen stability (Chapter 6). Furthermore, considering relaxation as a whole and no longer limiting ourselves to a description along the transverse and longitudinal directions opens the ability to tunably control spin lifetimes. Ultimately, we reveal that the observed transverse lifetime is dependent on the method by which the state is prepared, and that preparation of spins into an engineered state allows spin lifetime extensions to become a controllable parameter.

Bibliography

[1] D. A. Abanin, W. De Roeck, and F. Huveneers. "Exponentially slow heating in periodically driven many-body systems". In: *Physical Review Letters* 115.25 (2015), p. 256803. DOI: 10.1103/PhysRevLett.115.256803.

[2] D. A. Abanin et al. "Colloquium: Many-body localization, thermalization, and entanglement". In: *Reviews of Modern Physics* 91 (2 2019), p. 021001. DOI: 10.1103/RevModPhys.91.021001.

[3] M. Abobeih et al. "Atomic-scale imaging of a 27-nuclear-spin cluster using a quantum sensor". In: *Nature* 576.7787 (2019), pp. 411–415. DOI: 10.1038/s41586-019-1834-7.

[4] A. Abragam and M. Goldman. "Principles of Dynamic Nuclear Polarization". In: *Reports on Progress in Physics* 41.3 (1978), pp. 395–467. DOI: 10.1088/0034-4885/41/3/002.

[5] A. Abragam and W. Proctor. "Experiments on Spin Temperature". In: *Physical Review* 106.1 (1957), pp. 160–161. DOI: 10.1103/PhysRev.106.160.

[6] A. Abragam. "Overhauser Effect in Nonmetals". In: *Physical Review* 98.6 (1955), pp. 1729–1735. DOI: 10.1103/PhysRev.98.1729.

[7] V. M. Acosta et al. "Temperature Dependence of the Nitrogen-Vacancy Magnetic Resonance in Diamond". In: *Physical Review Letters* 104 (7 2010), p. 070801. DOI: 10.1103/PhysRevLett.104.070801.

[8] A. Ajoy et al. "Dynamical decoupling in interacting systems: applications to signal-enhanced hyperpolarized readout". In: *arXiv preprint arXiv:2008.08323* (2020). DOI: 10.48550/arXiv.2008.08323.

[9] A. Ajoy et al. "Hyperpolarized relaxometry based nuclear T 1 noise spectroscopy in diamond". In: *Nature Communications* 10.1 (2019), p. 5160. DOI: 10.1038/s41467-019-13042-3.

[10] A. Ajoy et al. "Enhanced dynamic nuclear polarization via swept microwave frequency combs". In: *Proceedings of the National Academy of Sciences* 115.42 (2018), pp. 10576–10581. DOI: 10.1073/pnas.1807125115.

[11] A. Ajoy et al. "Wide dynamic range magnetic field cycler: Harnessing quantum control at low and high fields". In: *Review of Scientific Instruments* 90.1 (Jan. 2019), p. 013112. DOI: 10.1063/1.5064685.

[12] A. Ajoy et al. "Low-field Microwave-Mediated Optical Hyperpolarization in Optically Pumped Diamond". In: *Journal of Magnetic Resonance* 331 (2021), p. 107021. DOI: 10.1016/j.jmr.2021.107021.

[13] A. Ajoy et al. "Orientation-independent room temperature optical 13C hyperpolarization in powdered diamond". In: *Science Advances* 4.5 (2018), eaar5492. DOI: 10.1126/sciadv.aar5492.

[14] G. A. Álvarez et al. "Local and bulk 13C hyperpolarization in nitrogen-vacancy-centred diamonds at variable fields and orientations". In: *Nature Communications* 6 (2015), p. 8456. DOI: 10.1038/ncomms9456.

[15] A. Anderson and A. Redfield. "Nuclear Spin-Lattice Relaxation in Metals". In: *Physical Review* 116.3 (1959), pp. 583–591. DOI: 10.1103/PhysRev.116.583.

[16] E. R. Andrew, W. S. Hinshaw, and J. P. Jasinski. "An AB_3 High-Resolution NMR Spectrum in the Solid State: ^{31}P in P_4S_3". In: *Chemical Physics Letters* 24.3 (1974), pp. 399–400. DOI: 10.1016/0009-2614(74)85287-5.

[17] J. H. Ardenkjaer-Larsen et al. "Increase in signal-to-noise ratio of > 10,000 times in liquid-state NMR". In: *Proceedings of the National Academy of Sciences* 100.18 (2003), pp. 10158–10163. DOI: 10.1073/pnas.1733835100.

[18] J. H. Ardenkjaer-Larsen. "On the present and future of dissolution-DNP". In: *Journal of Magnetic Resonance* 264 (2016), pp. 3–12. DOI: 10.1016/j.jmr.2016.01.015.

[19] C. Artiaco et al. "Efficient Large-Scale Many-Body Quantum Dynamics via Local-Information Time Evolution". In: *PRX Quantum* 5 (2 2024), p. 020352. DOI: 10.1103/PRXQuantum.5.020352.

[20] N. Aslam et al. "Nanoscale nuclear magnetic resonance with chemical resolution". In: *Science* 357.6346 (2017), pp. 67–71. DOI: 10.1126/science.aam8697.

[21] L. Babich and T. V. Loĭko. "Generalized Paschen's Law for Overvoltage Conditions". In: *IEEE Transactions on Plasma Science* 44.12 (2016), pp. 3243–3248. DOI: 10.1109/TPS.2016.2629022.

[22] S. Bayliss et al. "Optically addressable molecular spins for quantum information processing". In: *Science* 370.6522 (2020), pp. 1309–1312. DOI: 10.1126/science.abb9352.

[23] W. Beatrez et al. "Critical prethermal discrete time crystal created by two-frequency driving". In: *Nature Physics* 19.3 (2023), pp. 407–413. ISSN: 1745-2481. DOI: 10.1038/s41567-022-01891-7.

[24] W. Beatrez et al. "Electron Induced Nanoscale Nuclear Spin Relaxation Probed by Hyperpolarization Injection". In: *Physical Review Letters* 131 (1 July 2023), p. 010802. DOI: 10.1103/PhysRevLett.131.010802.

[25] W. Beatrez et al. "Floquet Prethermalization with Lifetime Exceeding 90 s in a Bulk Hyperpolarized Solid". In: *Physical Review Letters* 127 (17 Oct. 2021), p. 170603. DOI: 10.1103/PhysRevLett.127.170603.

[26] L. R. Becerra et al. "Dynamic nuclear polarization with a cyclotron resonance maser at 5 T". In: *Physical Review Letters* 71.21 (1993), pp. 3561–3564. DOI: 10.1103/PhysRevLett.71.3561.

[27] E. Bendet-Taicher, N. Müller, and A. Jerschow. "Dependence of NMR Noise Line Shapes on Tuning, Matching, and Transmission Line Properties". In: *Concepts in Magnetic Resonance Part B: Magnetic Resonance Engineering* 44B.1 (2014), pp. 1–11. DOI: 10.1002/cmr.b.21253.

[28] A. Bielecki, A. C. Kolbert, and M. H. Levitt. "Frequency-Switched Pulse Sequences: Homonuclear Decoupling and Dilute Spin NMR in Solids". In: *Chemical Physics Letters* 155.4–5 (1989), pp. 341–346. DOI: 10.1016/0009-2614(89)87166-0.

[29] S. Birnkammer, A. Bastianello, and M. Knap. "Prethermalization in one-dimensional quantum many-body systems with confinement". In: *Nature Communications* 13.1 (2022), p. 7663. DOI: 10.1038/s41467-022-35301-6.

[30] F. Bloch. "Nuclear Induction". In: *Physical Review* 70 (1946), pp. 460–474. DOI: 10.1103/PhysRev.70.460.

[31] I. Bloch, J. Dalibard, and W. Zwerger. "Many-body physics with ultracold gases". In: *Reviews of Modern Physics* 80 (3 2008), pp. 885–964. DOI: 10.1103/RevModPhys.80.885.

[32] C. Boehme and D. R. McCamey. "Nuclear-Spin Quantum Memory Poised to Take the Lead". In: *Science* 336.6086 (2012), pp. 1239–1240. ISSN: 1095-9203. DOI: 10.1126/science.1223439.

[33] G. C. Borgia, R. J. Brown, and P. Fantazzini. "Uniform-penalty inversion of multiexponential decay data". In: *Journal of Magnetic Resonance* 132.1 (1998), pp. 65–77. DOI: 10.1006/jmre.1998.1387.

[34] A. Bornet and S. Jannin. "Optimizing dissolution dynamic nuclear polarization". In: *Journal of Magnetic Resonance* 264 (2016), pp. 13–21. DOI: 10.1016/j.jmr.2015.12.007.

[35] S. Braun et al. "Negative absolute temperature for motional degrees of freedom". In: *Science* 339.6115 (2013), pp. 52–55. DOI: 10.1126/science.1227831.

[36] D. Budker and M. Romalis. "Optical magnetometry". In: *Nature Physics* 3.4 (2007), pp. 227–234. DOI: 10.1038/nphys566.

[37] M. Bukov, L. D'Alessio, and A. Polkovnikov. "Universal high-frequency behavior of periodically driven systems: from dynamical stabilization to Floquet engineering". In: *Advances in Physics* 64.2 (2015), pp. 139–226. DOI: 10.1080/00018732.2015.1055918.

[38] M. C. Cambria et al. "Physically Motivated Analytical Expression for the Temperature Dependence of the Zero-Field Splitting of the Nitrogen-Vacancy Center in Diamond". In: *Physical Review B* 108.18 (2023), p. L180102. DOI: 10.1103/PhysRevB.108.L180102.

[39] H. Y. Carr and E. M. Purcell. "Effects of Diffusion on Free Precession in Nuclear Magnetic Resonance Experiments". In: *Physical Review* 94.3 (1954), pp. 630–638. DOI: 10.1103/PhysRev.94.630.

[40] T. R. Carver and C. P. Slichter. "Polarization of nuclear spins in metals". In: *Physical Review* 92.1 (1953), pp. 212–213. DOI: 10.1103/PhysRev.92.212.2.

[41] H. Celik et al. "Stabilization of the inverse Laplace transform of multiexponential decay through introduction of a second dimension". In: *Journal of Magnetic Resonance* 236 (2013), pp. 134–139. DOI: 10.1016/j.jmr.2013.07.008.

[42] C. Charlier et al. "Nanosecond time scale motions in proteins revealed by high-resolution NMR relaxometry". In: *Journal of the American Chemical Society* 135.49 (2013), pp. 18665–18672. DOI: 10.1021/ja409820g.

[43] C.-Y. Chou et al. "A compact high-speed mechanical sample shuttle for field-dependent high-resolution solution NMR". In: *Journal of Magnetic Resonance* 214 (2012), pp. 302–308. DOI: 10.1016/j.jmr.2011.12.001.

[44] C.-Y. Chou et al. "High sensitivity high-resolution full range relaxometry using a fast mechanical sample shuttling device and a cryo-probe". In: *Journal of Biomolecular NMR* 66 (2016), pp. 187–194. DOI: 10.1007/s10858-016-0066-5.

[45] M. S. Conradi and A. P. Zens. "RF shielding and eddy currents in NMR probes". In: *Journal of Magnetic Resonance* 305 (2019), pp. 180–184. DOI: 10.1016/j.jmr.2019.06.011.

[46] S. F. Cousin et al. "High-resolution two-field nuclear magnetic resonance spectroscopy". In: *Physical Chemistry Chemical Physics* 18.48 (2016), pp. 33187–33194. DOI: 10.1039/C6CP05422F.

[47] T. Cvitanić, M. Lukas, and M. S. Grbić. "Two-axis goniometer for single-crystal nuclear magnetic resonance measurements". In: *Review of Scientific Instruments* 90.4 (2019), p. 043903. DOI: 10.1063/1.5075521.

[48] L. D'Alessio et al. "From quantum chaos and eigenstate thermalization to statistical mechanics and thermodynamics". In: *Advances in Physics* 65.3 (2016), pp. 239–362. DOI: 10.1080/00018732.2016.1198134.

[49] N. D'Souza et al. "Cryogenic field-cycling instrument for optical NMR hyperpolarization studies". In: *Journal of Magnetic Resonance* 375 (2025), p. 107874. DOI: 10.1016/j.jmr.2025.107874.

[50] F. De Biasi et al. "Optically enhanced solid-state 1H NMR spectroscopy". In: *Journal of the American Chemical Society* 145.27 (2023), pp. 14874–14883. DOI: 10.1021/jacs.3c03937.

[51] C. L. Degen, F. Reinhard, and P. Cappellaro. "Quantum sensing". In: *Reviews of Modern Physics* 89.3 (2017), p. 035002. DOI: 10.1103/RevModPhys.89.035002.

[52] J. M. Deutsch. "Eigenstate thermalization hypothesis". In: *Reports on Progress in Physics* 81.8 (2018), p. 082001. DOI: 10.1088/1361-6633/aac9f1.

[53] S. Dhomkar et al. "Long-term data storage in diamond". In: *Science Advances* 2 (10 2016), e1600911. DOI: 10.1126/sciadv.1600911.

[54] M. W. Doherty et al. "The Nitrogen-Vacancy Colour Centre in Diamond". In: *Physics Reports* 528.1 (2013), pp. 1–45. DOI: 10.1016/j.physrep.2013.02.001.

[55] M. Doherty et al. "Towards a room-temperature spin quantum bus in diamond via electron photoionization, transport, and capture". In: *Physical Review X* 6.4 (2016), p. 041035. DOI: 10.1103/PhysRevX.6.041035.

[56] Y. Dong et al. "Controlling coherence using the internal structure of hard π pulses". In: *Physical Review Letters* 100.24 (2008), p. 247601. DOI: 10.1103/PhysRevLett.100.247601.

[57] A. Eckardt. "Colloquium: Atomic quantum gases in periodically driven optical lattices". In: *Reviews of Modern Physics* 89 (1 2017), p. 011004. DOI: 10.1103/RevModPhys.89.011004.

[58] T. R. Eichhorn et al. "Hyperpolarized Solution-State NMR Spectroscopy with Optically Polarized Crystals". In: *Journal of the American Chemical Society* 144.6 (2022), pp. 2511–2519. DOI: 10.1021/jacs.1c09119.

[59] T. Eichhorn et al. "High proton spin polarization with DNP using the triplet state of pentacene-d14". In: *Chemical Physics Letters* 555 (2013), pp. 296–299. DOI: 10.1016/j.cplett.2012.11.007.

[60] T. Eichhorn et al. "Proton polarization above 70% by DNP using photo-excited triplet states, a first step towards a broadband neutron spin filter". In: *Nuclear Instruments and Methods in Physics Research Section A: Accelerators, Spectrometers, Detectors and Associated Equipment* 754 (2014), pp. 10–14. DOI: 10.1016/j.nima.2014.03.047.

[61] J. Eills et al. "Spin Hyperpolarization in Modern Magnetic Resonance". In: *Chemical Reviews* 123.4 (2023), pp. 1417–1551. DOI: 10.1021/acs.chemrev.2c00534.

[62] D. V. Else, B. Bauer, and C. Nayak. "Prethermal Phases of Matter Protected by Time-Translation Symmetry". In: *Physical Review X* 7 (1 2017), p. 011026. DOI: 10.1103/PhysRevX.7.011026.

[63] A. English et al. "Quantitative two-dimensional time correlation relaxometry". In: *Magnetic Resonance in Medicine* 22.2 (1991), pp. 425–434. DOI: 10.1002/mrm.1910220250.

[64] A. L. Falk et al. "Optical polarization of nuclear spins in silicon carbide". In: *Physical Review Letters* 114.24 (2015), p. 247603. DOI: 10.1103/PhysRevLett.114.247603.

[65] R. Fischer et al. "Bulk nuclear polarization enhanced at room temperature by optical pumping". In: *Physical Review Letters* 111.5 (2013), p. 057601. DOI: 10.1103/PhysRevLett.111.057601.

[66] R. Fischer et al. "Optical Polarization of Nuclear Ensembles in Diamond". In: *Physical Review B* 87.12 (2013), p. 125207. DOI: 10.1103/PhysRevB.87.125207.

[67] C. Fleckenstein and M. Bukov. "Thermalization and prethermalization in periodically kicked quantum spin chains". In: *Physical Review B* 103 (14 2021), p. 144307. DOI: 10.1103/PhysRevB.103.144307.

[68] R. Freeman. *Spin Choreography: Basic Steps in High Resolution NMR*. Revised. Oxford: Oxford University Press, 1998. ISBN: 9780198504818.

[69] S. Fujiwara et al. "Dynamic Nuclear Polarization of Metal–Organic Frameworks Using Photoexcited Triplet Electrons". In: *Journal of the American Chemical Society* 140.46 (2018), pp. 15606–15610. DOI: 10.1021/jacs.8b10121.

[70] S. Fujiwara et al. "Dynamic Nuclear Polarization of Metal–Organic Frameworks Using Photoexcited Triplet Electrons". In: *Journal of the American Chemical Society* 140.46 (2018), pp. 15606–15610. DOI: 10.1021/jacs.8b10121.

[71] S. Fujiwara et al. "Triplet Dynamic Nuclear Polarization of Guest Molecules through Induced Fit in a Flexible Metal–Organic Framework". In: *Angewandte Chemie International Edition* 61.9 (2022), e202115792. DOI: 10.1002/anie.202115792.

[72] M. Goldman. *Spin Temperature and Nuclear Magnetic Resonance in Solids*. 1st ed. Oxford: Clarendon Press, 1970.

[73] M. L. Goldman et al. "Phonon-induced population dynamics and intersystem crossing in nitrogen-vacancy centers". In: *Physical Review Letters* 114.14 (2015), p. 145502. DOI: 10.1103/PhysRevLett.114.145502.

[74] N. Goldman and J. Dalibard. "Periodically Driven Quantum Systems: Effective Hamiltonians and Engineered Gauge Fields". In: *Physical Review X* 4 (3 2014), p. 031027. DOI: 10.1103/PhysRevX.4.031027.

[75] B. M. Goodson. "Applications of Optical Pumping and Polarization Techniques in NMR I: Optical Nuclear Polarization in Molecular Crystals". In: *Annual Reports on NMR Spectroscopy* 55 (2005), pp. 299–323. DOI: 10.1016/S0066-4103(04)55006-8.

[76] D. Gräsing et al. "Field-cycling NMR with high-resolution detection under magic-angle spinning: determination of field-window for nuclear hyperpolarization in a photosynthetic reaction center". In: *Scientific Reports* 7.1 (Sept. 2017), p. 12111. DOI: 10.1038/s41598-017-10413-y.

[77] S. Grosse et al. "Field cycling by fast NMR probe transfer: Design and application in field-dependent CIDNP experiments". In: *Applied Magnetic Resonance* 17 (1999), pp. 211–225. DOI: 10.1007/BF03162162.

[78] M. Gulka et al. "Room-temperature control and electrical readout of individual nitrogen-vacancy nuclear spins". In: *Nature Communications* 12 (2021), p. 4421. ISSN: 2041-1723. DOI: 10.1038/s41467-021-24494-x.

[79] U. Haeberlen. *High Resolution NMR in Solids: Selective Averaging*. Academic Press Inc., New York, 1976.

[80] U. Haeberlen and J. S. Waugh. "Coherent averaging effects in magnetic resonance". In: *Physical Review* 175.2 (1968), pp. 453–467. DOI: 10.1103/PhysRev.175.453.

[81] A. M. Hall, T. A. Cartlidge, and G. Pileio. "A temperature-controlled sample shuttle for field-cycling NMR". In: *Journal of Magnetic Resonance* 317 (2020), p. 106778. DOI: 10.1016/j.jmr.2020.106778.

[82] T. Hamachi et al. "Porphyrins as versatile, aggregation-tolerant, and biocompatible polarizing agents for triplet dynamic nuclear polarization of biomolecules". In: *The Journal of Physical Chemistry Letters* 12.10 (2021), pp. 2645–2650. DOI: 10.1021/acs.jpclett.1c00294.

[83] R. Hanson et al. "Coherent Dynamics of a Single Spin Interacting with an Adjustable Spin Bath". In: *Science* 320.5874 (2008), pp. 352–355. DOI: 10.1126/science.1155400.

[84] K. Harkins et al. "Nanoscale Engineering and Dynamic Stabilization of Mesoscopic Spin Textures". In: *Science Advances* 11.13 (2025), eadn9021. DOI: 10.1126/sciadv.adn9021.

[85] K. A. Harkins et al. "Anomalously Extended Floquet Prethermal Lifetimes and Applications to Long-Time Quantum Sensing". In: *arXiv preprint arXiv:2410.09028* (2024). DOI: 10.48550/arXiv.2410.09028. arXiv: 2410.09028 [quant-ph].

[86] P. Hautle and W. T. Wenckebach. "Creating high, portable proton polarization with photo-excited triplet DNP". In: *Journal of Magnetic Resonance Open* 20 (2024), p. 100159. DOI: 10.1016/j.jmro.2024.100159.

[87] L. Hebel and C. Slichter. "Nuclear Spin Relaxation in Normal and Superconducting Aluminum". In: *Physical Review* 113.6 (1959), pp. 1504–1519. DOI: 10.1103/PhysRev.113.1504.

[88] J. Hellwagner et al. "Origin of the residual line width under frequency-switched Lee–Goldburg decoupling in MAS solid-state NMR". In: *Magnetic Resonance* 1.1 (2020), pp. 13–25. DOI: 10.5194/mr-1-13-2020.

[89] W. W. Ho et al. "Quantum and classical Floquet prethermalization". In: *Annals of Physics* 454 (2023), p. 169297. DOI: 10.1016/j.aop.2023.169297.

[90] R. IJsselsteijn et al. "A full optically operated magnetometer array: An experimental study". In: *Review of Scientific Instruments* 83.11 (2012), p. 113106. DOI: 10.1063/1.4766961.

[91] V. Ivády et al. "Theoretical model of dynamic spin polarization of nuclei coupled to paramagnetic point defects in diamond and silicon carbide". In: *Physical Review B* 92.11 (2015), p. 115206. DOI: 10.1103/PhysRevB.92.115206.

[92] V. Jacques et al. "Dynamic Polarization of Single Nuclear Spins by Optical Pumping of Nitrogen-Vacancy Color Centers in Diamond at Room Temperature". In: *Physical Review Letters* 102.5 (2009), p. 057403. DOI: 10.1103/PhysRevLett.102.057403.

[93] F. Jähnig, G. Kwiatkowski, and M. Ernst. "Conceptual and instrumental progress in dissolution dynamic nuclear polarization". In: *Journal of Magnetic Resonance* 264 (2016), pp. 22–29. DOI: 10.1016/j.jmr.2015.12.024.

[94] A. Jarmola et al. "Temperature-and magnetic-field-dependent longitudinal spin relaxation in nitrogen-vacancy ensembles in diamond". In: *Physical Review Letters* 108.19 (2012), p. 197601. DOI: 10.1103/PhysRevLett.108.197601.

[95] V. Kalendra et al. "Q-band EPR cryoprobe". In: *Journal of Magnetic Resonance* 356 (2023), p. 107573. DOI: 10.1016/j.jmr.2023.107573.

[96] R. K. Kawakami et al. "Ferromagnetic Imprinting of Nuclear Spins in Semiconductors". In: *Science* 294.5540 (2001), pp. 131–134. ISSN: 00368075, 10959203. DOI: 10.1126/science.1063186.

[97] J. Keeler. *Understanding NMR Spectroscopy*. 2nd ed. John Wiley & Sons, 2010. ISBN: 9780470746097.

[98] R. Kimmich and E. Anoardo. "Field-cycling NMR relaxometry". In: *Progress in Nuclear Magnetic Resonance Spectroscopy* 44.3-4 (2004), pp. 257–320. DOI: 10.1016/j.pnmrs.2004.03.002.

[99] J. P. King, P. J. Coles, and J. A. Reimer. "Optical polarization of C 13 nuclei in diamond through nitrogen vacancy centers". In: *Physical Review B* 81.7 (2010), p. 073201. DOI: 10.1103/PhysRevB.81.073201.

[100] J. P. King et al. "Optically rewritable patterns of nuclear magnetization in gallium arsenide". In: *Nature Communications* 3 (2012), p. 918. DOI: 10.1038/ncomms1918.

[101] A. Kiryutin et al. "Complete magnetic field dependence of SABRE-derived polarization". In: *Magnetic Resonance in Chemistry* 56.7 (2018), pp. 651–662. DOI: 10.1002/mrc.4694.

[102] A. S. Kiryutin et al. "A fast field-cycling device for high-resolution NMR: Design and application to spin relaxation and hyperpolarization experiments". In: *Journal of Magnetic Resonance* 263 (2016), pp. 79–91. DOI: 10.1016/j.jmr.2015.11.017.

[103] T. Klein Kvorning, L. Herviou, and J. H. Bardarson. "Time-evolution of local information: Thermalization dynamics of local observables". In: *SciPost Physics* 13 (2022), p. 080. DOI: 10.21468/SciPostPhys.13.4.080.

[104] K. Kohda, N. Nakamura, and H. Chihara. "Proton Magnetic Relaxation Study of Phase Transition in Crystalline p-Terphenyl". In: *Journal of the Physical Society of Japan* 51.12 (1982), pp. 3936–3941. DOI: 10.1143/JPSJ.51.3936.

[105] K. G. Kurian et al. "Single-beam room-temperature atomic magnetometer with large bandwidth and dynamic range". In: *Physical Review Applied* 19.5 (2023), p. 054040. DOI: 10.1103/PhysRevApplied.19.054040.

[106] A. Kuwahata et al. "Magnetometer with nitrogen-vacancy center in a bulk diamond for detecting magnetic nanoparticles in biomedical applications". In: *Scientific Reports* 10 (2020), p. 2483. DOI: 10.1038/s41598-020-59064-6.

[107] N. D. Lai et al. "Influence of a static magnetic field on the photoluminescence of an ensemble of nitrogen-vacancy color centers in a diamond single-crystal". In: *Applied Physics Letters* 95.13 (2009), p. 133101. DOI: 10.1063/1.3238467.

[108] R. Lamanna. "On the inversion of multicomponent NMR relaxation and diffusion decays in heterogeneous systems". In: *Concepts in Magnetic Resonance Part A: An Educational Journal* 26.2 (2005), pp. 78–90. DOI: 10.1002/cmr.a.20036.

[109] D. W. Laorenza et al. "Tunable Cr4+ molecular color centers". In: *Journal of the American Chemical Society* 143.50 (2021), pp. 21350–21363. DOI: 10.1021/jacs.1c10145.

[110] M. Lee and W. I. Goldburg. "Nuclear-magnetic-resonance line narrowing by a rotating rf field". In: *Physical Review* 140.4A (1965), A1261–A1271. DOI: 10.1103/PhysRev.140.A1261.

[111] M. H. Levitt. *Spin Dynamics: Basics of Nuclear Magnetic Resonance*. 1st ed. Chichester, UK: John Wiley & Sons, 2001. ISBN: 0-471-48921-2.

[112] M. Levitt et al. "High-resolution 1H NMR in solids with frequency-switched multiple-pulse sequences". In: *Solid State Nuclear Magnetic Resonance* 2.4 (1993), pp. 151–163. DOI: 10.1016/0926-2040(93)90021-E.

[113] M. Ljubotina, M. Žnidarič, and T. Prosen. "Spin diffusion from an inhomogeneous quench in an integrable system". In: *Nature Communications* 8 (2017), p. 16117. DOI: 10.1038/ncomms16117.

[114] A. Lozovoi et al. "Detection and Modeling of Hole Capture by Single Point Defects under Variable Electric Fields". In: *Nano Letters* 23.10 (2023), pp. 4495–4501. ISSN: 1530-6992. DOI: 10.1021/acs.nanolett.3c00860.

[115] A. Lozovoi et al. "Imaging dark charge emitters in diamond via carrier-to-photon conversion". In: *Science Advances* 8.1 (2022), eabl9402. ISSN: 2375-2548. DOI: 10.1126/sciadv.abl9402.

[116] X. Lv et al. "Background-free dual-mode optical and 13C magnetic resonance imaging in diamond particles". In: *Proceedings of the National Academy of Sciences* 118.21 (2021), e2023579118. DOI: 10.1073/pnas.2023579118.

[117] F. Machado et al. "Long-Range Prethermal Phases of Nonequilibrium Matter". In: *Physical Review X* 10 (1 2020), p. 011043. DOI: 10.1103/PhysRevX.10.011043.

[118] M. T. Madzik et al. "Controllable freezing of the nuclear spin bath in a single-atom spin qubit". In: *Science Advances* 6.27 (2020), eaba3442. ISSN: 2375-2548. DOI: 10.1126/sciadv.aba3442.

[119] K. Mallayya, M. Rigol, and W. De Roeck. "Prethermalization and thermalization in isolated quantum systems". In: *Physical Review X* 9.2 (2019), p. 021027. DOI: 10.1103/PhysRevX.9.021027.

[120] T. Maly et al. "Dynamic nuclear polarization at high magnetic fields". In: *The Journal of Chemical Physics* 128.5 (2008), p. 052211. DOI: 10.1063/1.2833582.

[121] N. B. Manson, J. P. Harrison, and M. J. Sellars. "Nitrogen-vacancy center in diamond: Model of the electronic structure and associated dynamics". In: *Physical Review B* 74.10 (2006), p. 104303. DOI: 10.1103/PhysRevB.74.104303.

[122] J. R. Maze et al. "Nanoscale magnetic sensing with an individual electronic spin in diamond". In: *Nature* 455.7213 (2008), pp. 644–647. DOI: 10.1038/nature07279.

[123] M. Mehring and J. Waugh. "Magic-angle NMR experiments in solids". In: *Physical Review B* 5.9 (1972), pp. 3459–3471. DOI: 10.1103/PhysRevB.5.3459.

[124] M. Mehring. *Principles of High Resolution NMR in Solids*. 2nd ed. Springer-Verlag, 1983.

[125] S. Meiboom and D. Gill. "Modified Spin-Echo Method for Measuring Nuclear Relaxation Times". In: *Review of Scientific Instruments* 29.8 (1958), pp. 688–691. DOI: 10.1063/1.1716296.

[126] A. Mena et al. "Room-temperature optically detected coherent control of molecular spins". In: *Physical Review Letters* 133.12 (2024), p. 120801. DOI: 10.1103/PhysRevLett.133.120801.

[127] P. Millington-Hotze et al. "Nuclear spin diffusion in the central spin system of a GaAs/AlGaAs quantum dot". In: *Nature Communications* 14.1 (2023), p. 2677. DOI: 10.1038/s41467-023-38349-0.

[128] N. Mizuochi et al. "Coherence of single spins coupled to a nuclear spin bath of varying density". In: *Physical Review B* 80.4 (2009), p. 041201. DOI: 10.1103/PhysRevB.80.041201.

[129] L. J. I. Moon et al. "High-Speed, High-Memory NMR Spectrometer and Hyperpolarizer". In: *Journal of Magnetic Resonance* 380 (2025), p. 107952. DOI: 10.1016/j.jmr.2025.107952.

[130] L. J. I. Moon et al. "Sensing with discrete time crystals". In: *Nature Physics* 22.3 (2026), pp. 367–373. DOI: 10.1038/s41567-025-03163-6.

[131] A. Morello et al. "Donor Spins in Silicon for Quantum Technologies". In: *Advanced Quantum Technologies* 3.11 (2020), p. 2000005. ISSN: 2511-9044. DOI: 10.1002/qute.202000005.

[132] K. R. Mote, V. Agarwal, and P. Madhu. "Five decades of homonuclear dipolar decoupling in solid-state NMR: Status and outlook". In: *Progress in Nuclear Magnetic Resonance Spectroscopy* 97 (2016), pp. 1–39. DOI: 10.1016/j.pnmrs.2016.08.001.

[133] J. T. Muhonen et al. "Storing quantum information for 30 seconds in a nanoelectronic device". In: *Nature Nanotechnology* 9.12 (2014), pp. 986–991. ISSN: 1748-3395. DOI: 10.1038/nnano.2014.211.

[134] Q. Z. Ni et al. "High-frequency dynamic nuclear polarization". In: *Accounts of Chemical Research* 46.9 (2013), pp. 1933–1941. DOI: 10.1021/ar300348n.

[135] L. Nie et al. "Quantum monitoring of cellular metabolic activities in single mitochondria". In: *Science Advances* 7.21 (2021), eabf0573. DOI: 10.1126/sciadv.abf0573.

[136] K. Nishimura et al. "Materials chemistry of triplet dynamic nuclear polarization". In: *Chemical Communications* 56.53 (2020), pp. 7217–7232. DOI: 10.1039/d0cc02258f.

[137] Y. Nishiyama et al. "Ultrafast magic angle spinning solid-state NMR spectroscopy: advances in methodology and applications". In: *Chemical Reviews* 123.3 (2023), pp. 918–988. DOI: 10.1021/acs.chemrev.2c00197.

[138] J. O'Sullivan et al. "Random-Access Quantum Memory Using Chirped Pulse Phase Encoding". In: *Physical Review X* 12 (4 2022), p. 041014. DOI: 10.1103/PhysRevX.12.041014.

[139] E. Ostroff and J. Waugh. "Multiple spin echoes and spin locking in solids". In: *Physical Review Letters* 16.24 (1966), pp. 1097–1098. DOI: 10.1103/PhysRevLett.16.1097.

[140] A. Overhauser. "Polarization of Nuclei in Metals". In: *Physical Review* 92.2 (1953), pp. 411–415. DOI: 10.1103/PhysRev.92.411.

[141] B. R. Page et al. "Compact quantum magnetometer system on an agile underwater glider". In: *Sensors* 21.4 (2021), p. 1092. DOI: 10.3390/s21041092.

[142] S. Pal et al. "Temporal order in periodically driven spins in star-shaped clusters". In: *Physical Review Letters* 120.18 (2018), p. 180602. DOI: 10.1103/PhysRevLett.120.180602.

[143] A. J. Parker et al. "Optically pumped dynamic nuclear hyperpolarization in C 13-enriched diamond". In: *Physical Review B* 100 (4 2019), p. 041203. DOI: 10.1103/PhysRevB.100.041203.

[144] P. Peng et al. "Floquet prethermalization in dipolar spin chains". In: *Nature Physics* 17.4 (2021), pp. 444–447. DOI: 10.1038/s41567-020-01120-z.

[145] A. Pillai et al. "Electron-to-nuclear spectral mapping via dynamic nuclear polarization". In: *The Journal of Chemical Physics* 159.15 (2023), p. 154201. DOI: 10.1063/5.0157954.

[146] A. Pines, M. G. Gibby, and J. S. Waugh. "Proton-enhanced NMR of dilute spins in solids". In: *The Journal of Chemical Physics* 59.2 (1973), pp. 569–590. DOI: 10.1063/1.1680061.

[147] R. Pound. "Nuclear Spin Relaxation Times in Single Crystals of LiF". In: *Physical Review* 81.1 (1951), p. 156. DOI: 10.1103/PhysRev.81.156.

[148] S. W. Provencher. "A constrained regularization method for inverting data represented by linear algebraic or integral equations". In: *Computer Physics Communications* 27.3 (1982), pp. 213–227. DOI: 10.1016/0010-4655(82)90173-4.

[149] E. Purcell and R. Pound. "A Nuclear Spin System at Negative Temperature". In: *Physical Review* 81.2 (1951), pp. 279–280. DOI: 10.1103/PhysRev.81.279.

[150] N. Ramsey and R. Pound. "Nuclear Audiofrequency Spectroscopy by Resonant Heating of the Nuclear Spin System". In: *Physical Review* 81.2 (1951). DOI: 10.1103/PhysRev.81.278.

[151] E. Ravera, C. Luchinat, and G. Parigi. "Basic facts and perspectives of Overhauser DNP NMR". In: *Journal of Magnetic Resonance* 264 (2016), pp. 78–87. DOI: 10.1016/j.jmr.2015.12.013.

[152] A. Redfield. "Nuclear Spin Relaxation Time in Superconducting Aluminum". In: *Physical Review Letters* 3.2 (1959), pp. 85–86. DOI: 10.1103/PhysRevLett.3.85.

[153] A. G. Redfield. "Shuttling device for high-resolution measurements of relaxation and related phenomena in solution at low field, using a shared commercial 500 MHz NMR instrument". In: *Magnetic Resonance in Chemistry* 41.10 (2003), pp. 753–768. DOI: 10.1002/mrc.1264.

[154] J. A. Reimer. "Nuclear hyperpolarization in solids and the prospects for nuclear spintronics". In: *Solid State Nuclear Magnetic Resonance* 37.1-2 (2010), pp. 3–12. DOI: 10.1016/j.ssnmr.2010.04.001.

[155] E. C. Reynhardt and G. L. High. "Nuclear magnetic resonance studies of diamond". In: *Progress in Nuclear Magnetic Resonance Spectroscopy* 38.1 (2001), pp. 37–81. DOI: 10.1016/S0079-6565(00)00025-X.

[156] E. Reynhardt and C. Terblanche. "13C relaxation in natural diamond". In: *Chemical Physics Letters* 269.5-6 (1997), pp. 464–468. DOI: 10.1016/S0009-2614(97)00309-6.

[157] E. C. Reynhardt and G. L. High. "Dynamic nuclear polarization of diamond. I. Solid state and thermal mixing effects". In: *The Journal of Chemical Physics* 109.10 (1998), pp. 4090–4099. DOI: 10.1063/1.477009.

[158] W.-K. Rhim, D. Burum, and D. Elleman. "Calculation of spin–lattice relaxation during pulsed spin locking in solids". In: *The Journal of Chemical Physics* 68.2 (1978), pp. 692–695. DOI: 10.1063/1.435742.

[159] W.-K. Rhim, D. Burum, and D. Elleman. "Multiple-pulse spin locking in dipolar solids". In: *Physical Review Letters* 37.26 (1976), pp. 1764–1766. DOI: 10.1103/PhysRevLett.37.1764.

[160] M. Rigol, V. Dunjko, and M. Olshanii. "Thermalization and its mechanism for generic isolated quantum systems". In: *Nature* 452.7189 (2008), pp. 854–858. DOI: 10.1038/nature06838.

[161] M. Rosay et al. "Solid-state dynamic nuclear polarization at 263 GHz: spectrometer design and experimental results". In: *Physical Chemistry Chemical Physics* 12.22 (2010), pp. 5850–5860. DOI: 10.1039/C003685B.

[162] E. Rosenberg et al. "Dynamics of magnetization at infinite temperature in a Heisenberg spin chain". In: *Science* 384.6691 (2024), pp. 48–53. DOI: 10.1126/science.adi7877.

[163] A. Rotem et al. "Limits on spectral resolution measurements by quantum probes". In: *Physical Review Letters* 122.6 (2019), p. 060503. DOI: 10.1103/PhysRevLett.122.060503.

[164] A. Rubio-Abadal et al. "Floquet Prethermalization in a Bose-Hubbard System". In: *Physical Review X* 10 (2 May 2020), p. 021044. DOI: 10.1103/PhysRevX.10.021044.

[165] O. Sahin et al. "High field magnetometry with hyperpolarized nuclear spins". In: *Nature Communications* 13.1 (2022), p. 5486. DOI: 10.1038/s41467-022-32907-8.

[166] O. Sahin et al. "Micromotion-based DC sensing using continuously tracked trajectories of dipolar coupled nuclear spins". In: *Physical Review Research* 7.4 (2025), p. 043272. DOI: 10.1103/bgdc-rgkd.

[167] K. Sakamoto et al. "Polarizing agents beyond pentacene for efficient triplet dynamic nuclear polarization in glass matrices". In: *Proceedings of the National Academy of Sciences* 120.44 (2023), e2307926120. DOI: 10.1073/pnas.2307926120.

[168] A. Sarkar et al. "Rapidly Enhanced Spin-Polarization Injection in an Optically Pumped Spin Ratchet". In: *Physical Review Applied* 18.3 (2022), p. 034079. DOI: 10.1103/PhysRevApplied.18.034079.

[169] K. Schaumburg, E. S. Shabanova, and J. P. F. Sellschop. "NMR Studies of Orientation-Dependent Nuclear Spin-Spin Relaxation and Line Shapes in ^{13}C-Enriched Diamonds". In: *Journal of Magnetic Resonance, Series A* 112 (1995), pp. 176–181. DOI: 10.1006/jmra.1995.1029.

[170] S. Schmitt et al. "Optimal frequency measurements with quantum probes". In: *npj Quantum Information* 7 (2021), p. 55. DOI: 10.1038/s41534-021-00391-5.

[171] E. Scott, M. Drake, and J. A. Reimer. "The phenomenology of optically pumped 13 C NMR in diamond at 7.05 T: Room temperature polarization, orientation dependence, and the effect of defect concentration on polarization dynamics". In: *Journal of Magnetic Resonance* 264 (2016), pp. 154–162. DOI: 10.1016/j.jmr.2016.01.001.

[172] C. M. Selco et al. "Breakdown of Disorder-Suppressed Floquet Heating under Two-Frequency Driving". In: *Physical Review Letters* 136.22 (2026), p. 220801. DOI: 10.1103/t953-lhht.

[173] C. M. Selco et al. "Emergent Decoherence Dynamics in Doubly Disordered Spin Networks". In: *arXiv preprint arXiv:2511.07785* (2025). DOI: 10.48550/arXiv.2511.07785. arXiv: 2511.07785 [quant-ph].

[174] L. Shao et al. "Diamond radio receiver: nitrogen-vacancy centers as fluorescent transducers of microwave signals". In: *Physical Review Applied* 6.6 (2016), p. 064008. DOI: 10.1103/PhysRevApplied.6.064008.

[175] H. Singh et al. "Room-temperature quantum sensing with photoexcited triplet electrons in organic crystals". In: *Physical Review Research* 7.1 (2025), p. 013192. DOI: 10.1103/PhysRevResearch.7.013192.

[176] K. Singh et al. "Quantifying and Controlling Prethermal Nonergodicity in Interacting Floquet Matter". In: *Physical Review X* 9 (4 2019), p. 041021. DOI: 10.1103/PhysRevX.9.041021.

[177] C. Slichter and W. C. Holton. "Adiabatic demagnetization in a rotating reference system". In: *Physical Review* 122.6 (1961), pp. 1701–1708. DOI: 10.1103/PhysRev.122.1701.

[178] Y.-Q. Song, L. Venkataramanan, and L. Burcaw. "Determining the resolution of Laplace inversion spectrum". In: *The Journal of Chemical Physics* 122.10 (2005), p. 104104. DOI: 10.1063/1.1858436.

[179] Y.-Q. Song et al. "T1–T2 correlation spectra obtained using a fast two-dimensional Laplace inversion". In: *Journal of Magnetic Resonance* 154.2 (2002), pp. 261–268. DOI: 10.1006/jmre.2001.2474.

[180] M. Srednicki. "Chaos and quantum thermalization". In: *Phys. Rev. E* 50 (2 1994), pp. 888–901. DOI: 10.1103/PhysRevE.50.888.

[181] R. M. Steele et al. "New applications and perspectives of fast field cycling NMR relaxometry". In: *Magnetic Resonance in Chemistry* 54.6 (2016), pp. 502–509. DOI: 10.1002/mrc.4220.

[182] J. Stephens et al. "Optically patterned nuclear doughnuts in GaAs/MnAs heterostructures". In: *Applied Physics Letters* 85 (7 2004), pp. 1184–1186. DOI: 10.1063/1.1781743.

[183] Q. Stern et al. "Direct observation of hyperpolarization breaking through the spin diffusion barrier". In: *Science Advances* 7.18 (2021), eabf5735. DOI: 10.1126/sciadv.abf5735.

[184] H.-J. Stöckmann and P. Heitjans. "Low-Temperature Nuclear Spin-Lattice Relaxation in Glasses – Homogeneous and Inhomogeneous Averaging". In: *Journal of Non-Crystalline Solids* 66.3 (1984), pp. 501–509. DOI: 10.1016/0022-3093(84)90373-9.

[185] K. Tagami et al. "Design of a cryogen-free high field dual EPR and DNP probe". In: *Journal of Magnetic Resonance* 347 (2023), p. 107351. ISSN: 1090-7807. DOI: 10.1016/j.jmr.2022.107351.

[186] S. Takahashi et al. "Quenching Spin Decoherence in Diamond through Spin Bath Polarization". In: *Physical Review Letters* 101.4 (2008), p. 047601. DOI: 10.1103/PhysRevLett.101.047601.

[187] K. Tateishi et al. "Room temperature hyperpolarization of nuclear spins in bulk". In: *Proceedings of the National Academy of Sciences* 111.21 (2014), pp. 7527–7530. DOI: 10.1073/pnas.1315778111.

[188] D. Tse and S. Hartmann. "Nuclear spin-lattice relaxation via paramagnetic centers without spin diffusion". In: *Physical Review Letters* 21.8 (1968), pp. 511–514. DOI: 10.1103/PhysRevLett.21.511.

[189] R. Tycko. "NMR at Low and Ultralow Temperatures". In: *Accounts of Chemical Research* 46.9 (2013), pp. 1923–1932. DOI: 10.1021/ar300358z.

[190] L. Venkataramanan, Y.-Q. Song, and M. D. Hürlimann. "Solving Fredholm integrals of the first kind with tensor product structure in 2 and 2.5 dimensions". In: *IEEE Transactions on Signal Processing* 50.5 (2002), pp. 1017–1026. DOI: 10.1109/78.995059.

[191] E. Vinogradov, P. K. Madhu, and S. Vega. "High-resolution proton solid-state NMR spectroscopy by phase-modulated Lee–Goldburg experiment". In: *Chemical Physics Letters* 314.5-6 (1999), pp. 443–450. DOI: 10.1016/S0009-2614(99)01174-4.

[192] E. Vinogradov, P. K. Madhu, and S. Vega. "Proton spectroscopy in solid state nuclear magnetic resonance with windowed phase modulated Lee–Goldburg decoupling sequences". In: *Chemical Physics Letters* 354.3-4 (2002), pp. 193–202. DOI: 10.1016/S0009-2614(02)00060-X.

[193] L. Viola, E. Knill, and S. Lloyd. "Dynamical Generation of Noiseless Quantum Subsystems". In: *Physical Review Letters* 85.16 (2000), pp. 3520–3523. DOI: 10.1103/PhysRevLett.85.3520.

[194] D. Wei et al. "Quantum gas microscopy of Kardar-Parisi-Zhang superdiffusion". In: *Science* 376.6594 (2022), pp. 716–720. DOI: 10.1126/science.abk2397.

[195] S. A. Weidinger and M. Knap. "Floquet prethermalization and regimes of heating in a periodically driven, interacting quantum system". In: *Scientific Reports* 7 (2017), p. 45382. DOI: 10.1038/srep45382.

[196] J. F. Wienand et al. "Emergence of Fluctuating Hydrodynamics in Chaotic Quantum Systems". In: *Nature Physics* 20.11 (2024), pp. 1732–1737. DOI: 10.1038/s41567-024-02611-z.

[197] G. von Witte et al. "Temperature-Dependent Dynamic Nuclear Polarization of Diamond". In: *The Journal of Physical Chemistry C* 129.27 (2025), pp. 12577–12584. DOI: 10.1021/acs.jpcc.5c02747.

[198] A. Yurkovskaya et al. "The influence of scavenging on CIDNP field dependences in biradicals during the photolysis of large-ring cycloalkanones". In: *Chemical Physics* 197.2 (1995), pp. 157–166. DOI: 10.1016/0301-0104(95)00125-8.

[199] J. M. Zadrozny et al. "A porous array of clock qubits". In: *Journal of the American Chemical Society* 139.20 (2017), pp. 7089–7094. DOI: 10.1021/jacs.7b03123.

[200] H. Zhao et al. "Suppression of interband heating for random driving". In: *Physical Review Letters* 129.12 (2022), p. 120605. DOI: 10.1103/PhysRevLett.129.120605.

[201] I. V. Zhukov et al. "Field-cycling NMR experiments in an ultra-wide magnetic field range: relaxation and coherent polarization transfer". In: *Physical Chemistry Chemical Physics* 20.18 (2018), pp. 12396–12405. DOI: 10.1039/C7CP08529J.

[202] C. Zu et al. "Emergent hydrodynamics in a strongly interacting dipolar spin ensemble". In: *Nature* 597.7874 (2021), pp. 45–50. DOI: 10.1038/s41586-021-03763-1.